



AN IMPROVED VARIATIONAL MODEL FOR SPECKLE NOISE REDUCTION IN REAL  
ULTRASOUND IMAGES



A Thesis Submitted in Partial Fulfillment of the Requirements  
for Doctor of Philosophy MATHEMATICS

Department of MATHEMATICS

Silpakorn University

Academic Year 2022

Copyright of Silpakorn University

ตัวแบบเชิงแปรผันที่ปรับปรุงสำหรับการลดสัญญาณรบกวนแบบสเปกเกิดจากภาพถ่าย  
คลื่นเสียงความถี่สูง



วิทยานิพนธ์นี้เป็นส่วนหนึ่งของการศึกษาตามหลักสูตรปรัชญาดุษฎีบัณฑิต  
สาขาวิชาคณิตศาสตร์ แบบ 2.1 ปรัชญาดุษฎีบัณฑิต นานาชาติ  
ภาควิชาคณิตศาสตร์  
มหาวิทยาลัยศิลปากร  
ปีการศึกษา 2565  
ลิขสิทธิ์ของมหาวิทยาลัยศิลปากร

AN IMPROVED VARIATIONAL MODEL FOR SPECKLE NOISE REDUCTION  
IN REAL ULTRASOUND IMAGES



A Thesis Submitted in Partial Fulfillment of the Requirements

for Doctor of Philosophy MATHEMATICS

Department of MATHEMATICS

Silpakorn University

Academic Year 2022

Copyright of Silpakorn University

Title                    An improved variational model for speckle noise reduction in real ultrasound  
                                 images

By                        MISS Siriwan CHANKAN

Field of Study        MATHEMATICS

Advisor                Assistant Professor Noppadol Chumchob, Ph.D.

---

Faculty of Science, Silpakorn University in Partial Fulfillment of the Requirements for the  
Doctor of Philosophy

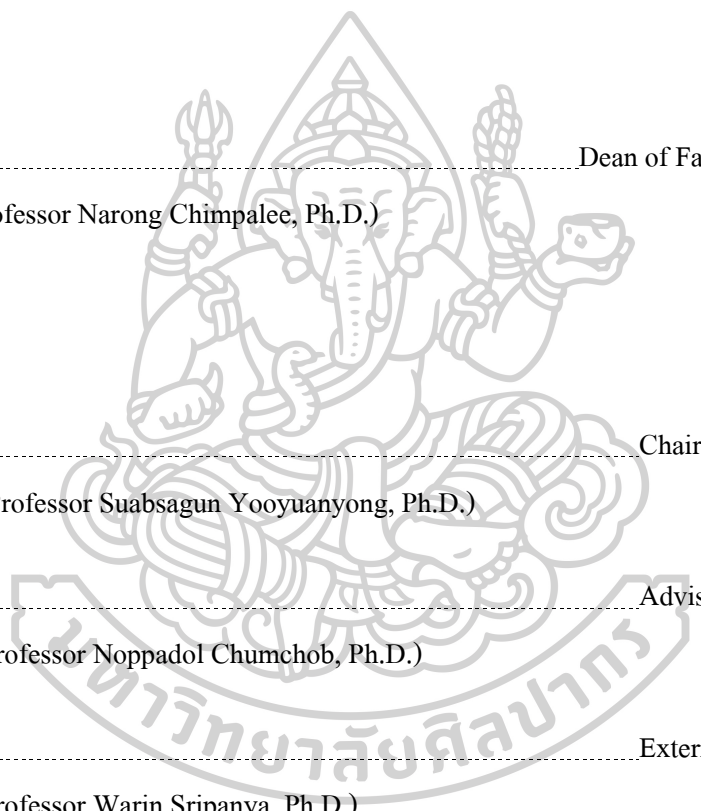
..... Dean of Faculty of Science  
(Assistant Professor Narong Chimpalee, Ph.D.)

Approved by

..... Chair person  
(Associate Professor Suabsagun Yooyuanyong, Ph.D.)

..... Advisor  
(Assistant Professor Noppadol Chumchob, Ph.D.)

..... External Examiner  
(Assistant Professor Warin Sripanya, Ph.D.)



61305802 : MAJOR: MATHEMATICS

KEY WORDS : HIGHER-ORDER VARIATIONAL MODEL, SPLIT BREGMAN METHOD, IMAGE RESTORATION

SIRIWAN CHANKAN : AN IMPROVED VARIATIONAL MODEL FOR SPECKLE NOISE REDUCTION IN REAL ULTRASOUND IMAGES. THESIS ADVISOR : ASSISTANT PROFESSOR NOPPADOL CHUMCHOB, Ph.D.

Noise reduction of ultrasound (US) images corrupted by the mixture of additive and multiplicative speckle noise is an important task in various medical applications. In this research, we first propose a first-order variational model consisting of the total variation (TV) regularization and the new non-quadratic data fidelity term deriving from the distribution of the mixed noise in the observed US images. In image processing, TV regularization has been proven to be very useful for additive noise reduction, but it has the staircase effect. To overcome this drawback, a number of high-order (typically second-order) regularizations have been proposed in the last few years. High-order regularizations have more efficient than the TV regularization. The main motivation behind these regularizations is to overcome problems such as the staircase effect and the loss of image contrast that the TV regularization does have. In this research, we also propose an improved variational model on removing the mixed noise in real US images using a second-order regularization. In order to solve the proposed variational models, we apply the split Bregman method to propose a fast US speckle reduction algorithm for model. Numerical experiments are shown to illustrate the capability of the proposed variation models and the performance of the proposed numerical algorithms on synthetic images and real US images.

## ACKNOWLEDGEMENTS

This thesis was accomplished with the help of my thesis advisor, Assistant Professor Dr. Noppadol Chumchob. He dedicates his time to give advice and check the various mistakes in my study and research with attention as well. I appreciate every help from him.

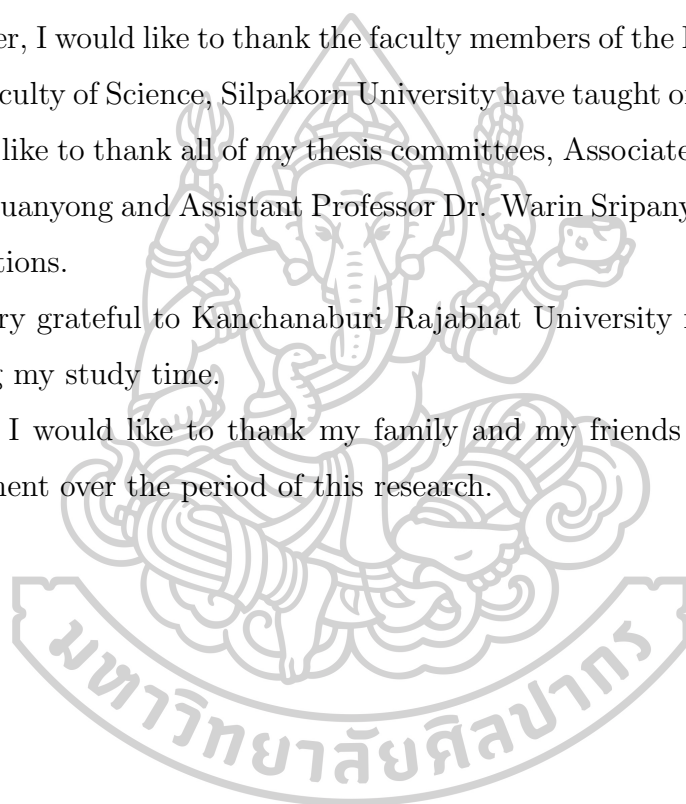
Moreover, I would like to thank the faculty members of the Department of Mathematics, Faculty of Science, Silpakorn University have taught of valuable knowledge.

I would like to thank all of my thesis committees, Associate Professor Dr. Suab-sagun Yooyuanyong and Assistant Professor Dr. Warin Sripanya for their comments and suggestions.

I am very grateful to Kanchanaburi Rajabhat University for the financial support during my study time.

Finally, I would like to thank my family and my friends for the support and encouragement over the period of this research.

Siriwan CHANKAN



# CONTENTS

<b>ABSTRACT</b>	<b>v</b>
<b>ACKNOWLEDGEMENTS</b>	<b>vi</b>
<b>LIST OF FIGURES</b>	<b>x</b>
<b>LIST OF TABLES</b>	<b>xiii</b>
<b>1 Introduction</b>	<b>2</b>
1.1 Introduction to Noise Reduction Problems . . . . .	2
1.2 Some Applications of Noise Reduction . . . . .	2
1.3 Organization of the Thesis . . . . .	3
<b>2 Mathematical preliminaries</b>	<b>5</b>
2.1 Linear Vector Space . . . . .	5
2.1.1 Normed Linear Spaces . . . . .	5
2.1.2 Convex Sets and Functions . . . . .	9
2.2 Function of Bounded Variations . . . . .	10
2.3 Inverse and Ill-posed Problems and Regularization . . . . .	11
2.3.1 Well- and Ill-Posed Problems . . . . .	11
2.3.2 Regularization . . . . .	13
2.4 Introduction to Calculus of Variations . . . . .	14
2.5 Discretization of Partial Differential Equations . . . . .	17
2.6 Iterative Solutions to System of Nonlinear Equations . . . . .	21
2.6.1 Fixed-Point Iteration Method . . . . .	21
2.6.2 Explicit Time Marching Method . . . . .	22

2.6.3	Alternating Direction Method of Multipliers . . . . .	23
2.6.4	Bregman Iteration . . . . .	24
<b>3</b>	<b>Review of Variational Models for Noise Reduction</b>	<b>25</b>
3.1	Images and Noise . . . . .	26
3.2	Variational Formulation . . . . .	27
3.3	Variational Models for Additive Noise Reduction . . . . .	27
3.4	Variational Models for Speckle Noise Reduction . . . . .	31
3.5	Numerical Solution Schemes . . . . .	34
3.5.1	Split Bregman Algorithm for the JY model . . . . .	34
3.5.2	Split Bregman Algorithm for the KKWV model . . . . .	37
3.5.3	Split Bregman Algorithm for the improved KKWV model . . . . .	39
<b>4</b>	<b>A First-Order Variational Model and Its Numerical Algorithm</b>	<b>42</b>
4.1	Introduction . . . . .	42
4.2	A New First-Order Variational Model . . . . .	43
4.2.1	Existence and Uniqueness of the Solution . . . . .	43
4.2.2	Euler-Lagrange Equation . . . . .	45
4.3	Numerical Solutions . . . . .	46
4.3.1	Numerical Discretization . . . . .	46
4.3.2	Method 1-Explicit Time Marching Method . . . . .	47
4.3.3	Method 2-Fixed-Point Iteration Method . . . . .	47
4.3.4	Method 3-Split Bregman Method . . . . .	48
4.4	Numerical Results and Discussion . . . . .	52
4.5	Conclusions . . . . .	64
<b>5</b>	<b>A Second-Order Model and Its Numerical Algorithm</b>	<b>65</b>
5.1	A New Second-Order Variational Model . . . . .	65
5.1.1	Existence and Uniqueness of the Solution . . . . .	67
5.1.2	Split Bregman Method for the New Variational Model . . . . .	68
5.2	Numerical Results and Discussion . . . . .	72
5.3	Conclusions . . . . .	82



6 Summary and Future Directions	83
REFERENCES	85
PRESENTATION AND PUBLICATIONS	91
VITA	93

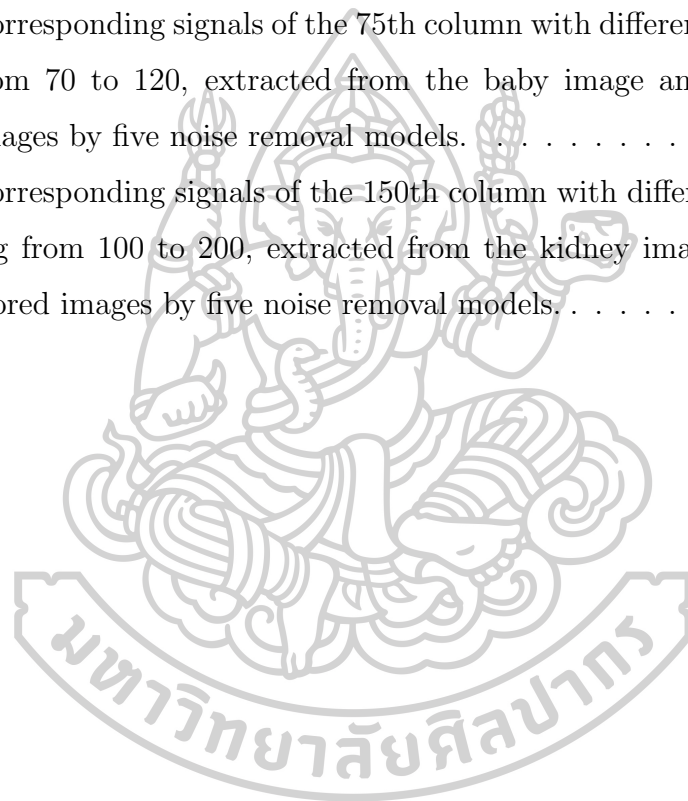


# LIST OF FIGURES

4.1	The original test images. . . . .	53
4.2	Performance comparison of the restored images by four noise removal models with $k_0 = 0.5$ and $k_1 = \frac{1}{10}$ ; (a) original image; (b) noisy image; (c)-(f) restoration results by proposed, JY, KKWV and improved KKWV models respectively. . . . .	55
4.3	Corresponding signals of one column 128 of the Ring image in figure 4.2. . . . .	55
4.4	Performance comparison of different noise removal models on the baby image. Top: The original and restored images. Bottom: the magnification of the original and restored images. . . . .	58
4.5	Performance comparison of different noise removal models on the kidney image. Top: The original and restored images. Bottom: the magnification of the original and restored images. . . . .	58
4.6	Corresponding signals of the 75th column with different rows ranging from 70 to 120, extracted from the baby image and the restored images by four noise removal models. . . . .	59
4.7	Corresponding signals of the 75th column with different rows ranging from 70 to 120, extracted from the kidney image and the restored images by the proposed model. . . . .	60
4.8	Corresponding signals of the 75th column with different rows ranging from 70 to 120, extracted from the baby image and the restored images by the JY model. . . . .	60

4.9	Corresponding signals of the 75th column with different rows ranging from 70 to 120, extracted from the baby image and the restored images by the KKWV model. . . . .	61
4.10	Corresponding signals of the 75th column with different rows ranging from 70 to 120, extracted from the baby image and the restored images by the improved KKWV model. . . . .	61
4.11	Corresponding signals of the 150th column with different rows ranging from 100 to 200, extracted from the baby image and the restored images by four noise removal models. . . . .	62
4.12	Corresponding signals of the 150th column with different rows ranging from 100 to 200, extracted from the baby image and the restored images by the proposed model. . . . .	62
4.13	Corresponding signals of the 150th column with different rows ranging from 100 to 200, extracted from the kidney image and the restored images by the JY model. . . . .	63
4.14	Corresponding signals of the 150th column with different rows ranging from 100 to 200, extracted from the kidney image and the restored images by the KKWV model. . . . .	63
4.15	Corresponding signals of the 150th column with different rows ranging from 100 to 200, extracted from the kidney image and the restored images by the improved KKWV model. . . . .	64
5.1	The original test images. . . . .	74
5.2	Linear-preservation ability test; (a) noisy image; (b)-(f) restoration results by SN-TV, SN-TL, SN-BH, SN-TC and SN-TGV models respectively. . . . .	75
5.3	Plots of 1D of the noisy and denoised images in Figure 5.2, where the x-axis presents the number of columns and the y-axis shows the value of the image intensity. . . . .	76
5.4	Surfaces of the noisy and denoised images in Figure 5.2. . . . .	76
5.5	Performance comparison of different noise removal models on the baby image; (a) original image; (b)-(f) restored images. . . . .	79

5.6	Performance comparison of different noise removal models on the baby image; (a) magnification of original image; (b)-(f) magnification of restored images. . . . .	80
5.7	Performance comparison of different noise removal models on the kidney image; (a) original image; (b)-(f) restored images. . . . .	80
5.8	Performance comparison of different noise removal models on the kidney image; (a) magnification of original image; (b)-(f) magnification of restored images. . . . .	81
5.9	Corresponding signals of the 75th column with different rows ranging from 70 to 120, extracted from the baby image and the restored images by five noise removal models. . . . .	81
5.10	Corresponding signals of the 150th column with different rows ranging from 100 to 200, extracted from the kidney image and the restored images by five noise removal models. . . . .	82



# LIST OF TABLES

4.1	Performance comparison using the average PSNR of the restored images by four noise removal models with several levels of noise strength, where the test images are corrupted with a fixed level of Gaussian noise and five different levels of Gamma noise. . . . .	54
4.2	Performance comparison using the average PSNR of the restored images by four noise removal models with several levels of noise strength, where the test images are corrupted with a fixed level of Gamma noise and four different levels of Gaussian noise. . . . .	54
4.3	Performance comparison using the average PSNR of the restored images by four noise removal models with several levels of noise strength, where the test images are corrupted with four different levels of Gaussian noise and five different levels of Gamma noise. . .	54
4.5	Performance comparison using the average PSNR of the restored images by three numerical solutions with several levels of SN strength, where the test images are corrupted with a fixed level of Gamma noise and four different levels of Gaussian noise. . . . .	56
4.6	Performance comparison using the average PSNR of the restored images by three numerical solutions with several levels of noise strength, where the test images are corrupted with four different levels of Gaussian noise and five different levels of Gamma noise. . . . .	56
4.4	Performance comparison using the average PSNR of the restored images by three numerical solutions with several levels of noise strength, where the test images are corrupted with a fixed level of Gaussian noise and five different levels of Gamma noise. . . . .	56

5.1	Comparison of PSNR by different variational models on synthetic image. . . . .	74
5.2	Comparison of PSNR testing on different levels of Gamma noise by different variational models on two images. . . . .	77
5.3	Comparison of PSNR testing on different levels of Gaussian noise by different variational models on real images. . . . .	78



# Chapter 1

## Introduction

### 1.1 Introduction to Noise Reduction Problems

Noise reduction problem is one of the most important tasks in image processing. The goal of this problem is to remove or reduce the noise contaminating in a real recorded image while preserving its important features and details. The noise in images can be caused by various factors such as sensor noise in digital cameras, compression artifacts, interference during image acquisition, and other sources of random or systematic disturbances.

### 1.2 Some Applications of Noise Reduction

There are several applications of noise reduction. Some examples are given as follows:

1. Improved image quality : Noise reduction can be used to improve the overall quality of a real recorded image by removing unwanted artifacts and improving sharpness.
2. Medical imaging : Noise reduction is important in medical imaging such as X-rays, CT scans, MRI and Ultrasound (US), as it improves image quality and accuracy of diagnosis.
3. Astrophotography : Noise reduction is crucial in astrophotography, where a

real recorded image is often captured in low light conditions and high ISO setting, resulting in a lot of noise.

4. Surveillance : In surveillance applications, noise reduction can be used to improve the clarity of recorded images captured by security cameras, making it easier to detect suspects and other important details.
5. Art restoration : In art restoration, noise reduction can be used to remove unwanted artifacts and enhance the quality of the given image, making it easier record the original artwork.

### 1.3 Organization of the Thesis

The remaining parts of this thesis are arranged as follows:

In Chapter 2, we review some necessary mathematical tools to be used in this thesis. It includes:

- Linear vector space, normed linear spaces, convex sets and functions.
- Function of bounded variations.
- Inverse and ill-posed problems and regularization.
- Introduction into calculus of variations.
- Discretization of partial differential equations.
- Iterative solutions to system of nonlinear equations.

In Chapter 3, we review many variational models for noise reduction and numerical solution schemes. It includes:

- Images and noise.
- Variational formulation.
- Variational models for additive noise reduction.
- Variational models for speckle noise reduction.



- Numerical solution schemes, numerical discretization, basic iterative methods, split Bregman method.

In Chapter 4, we introduce a new first-order model and its numerical algorithm for the mixed noise reduction of real US images. It includes:

- Details of the proposed variational model for removing the mixed noise in real US images.
- Details of the proposed numerical algorithm, including a finite difference discretization and its numerical solutions.
- Tests showing the effectiveness of the proposed model and numerical algorithms, including several comparisons with other noise reduction models and numerical solutions.

In Chapter 5, we propose a new second-order model and its numerical algorithm for the mixed noise reduction of real US images. It includes:

- Details of the proposed variational model for removing the combination of additive and speckle noise from real US images.
- Details of the proposed numerical method, including the split Bregman iteration scheme.
- Tests showing the robustness of the new second-order model and the proposed numerical algorithm.

In Chapter 6, we give our conclusion and future research direction.

# Chapter 2

## Mathematical preliminaries

In this chapter, we review some necessary mathematical tools.

### 2.1 Linear Vector Space

In this section, we review linear vector space, including normed spaces and convex sets and functions.

#### 2.1.1 Normed Linear Spaces

Here, we review some basic notions, theorems, and examples in normed linear spaces. For more details, we refer the reader to [67].

**Definition 2.1** (Field). *Let  $\mathbf{K}$  be a subset of the complex numbers  $\mathbb{C}$ . We say that  $\mathbf{K}$  is a field if it satisfies the following conditions:*

1. *If  $x, y \in \mathbf{K}$ ,  $x + y$  and  $xy$  are also elements of  $\mathbf{K}$ .*
2. *If  $x \in \mathbf{K}$ ,  $-x$  is also an element of  $\mathbf{K}$ . If furthermore  $x \neq 0$ ,  $x^{-1}$  is also an element of  $\mathbf{K}$ .*
3. *The elements 0 and 1 are elements of  $\mathbf{K}$ .*

**Example 2.2.**  $\mathbb{R}$  and  $\mathbb{C}$  are both fields.

**Definition 2.3** (Linear Vector Space). *Let  $\mathbf{K}$  be a field. We say that  $\mathbf{V}$  is a linear vector space over the field  $\mathbf{K}$  if it satisfies the following conditions:*

1. If  $\mathbf{u}, \mathbf{v} \in \mathbf{V}$ ,  $\mathbf{u} + \mathbf{v} = \mathbf{v} + \mathbf{u}$ .
2. If  $\mathbf{u}, \mathbf{v}, \mathbf{w} \in \mathbf{V}$ ,  $(\mathbf{u} + \mathbf{v}) + \mathbf{w} = \mathbf{u} + (\mathbf{v} + \mathbf{w})$ .
3. There is an element of  $\mathbf{V}$ , denoted by  $\mathbf{0}$ , such that  $\mathbf{0} + \mathbf{u} = \mathbf{u} + \mathbf{0} = \mathbf{u}$  for all elements  $\mathbf{u} \in \mathbf{V}$ .
4. If  $\mathbf{u} \in \mathbf{V}$ , there exists an element  $-\mathbf{u} \in \mathbf{V}$  such that  $\mathbf{u} + (-\mathbf{u}) = \mathbf{0}$ .
5. If  $c \in \mathbf{K}$  and  $\mathbf{u}, \mathbf{v} \in \mathbf{V}$ ,  $c(\mathbf{u} + \mathbf{v}) = c\mathbf{u} + c\mathbf{v}$ .
6. If  $a, b \in \mathbf{K}$  and  $\mathbf{u} \in \mathbf{V}$ ,  $(a + b)\mathbf{u} = a\mathbf{u} + b\mathbf{u}$ .
7. If  $a, b \in \mathbf{K}$  and  $\mathbf{u} \in \mathbf{V}$ ,  $(ab)\mathbf{u} = a(b\mathbf{u})$ .
8. If  $\mathbf{u} \in \mathbf{V}$ , we have  $1 \cdot \mathbf{u} = \mathbf{u}$  (here 1 is the number one).

We can notice that a linear vector space  $\mathbf{V}$  over the field  $\mathbf{K}$  is a set of objects which can be added and multiplied by elements of  $\mathbf{K}$ . In other words, the sum of two elements of  $\mathbf{V}$  is also an element of  $\mathbf{V}$  and the product of an element of  $\mathbf{V}$  by an element of  $\mathbf{K}$  is also an element of  $\mathbf{V}$ .

**Example 2.4.** Let  $\mathbf{V} = \mathbf{K}^n$  be the set of  $n$ -tuples of elements of  $\mathbf{K}$ . Then  $\mathbf{V}$  is a linear vector space over the field  $\mathbf{K}$ .

**Definition 2.5** (Linear Subspace). Let  $\mathbf{V}$  be a vector space over the field  $\mathbf{K}$  and  $\mathbf{W}$  be a subset of  $\mathbf{V}$ . We say that  $\mathbf{W}$  is a linear subspace of  $\mathbf{V}$  if it satisfies the following conditions:

1. If  $\mathbf{v}, \mathbf{w} \in \mathbf{W}$ ,  $\mathbf{v} + \mathbf{w}$  is also an element of  $\mathbf{W}$ .
2. If  $\mathbf{v} \in \mathbf{W}$  and  $c \in \mathbf{K}$ ,  $c\mathbf{v}$  is also an element of  $\mathbf{W}$ .
3. The element  $\mathbf{0}$  of  $\mathbf{V}$  is also an element of  $\mathbf{W}$ .

**Example 2.6.** Let  $\mathbf{V} = \mathbf{K}^n$  and  $\mathbf{W}$  be the set of vectors in  $\mathbf{V}$  whose last coordinate is equal to 0. Then  $\mathbf{W}$  is a linear subspace of  $\mathbf{V}$ , which can be identified with  $\mathbf{K}^{n-1}$ .

**Definition 2.7** (Norm). Let  $\mathbf{V}$  be a vector space over the field  $\mathbf{K}$ . We say that a nonnegative-valued scalar function  $\|\cdot\|$  is a norm on  $\mathbf{V}$  if it satisfies the following conditions:

1.  $\|\mathbf{u}\| = 0$  if and only if  $\mathbf{u} = \mathbf{0} \in \mathbf{V}$ .
2.  $\|\lambda\mathbf{u}\| = |\lambda|\|\mathbf{u}\|$ , for all  $\lambda \in \mathbf{K}$  and all  $\mathbf{u} \in \mathbf{V}$ .
3.  $\|\mathbf{u} + \mathbf{v}\| \leq \|\mathbf{u}\| + \|\mathbf{v}\|$ , for all  $\mathbf{u}, \mathbf{v} \in \mathbf{V}$ .

**Definition 2.8** (Seminorm). Let  $\mathbf{V}$  be a vector space over the field  $\mathbf{K}$ . We say that a nonnegative-valued scalar function  $\|\cdot\|$  is a seminorm on  $\mathbf{V}$  if it satisfies the following conditions:

1.  $\|\lambda\mathbf{u}\| = |\lambda|\|\mathbf{u}\|$ , for all  $\lambda \in \mathbf{K}$  and all  $\mathbf{u} \in \mathbf{V}$ .
2.  $\|\mathbf{u} + \mathbf{v}\| \leq \|\mathbf{u}\| + \|\mathbf{v}\|$ , for all  $\mathbf{u}, \mathbf{v} \in \mathbf{V}$ .

**Example 2.9.** Let  $\mathbf{x} = (x_1, x_2, \dots, x_n)$  be a vector. Then well-known examples of the vector norm are as follows:

$$\|\mathbf{x}\|_\infty = \max_{1 \leq i \leq n} |x_i|, \text{ (} l^\infty \text{-norm)} \quad (2.1)$$

$$\|\mathbf{x}\|_1 = \sum_{i=1}^n |x_i|, \text{ (} l^1 \text{-norm)} \quad (2.2)$$

$$\|\mathbf{x}\|_2 = \left( \sum_{i=1}^n |x_i|^2 \right)^{1/2}, \text{ (} l^2 \text{-norm)}. \quad (2.3)$$

The above examples are special cases of  $l^p$ -norm which is defined by

$$\|\mathbf{x}\|_p = \left( \sum_{i=1}^n |x_i|^p \right)^{1/p}, \text{ (} l^p \text{-norm)}. \quad (2.4)$$

**Example 2.10** ( $L^p$ -norm). Let  $f$  be a function defined on a domain  $\Omega$  and  $1 \leq p \leq \infty$ . The  $L^p$ -norm of  $f$  on  $\Omega$  is defined by

$$\|f\|_{L^p} = \left( \int_{\Omega} |f(\mathbf{x})|^p d\mathbf{x} \right)^{1/p}. \quad (2.5)$$

This is a generalization of the previous example. The special case when  $p = \infty$  is defined by

$$\|f\|_{L^\infty} = \sup_{\mathbf{x}} |f(\mathbf{x})|. \quad (2.6)$$

**Example 2.11.** Let  $\mathbf{V}$  be a vector space over the field  $\mathbf{K}$ .  $\|\mathbf{u}\| = 0$  for all  $\mathbf{u} \in \mathbf{V}$  is a trivial seminorm.

**Definition 2.12** (Normed Linear Space). A normed linear space is a pair  $(\mathbf{V}, \|\cdot\|)$  where  $\mathbf{V}$  is a vector space over the field  $\mathbf{K}$  and  $\|\cdot\|$  is a norm on  $\mathbf{V}$ .

**Definition 2.13** (Inner Product). Let  $\mathbf{V}$  be a vector space over the field  $\mathbf{K}$ . We say that a function  $\langle \cdot, \cdot \rangle : \mathbf{V} \times \mathbf{V} \rightarrow \mathbf{K}$  is an inner product on  $\mathbf{V}$  if it satisfies the following conditions:

1.  $\langle \mathbf{u}, \mathbf{u} \rangle \geq 0$ , for all  $\mathbf{u} \in \mathbf{V}$ .
2.  $\langle \mathbf{u}, \mathbf{u} \rangle = 0$  if and only if  $\mathbf{u} = \mathbf{0} \in \mathbf{V}$ .
3.  $\langle \mathbf{u} + \mathbf{v}, \mathbf{w} \rangle = \langle \mathbf{u}, \mathbf{w} \rangle + \langle \mathbf{v}, \mathbf{w} \rangle$ , for all  $\mathbf{u}, \mathbf{v}, \mathbf{w} \in \mathbf{V}$ .
4.  $\langle \lambda \mathbf{u}, \mathbf{v} \rangle = \lambda \langle \mathbf{u}, \mathbf{v} \rangle$ , for all  $\lambda \in \mathbf{K}$  and all  $\mathbf{u}, \mathbf{v} \in \mathbf{V}$ .
5.  $\langle \mathbf{u}, \mathbf{v} \rangle = \overline{\langle \mathbf{v}, \mathbf{u} \rangle}$ , for all  $\mathbf{u}, \mathbf{v} \in \mathbf{V}$ .

**Example 2.14.** Two examples of the inner product are as follows:

- The Euclidean inner product on  $\mathbf{K}^n$  is defined by

$$\langle (w_1, w_2, \dots, w_n), (z_1, z_2, \dots, z_n) \rangle = w_1 \bar{z}_1 + w_2 \bar{z}_2 + \dots + w_n \bar{z}_n, \quad (2.7)$$

where  $w_i, z_i, \bar{z}_i \in \mathbf{K}$  for all  $1 \leq i \leq n$ .

- An inner product on the vector space of continuous real-valued functions on the interval  $[-1, 1]$  can be defined by

$$\langle f, g \rangle = \int_{-1}^1 f(\mathbf{x})g(\mathbf{x})dx. \quad (2.8)$$

**Definition 2.15** (Cauchy Sequence and Completeness). We say that a sequence  $\{x_n\}_{n=1}^{\infty}$  in a normed linear space  $\mathbf{V}$  is a Cauchy sequence if given any  $\epsilon > 0$ , there exists  $N_0 \in \mathbb{N}$  such that

$$\|x_n - x_m\| < \epsilon, \text{ for all } n, m > N_0. \quad (2.9)$$

In addition, we say that a normed linear space  $\mathbf{V}$  is complete if every Cauchy sequence in  $\mathbf{V}$  converges to an element in  $\mathbf{V}$ .

**Example 2.16.** Let  $a, b \in \mathbb{R}$ .  $\mathbf{V} = [a, b]$  is complete but  $\mathbf{V} = (a, b)$  is not complete.

**Definition 2.17** (Banach Space and Hilbert Space). *A complete normed linear space is called a Banach space. A complete inner product space concerning the norm induced by the inner product is called a Hilbert space.*

**Example 2.18.** *The space  $L^2(\Omega)$  with the inner product defined by*

$$\langle f, g \rangle_{L^2(\Omega)} = \int_{\Omega} f(\mathbf{x})g(\mathbf{x})d\mathbf{x} \quad (2.10)$$

*is a Hilbert space. It is also a Banach space.*

**Definition 2.19** (Linear Mapping). *Let  $\mathbf{V}$  and  $\mathbf{W}$  be vector spaces over the same field  $\mathbf{K}$ . We say that a mapping  $\mathcal{L} : \mathbf{V} \rightarrow \mathbf{W}$  is linear if it satisfies the following conditions:*

1.  $\mathcal{L}(\mathbf{u} + \mathbf{v}) = \mathcal{L}(\mathbf{u}) + \mathcal{L}(\mathbf{v})$ , for all  $\mathbf{u}, \mathbf{v} \in \mathbf{V}$ .
2.  $\mathcal{L}(\lambda\mathbf{u}) = \lambda\mathcal{L}(\mathbf{u})$ , for all  $\lambda \in \mathbf{K}$  and all  $\mathbf{u} \in \mathbf{V}$ .

**Example 2.20.** *Let  $\mathbf{V} = \mathbb{R}^3$  and  $\mathbf{W} = \mathbb{R}^2$ . Define a projective mapping  $\mathcal{L} : \mathbf{V} \rightarrow \mathbf{W}$ , namely  $\mathcal{L}(\mathbf{x}, \mathbf{y}, \mathbf{z}) = (\mathbf{x}, \mathbf{y})$ . Then the mapping  $\mathcal{L}$  is a linear mapping.*

## 2.1.2 Convex Sets and Functions

**Definition 2.21** (Convex Set). *Let  $S$  be a set. We say that  $S$  is a convex set if it satisfies the following condition:*

$$\lambda u + (1 - \lambda)v \in S; \text{ for all } \lambda \in [0, 1] \text{ and all } u, v \in S. \quad (2.11)$$

**Definition 2.22** (Convex Function and Strict Convex Function). *Let  $S$  be a nonempty convex set. We say that  $f : S \rightarrow \mathbb{R}$  is convex on  $S$  if it satisfies the following condition:*

$$f(\lambda u + (1 - \lambda)v) \leq \lambda f(u) + (1 - \lambda)f(v); \text{ for all } \lambda \in (0, 1) \text{ and all } u, v \in S. \quad (2.12)$$

*In addition, we say that  $f : S \rightarrow \mathbb{R}$  is strictly convex on  $S$  if it satisfies the following condition:*

$$f(\lambda u + (1 - \lambda)v) < \lambda f(u) + (1 - \lambda)f(v); \text{ for all } \lambda \in (0, 1) \text{ and all } u \neq v \in S. \quad (2.13)$$

**Example 2.23.** Let  $S$  be  $[0, \pi]$ . Then  $f(x) = x^2$  is convex and strictly convex on  $S$ . However,  $f(x) = \sin(x)$  is not convex on  $S$ .

**Example 2.24.** Let  $S \subset \mathbb{R}^n$  be a nonempty subset. The indicator function  $I_S : \mathbb{R}^n \rightarrow \mathbb{R} \cup \{\infty\}$  is defined by

$$I_S(x) := \begin{cases} 0 & \text{if } x \in S, \\ +1 & \text{otherwise.} \end{cases} \quad (2.14)$$

Obviously,  $I_S$  is convex if and only if  $S$  is convex.

## 2.2 Function of Bounded Variations

In this section, we give a short summary of the theory of function of bounded variations. As usual  $\Omega$  denotes an open domain in  $\mathbb{R}^d$ . For more details, we refer the reader to [1, 47] which we also follow here.

Let  $\Omega$  be a bounded convex region in  $\mathbb{R}^d$ ,  $d = 1, 2$ , or  $3$ , whose boundary  $\partial\Omega$  is Lipschitz continuous. Let  $|x| = \sqrt{\sum_{i=1}^d x_i^2}$  denote the Euclidean norm on  $\mathbb{R}^d$ . Denote the norm on the Banach spaces  $L^p(\Omega)$  by  $\|\cdot\|_{L^p(\Omega)}$ ,  $1 \leq p \leq \infty$ .

The BV semi-norm or total variation (TV) is given by [25]

$$J_0(u) = \sup_{v \in \mathcal{V}} \int_{\Omega} (-u \operatorname{div} v) dx, \quad (2.15)$$

where the set of test functions

$$\mathcal{V} = \{v \in C_0^1(\Omega; \mathbb{R}^d) : |v(x)| \leq 1 \text{ for all } x \in \Omega\}. \quad (2.16)$$

If  $u \in C^1(\Omega)$ , one can show using integration by parts that

$$J_0(u) = \int_{\Omega} |\nabla u| dx. \quad (2.17)$$

By a standard denseness argument, this also applies for  $u$  in the Sobolev space  $W^{1,1}(\Omega)$ .

The space of functions of bounded variation on  $\Omega$  is defined by

$$\operatorname{BV}(\Omega) = \{u \in L^1(\Omega) : J_0(u) < \infty\}. \quad (2.18)$$

The BV norm is given by

$$\|u\|_{\text{BV}} = \|u\|_{L^1(\Omega)} + J_0(u). \quad (2.19)$$

$\text{BV}(\Omega)$  is complete, and hence a Banach space, with respect to this norm. The Sobolev space  $W^{1,1}(\Omega)$  is a proper subset of  $\text{BV}(\Omega)$ . Note that for  $\Omega$  bounded,  $L^p(\Omega) \subset L^1(\Omega)$  for  $p > 1$ . From the definition,  $\text{BV}(\Omega) \subset L^1(\Omega)$ . It is shown in [1] that  $\text{BV}(\Omega) \subset L^p(\Omega)$  for  $1 \leq p \leq d/(d-1)$ .

Let  $T$  be a functional defined on  $L^p(\Omega)$  with values in the extended reals. Theorem 2.20 below, guarantees the existence and uniqueness of minimizers of the unconstrained minimization problem

$$\min_{u \in L^p(\Omega)} T(u). \quad (2.20)$$

Define  $T$  to be BV-coercive if

$$T(u) \rightarrow +\infty \text{ whenever } \|u\|_{\text{BV}} \rightarrow \infty. \quad (2.21)$$

Note that “lower level sets”  $\{u \in L^p(\Omega) : T(u) \leq a\}$ , where  $a \geq 0$ , are BV-bounded.

We recall the following theorem due to Acar and Vogel [1].

**Theorem 2.25** (Existence and Uniqueness of Minimizers [1]). *Suppose that  $T$  is BV-coercive. If  $1 \leq p < d/(d-1)$  and  $T$  is lower semicontinuous, then problem (2.20) has a solution. If in addition  $p = d/(d-1)$ , dimension  $d \geq 2$ , and  $T$  is weakly lower semicontinuous, then a solution also exists. In either case, the solution is unique if  $T$  is strictly convex.*

## 2.3 Inverse and Ill-posed Problems and Regularization

### 2.3.1 Well- and Ill-Posed Problems

In the last fifty years, inverse problems have been widely applied in geophysics, oceanography, signal processing, machine learning, medical imaging and many other fields [60]. Forward problems start with the causes and calculate the results but



inverse problems start with the results and calculate the causes. For example, in image denoising, we want to get the clean image from the recorded image and in CT scans, we want to get the CT image from the data source. However, inverse problems are usually ill-posed. The classical definition of an ill-posed problem is defined by Hadamard in 1902 [27]: if one of the following conditions can not be satisfied:

1. the solution exists;
2. the solution is unique;
3. the solution's behavior changes continuously with the initial conditions.

A problem is well-posed if it is not ill-posed.

**Example 2.26.** Here, we use several simple examples to illustrate the ill-posed problems and well-posed problems. Let us consider the following system of linear equations:

$$A\mathbf{x} = \mathbf{b}, \quad (2.22)$$

where  $A \in \mathbb{R}^{2 \times 2}$  is a matrix and  $\mathbf{b} \in \mathbb{R}^{2 \times 1}$  is a vector.

- If  $A = \begin{pmatrix} 3 & 4 \\ 3 & 4 \end{pmatrix}$  and  $\mathbf{b} = \begin{pmatrix} 2 \\ 7 \end{pmatrix}$ , this problem does not exist a solution and it is ill-posed.
- If  $A = \begin{pmatrix} 3 & 4 \\ 3 & 4 \end{pmatrix}$  and  $\mathbf{b} = \begin{pmatrix} 2 \\ 2 \end{pmatrix}$ , this problem has infinite solutions  $\mathbf{x} = \begin{pmatrix} \frac{2-4k}{3} \\ k \end{pmatrix}$ ,  $k \in \mathbb{R}$  and it is ill-posed.
- If  $A = \begin{pmatrix} 2.0002 & 1.9998 \\ 1.9998 & 2.0002 \end{pmatrix}$  and  $\mathbf{b} = \begin{pmatrix} 4 \\ 4 \end{pmatrix}$ , this problem has only one solution  $\mathbf{x} = \begin{pmatrix} 1 \\ 1 \end{pmatrix}$ . If we add a perturbation  $\delta\mathbf{b} = \begin{pmatrix} 2 \times 10^{-4} \\ -2 \times 10^{-4} \end{pmatrix}$  to  $\mathbf{b}$ , the solution changes to  $\bar{\mathbf{x}} = \begin{pmatrix} 1.5 \\ 0.5 \end{pmatrix}$ . Here, we can find that the relative error of the

solution  $\frac{\|\bar{\mathbf{x}} - \mathbf{x}\|_\infty}{\|\mathbf{x}\|_\infty}$  is 10,0000 times of the relative error of the right hand side  $\frac{\|\delta \mathbf{b}\|_\infty}{\|\mathbf{b}\|_\infty}$ . So it is ill-posed.

- If  $A = \begin{pmatrix} 3 & 4 \\ 5 & 1 \end{pmatrix}$  and  $\mathbf{b} = \begin{pmatrix} 7 \\ 6 \end{pmatrix}$ , this problem has a unique solution  $\mathbf{x} = \begin{pmatrix} 1 \\ 1 \end{pmatrix}$ . The solution depends continuously on the right hand side  $\mathbf{b}$  and it is well-posed.

### 2.3.2 Regularization

Since it is very difficult to deal with the ill-posed problem, Andrei N. Tikhonov in [58] introduced the concept of the regularization which used a series of well-posed problems to approximate the ill-posed problem.

**Example 2.27.** Let us consider the following least-square problem:

$$\min_{\mathbf{x}} \|\mathbf{A}\mathbf{x} - \mathbf{b}\|_2^2 \quad (2.23)$$

where  $A \in \mathbb{R}^{m \times n}$  is a matrix and  $\mathbf{b} \in \mathbb{R}^{m \times 1}$  is a vector. The normal equation of (2.23) is

$$A^T A \mathbf{x} = A^T \mathbf{b}. \quad (2.24)$$

If  $n > m$ , (2.24) may have no solution or infinite solutions. Here, we try to find the solution with some properties, for example, it has the smallest 2-norm. Then we can convert the problem (2.23) into the following problem:

$$\min_{\mathbf{x}} \|\mathbf{A}\mathbf{x} - \mathbf{b}\|_2^2 + \alpha \|\mathbf{x}\|_2^2. \quad (2.25)$$

Here, the first term is the fitting term and the second term is the regularizer.  $\alpha$  is a nonnegative parameter to balance the weight of these two terms. In order to minimize (2.25), we only need to solve the following linear system:

$$(A^T A + \alpha I) \mathbf{x} = A^T \mathbf{b}. \quad (2.26)$$

Since  $\alpha > 0$  and  $A^T A + \alpha I$  is symmetric and positive definite, (2.26) has only one solution. Hence, (2.25) is well-posed.

## 2.4 Introduction to Calculus of Variations

A functional is a mapping from a vector space of functions into the real numbers. The calculus of variations is concerned with finding maxima and minima of functionals. In this section, we introduce the basic notions about the calculus of variations, such as first variation, Euler-Lagrange equation, and the direct method to prove the existence. For more details, we refer to [67].

### First Variation and Euler-Lagrange Equation

In the general case, Tikhonov regularization replaces

$$\min_u \mathcal{D}(u) \tag{2.27}$$

by

$$\min_u \{ \mathcal{J}(u) = \mathcal{D}(u) + \alpha \mathcal{R}(u) \}, \tag{2.28}$$

where  $\mathcal{D}(u)$  is a fitting term and  $\mathcal{R}(u)$  is a regularizer which can rule out the unwanted solutions according to the prior information. Firstly, we define the local extrema for the functional.

**Definition 2.28** (Neighborhood). *The neighborhood of  $u \in \mathcal{U}$  is defined by*

$$N_\epsilon(u) = \{ \hat{u} \in \mathcal{U} \mid \|u - \hat{u}\| \leq \epsilon \}. \tag{2.29}$$

**Definition 2.29** (Local Extrema). *Let  $\mathcal{J} : \mathcal{U} \rightarrow \mathbb{R}$  be a functional defined on the functionspace  $(\mathcal{U}, \|\cdot\|)$ . We say that  $J$  has a local maximum at  $u \in \mathcal{U}$  if the following condition is satisfied:*

$$\mathcal{J}(\hat{u}) \leq \mathcal{J}(u) \text{ for all } \hat{u} \in N_\epsilon(u). \tag{2.30}$$

*We say that  $\mathcal{J}$  has a local minimum at  $u \in \mathcal{U}$  if  $u \in \mathcal{U}$  is a local maximum for  $-\mathcal{J}$ . Often,  $\mathcal{U}$  is a set of functions with certain boundary conditions.*

Next, we illustrate the first variation and the Euler-Lagrange equation through a particular class of problems. Let  $\mathcal{J} : C^2[x_0, x_1] \rightarrow \mathbb{R}$  be a functional defined by

$$\mathcal{J}(u) = \int_{x_0}^{x_1} f(x, u, x') dx, \tag{2.31}$$

where  $f$  is a function whose partial derivatives with respect to  $x$ ,  $u$  and  $u'$  are second-order continuous. In addition, let  $u_0, u_1$  be real numbers and  $u(x_0) = u_0, u(x_1) = u_1$ . Then

$$\mathcal{U} = \{u \in C^2[x_0, x_1] : u(x_0) = u_0 \text{ and } u(x_1) = u_1\}. \quad (2.32)$$

For simplifying the analysis, we set

$$\mathcal{H} = \{\eta \in C^2[x_0, x_1] : \eta(x_0) = \eta(x_1) = 0\}. \quad (2.33)$$

Assume that  $\mathcal{J}$  has a local maximum at  $u$ . Then there exists  $\epsilon > 0$  such that  $\mathcal{J}(\hat{u}) \leq \mathcal{J}(u)$  for all  $\hat{u} \in \mathcal{N}_\epsilon(u)$ . For any  $\hat{u} \in \mathcal{U}$  there is an  $\eta \in \mathcal{H}$  such that  $\hat{u} = u + \epsilon\eta$ . For small  $\epsilon$ , Taylor's theorem implies that

$$\begin{aligned} f(x, \hat{u}, \hat{u}') &= f(x, u + \epsilon\eta, u' + \epsilon\eta') \\ &= f(x, u, u') + \epsilon \left( \eta \frac{\partial f}{\partial u} + \eta' \frac{\partial f}{\partial u'} \right) + O(\epsilon^2). \end{aligned} \quad (2.34)$$

Here, we regard  $f$  as a function of the three independent variables  $x, u$  and  $u'$  and the partial derivatives in the above expression are all evaluated at the point  $x, u$  and  $u'$ . Then we have

$$\mathcal{J}(\hat{u}) - \mathcal{J}(u) = \int_{x_0}^{x_1} f(x, \hat{u}, \hat{u}') dx - \int_{x_0}^{x_1} f(x, u, u') dx \quad (2.35)$$

$$= \epsilon \int_{x_0}^{x_1} \left( \eta \frac{\partial f}{\partial u} + \eta' \frac{\partial f}{\partial u'} \right) dx + O(\epsilon^2). \quad (2.36)$$

The quantity

$$\delta\mathcal{J}(\eta, u) = \int_{x_0}^{x_1} \left( \eta \frac{\partial f}{\partial u} + \eta' \frac{\partial f}{\partial u'} \right) dx \quad (2.37)$$

is defined as the first variation of  $\mathcal{J}$ . For small  $\epsilon$ , the sign of  $\mathcal{J}(\hat{u}) - \mathcal{J}(u)$  is determined by the sign of the first variation, unless  $\delta\mathcal{J}(\eta, u) = 0$  for all  $\eta \in \mathcal{H}$ . Since  $u \in \mathcal{U}$  is a local maximum of  $\mathcal{J}$ ,  $\mathcal{J}(\hat{u}) - \mathcal{J}(u)$  does not change sign for any  $\hat{u} \in \mathcal{N}_\epsilon(u)$ . Hence, if  $\mathcal{J}(u)$  is a local maximum then

$$\delta\mathcal{J}(\eta, u) = \int_{x_0}^{x_1} \left\{ \eta \frac{\partial f}{\partial u} + \eta' \frac{\partial f}{\partial u'} \right\} dx = 0 \quad (2.38)$$

for all  $\eta \in \mathcal{H}$ . In addition, if  $\mathcal{J}$  has a local minimum at  $u \in \mathcal{U}$ , (2.38) must also be satisfied. If  $u$  satisfies (2.38) for all  $\eta \in \mathcal{H}$ , we say that  $\mathcal{J}$  is stationary at  $u$ .

Furthermore, by employing the integration by parts and boundary conditions  $\eta(x_0) = \eta(x_1) = 0$ , (2.38) can be rewritten into the following formulation

$$\int_{x_0}^{x_1} \eta \left( \frac{\partial f}{\partial u} - \frac{d}{dx} \left( \frac{\partial f}{\partial u'} \right) \right) dx = 0. \quad (2.39)$$

Then by applying the fundamental lemma of the calculus of variations [37], we conclude the following theorem:

**Theorem 2.30** (Theorem 2.2.3 in [12]). *Let  $\mathcal{J} : C^2[x_0, x_1] \rightarrow \mathbb{R}$  be a functional defined by*

$$\mathcal{J}(u) = \int_{x_0}^{x_1} f(x, u, u') dx \quad (2.40)$$

where  $f$  has second-order continuous partial derivatives with respect to  $x, u$  and  $u'$  and  $x_0 < x_1$ . Let

$$\mathcal{U} = \{u \in C^2[x_0, x_1] : u(x_0) = u_0 \text{ and } u(x_1) = u_1\}, \quad (2.41)$$

where  $u_0$  and  $u_1$  are given real numbers. If  $u \in \mathcal{U}$  is an extrema of  $\mathcal{J}$ , then

$$\frac{\partial f}{\partial u} - \frac{d}{dx} \left( \frac{\partial f}{\partial u'} \right) = 0 \quad (2.42)$$

for all  $x \in [x_0, x_1]$  (2.42) is a second-order ordinary differential equation that any extrema  $u$  must satisfy. This differential equation is called the Euler-Lagrange (EL) equation.

**Example 2.31.** Consider the following functional defined by

$$J(u) = \int_0^\pi (u'^2 - ku^2) dx, \quad (2.43)$$

with boundary conditions  $u(0) = 0$  and  $u(\pi) = 0$ . If  $u$  is an extrema for  $\mathcal{J}$ , then its EL equation is

$$u'' + ku = 0. \quad (2.44)$$

The general solution for the EL equation is

$$u(x) = c_1 \cos(\sqrt{k}x) + c_2 \sin(\sqrt{k}x). \quad (2.45)$$

Combining with the boundary conditions, we get an infinite number of extrema:  $u(x) = c_2 \sin(\sqrt{k}x)$ .

To find the solution of the model (2.28), we use the calculus of variations leading to the EL equation for  $u$ . In noise reduction problem, the EL equation is always a nonlinear partial differential equation. Thus, the EL equation is apparently difficult in developing an accurate numerical solver and then difficult to solve. So, standard numerical algorithms are not appropriate. In this thesis, we introduce two numerical algorithms to solve the associated EL equations of the proposed models.

## 2.5 Discretization of Partial Differential Equations

In the numerical implementation for solving the EL equation resulting from the variational problem (2.28), we must discretize the continuous problem into the discrete problem since the computer only deals with the discrete data. How to discretize a continuous problem is very important because a proper discretization may affect the rate of the convergence and an improper discretization may lead to a bad result or even divergence.

There exist several ways to discretize a continuous problem, including the finite element method, the finite volume method, and the finite difference method. For image noise reduction problem, since the domain of the image is usually rectangular and the intensity values of the image are uniformly distributed in this domain, the natural way is to choose the finite difference method to discretize this domain. This domain is denoted by  $\Omega \in \mathbb{R}^d$ . For simplicity, in this section, we only consider the two-dimensional case, namely,  $d = 2$  and  $\Omega \in \mathbb{R}^2$ . Here, we set  $\Omega = [a, b] \times [c, d]$ . We discretize  $\Omega$  into  $n_1 \times n_2$  cells of size  $h_1$  in  $x$  direction and  $h_2$  in  $y$  direction. Employing a cartesian mesh, the lengths of the intervals in  $x$  and  $y$  direction are  $h_1 = (b - a)/n_1$  and  $h_2 = (d - c)/n_2$  respectively.

In this thesis, we use the so called vertex centered discretization. The grids are located at the vertex of the cells. There are  $(n_1 + 1) \times (n_2 + 1)$  grid points including points on the boundary and the position of the grid point  $(i, j)$  is  $(a + ih_1, c + jh_2)$  for  $0 \leq i \leq n_1$  and  $0 \leq j \leq n_2$ . For more details, we refer to [67].

In order to solve the variational models using the so called split Bregman (SB)

method to be introduced in the next section and the next three chapter, we shall present the finite difference approximations of the first-, second- and fourth-order derivative operators. They are respectively  $\partial_x^+$ ,  $\partial_x^-$ ,  $\partial_y^+$ ,  $\partial_y^-$ ,  $\partial_x^+ \partial_x^+$ ,  $\partial_x^+ \partial_x^-$ ,  $\partial_y^- \partial_y^+$ ,  $\partial_y^+ \partial_y^-$ ,  $\partial_y^+ \partial_x^+$ ,  $\partial_x^+ \partial_y^+$ ,  $\partial_x^+ \partial_y^-$ ,  $\partial_x^- \partial_y^+$ ,  $\partial_x^- \partial_y^-$ ,  $\partial_x^+ \partial_x^- \partial_x^- \partial_x^+$ ,  $\partial_y^+ \partial_y^- \partial_y^- \partial_y^+$ ,  $\partial_y^- \partial_x^+ \partial_y^+ \partial_x^+$ , and  $\partial_x^- \partial_y^- \partial_x^+ \partial_y^+$ . Here the gradient, Hessian matrix and symmetrized derivative can be discretized as follows:

$$\nabla u = \begin{pmatrix} \partial_x^+ u \\ \partial_y^+ u \end{pmatrix}, \quad (2.46)$$

$$\nabla^2 u = \begin{pmatrix} \partial_x^- \partial_x^+ u & \partial_y^+ \partial_x^+ u \\ \partial_x^+ \partial_y^+ u & \partial_y^- \partial_y^+ u \end{pmatrix}, \quad (2.47)$$

$$\epsilon(\mathbf{p}) = \begin{pmatrix} \partial_x^- p_1 & \frac{\partial_y^- p_1 + \partial_x^- p_2}{2} \\ \frac{\partial_y^- p_1 + \partial_x^- p_2}{2} & \partial_y^- p_2 \end{pmatrix}. \quad (2.48)$$

We note first that  $\partial_x \partial_y u$  should be equal to  $\partial_y \partial_x u$  in the Hessian matrix  $\nabla^2 u$ , so it is necessary to define its discrete form such that  $\partial_x^+ \partial_y^+ u = \partial_y^+ \partial_x^+ u$  in (2.47). We also note that the periodic boundary conditions will be applied with these discretizations because it is able to preserve jumps and image contrasts and allows fast numerical computations.

From now on, we assume  $\Omega = [1, M] \times [1, N]$ . Let  $\bar{\Omega} \subset \Omega$  be the discretized image domain as given by

$$\bar{\Omega} = \{(x, y) \in \Omega \mid (x, y) = (x_i, y_j), x_i = i, y_j = j, i = 1, 2, \dots, M \text{ and } j = 1, 2, \dots, N\}.$$

For simplicity, each grid point  $(x_i, y_j) \in \bar{\Omega}$  is denoted by  $(i, j)$ , where the coordinates  $x$  and  $y$  are oriented along columns and rows, respectively. All the variables are defined on these grid points. Let  $\bar{\Omega} \rightarrow \mathcal{V} = \mathbb{R}^{M \times N}$  denotes the 2D grayscale image space with size  $MN$ . So, the first-order forward differences of the grayscale image  $u$  at a grid point  $(i, j)$  along  $x$  and  $y$  directions are respectively

$$\partial_x^+(u)_{i,j} = \begin{cases} (u)_{i,j+1} - (u)_{i,j} & \text{if } 1 \leq i \leq M, 1 \leq j < N, \\ (u)_{i,1} - (u)_{i,j} & \text{if } 1 \leq i \leq M, j = N, \end{cases} \quad (2.49)$$

and

$$\partial_y^+(u)_{i,j} = \begin{cases} (u)_{i+1,j} - (u)_{i,j} & \text{if } 1 < i \leq M, 1 \leq j \leq N, \\ (u)_{1,j} - (u)_{i,j} & \text{if } i = M, 1 \leq j \leq N. \end{cases} \quad (2.50)$$

The first-order backward differences are respectively

$$\partial_x^-(u)_{i,j} = \begin{cases} (u)_{i,j} - (u)_{i,j-1} & \text{if } 1 \leq i \leq M, 1 < j \leq N, \\ (u)_{i,j} - (u)_{i,N} & \text{if } 1 \leq i \leq M, j = 1, \end{cases} \quad (2.51)$$

and

$$\partial_y^-(u)_{i,j} = \begin{cases} (u)_{i,j} - (u)_{i-1,j} & \text{if } 1 < i \leq M, 1 \leq j \leq N, \\ (u)_{i,j} - (u)_{M,j} & \text{if } i = 1, 1 \leq j \leq N. \end{cases} \quad (2.52)$$

For  $\mathbf{p} = (p_1 p_2) \in \mathcal{V}^2$  and  $u \in \mathcal{V}$ , the discrete version of the first-order divergence operator satisfies

$$\sum_{\substack{1 \leq i \leq M \\ 1 \leq j \leq N}} -\text{div}(\mathbf{p}) \cdot u = \sum_{\substack{1 \leq i \leq M \\ 1 \leq j \leq N}} \mathbf{p} \cdot (\nabla u).$$

Therefore, according to the definition of discrete gradient operator, the discrete divergence is given by

$$\text{div}(\mathbf{p})_{i,j} = \partial_x^-(p_1)_{i,j} + \partial_y^-(p_2)_{i,j}. \quad (2.53)$$

The second-order derivative operators of  $u$  at a grid point  $(i, j)$  are given by

$$\begin{aligned} \partial_x^+ \partial_x^-(u)_{i,j} &= \partial_x^- \partial_x^+(u)_{i,j}, \\ &= \begin{cases} (u)_{i,N} - 2(u)_{i,j} + (u)_{i,j+1} & \text{if } 1 \leq i \leq M, j = 1, \\ (u)_{i,j-1} - 2(u)_{i,j} + (u)_{i,j+1} & \text{if } 1 \leq i \leq M, 1 < j < N, \\ (u)_{i,j-1} - 2(u)_{i,j} + (u)_{i,1} & \text{if } 1 \leq i \leq M, j = N, \end{cases} \end{aligned} \quad (2.54)$$

$$\begin{aligned} \partial_y^+ \partial_y^-(u)_{i,j} &= \partial_y^- \partial_y^+(u)_{i,j} \\ &= \begin{cases} (u)_{M,j} - 2(u)_{i,j} + (u)_{i+1,j} & \text{if } i = 1, 1 \leq j \leq N, \\ (u)_{i-1,j} - 2(u)_{i,j} + (u)_{i+1,j} & \text{if } 1 < i < M, 1 \leq j \leq N, \\ (u)_{i-1,j} - 2(u)_{i,j} + (u)_{1,j} & \text{if } i = M, 1 \leq j \leq N, \end{cases} \end{aligned} \quad (2.55)$$

$$\begin{aligned} \partial_x^+ \partial_y^+(u)_{i,j} &= \partial_y^+ \partial_x^+(u)_{i,j} \\ &= \begin{cases} (u)_{i,j} - (u)_{i+1,j} - (u)_{i,j+1} + (u)_{i+1,j+1} & \text{if } 1 \leq i < M, 1 \leq j < N, \\ (u)_{i,j} - (u)_{1,j} - (u)_{i,j+1} + (u)_{1,j+1} & \text{if } i = M, 1 \leq j < N, \\ (u)_{i,j} - (u)_{i+1,j} - (u)_{i,1} + (u)_{i+1,1} & \text{if } 1 \leq i < M, j = N, \\ (u)_{i,j} - (u)_{1,j} - (u)_{i,1} + (u)_{1,1} & \text{if } i = M, j = N, \end{cases} \end{aligned} \quad (2.56)$$



$$\begin{aligned}
\partial_x^- \partial_y^- (u)_{i,j} &= \partial_y^- \partial_x^- (u)_{i,j} \\
&= \begin{cases} (u)_{i,j} - (u)_{i,N} - (u)_{M,j} + (u)_{M,N} & \text{if } i = 1, j = 1, \\ (u)_{i,j} - (u)_{1,j-1} - (u)_{M,j} + (u)_{M,j-1} & \text{if } i = 1, 1 < j \leq N, \\ (u)_{i,j} - (u)_{i,N} - (u)_{i-1,j} + (u)_{i-1,N} & \text{if } 1 < i \leq M, j = 1, \\ (u)_{i,j} - (u)_{i,j-1} - (u)_{i-1,j} + (u)_{i-1,j-1} & \text{if } 1 < i \leq M, 1 < j \leq N, \end{cases}
\end{aligned} \tag{2.57}$$

$$\partial_x^+ \partial_y^- (u)_{i,j} = \begin{cases} (u)_{i,j+1} - (u)_{i,j} - (u)_{M,j+1} + (u)_{M,j} & \text{if } i = 1, 1 \leq j < N, \\ (u)_{i,1} - (u)_{i,j} - (u)_{M,1} + (u)_{M,j} & \text{if } i = 1, j = N, \\ (u)_{i,j+1} - (u)_{i,j} - (u)_{i-1,j+1} + (u)_{i-1,j} & \text{if } 1 < i \leq M, 1 \leq j < N, \\ (u)_{i,1} - (u)_{i,j} - (u)_{i-1,1} + (u)_{i-1,j} & \text{if } 1 < i \leq M, j = N, \end{cases} \tag{2.58}$$

$$\partial_y^+ \partial_x^- (u)_{i,j} = \begin{cases} (u)_{i+1,j} - (u)_{i,j} - (u)_{i+1,N} + (u)_{i,N} & \text{if } 1 \leq i < M, j = 1, \\ (u)_{1,j} - (u)_{i,j} - (u)_{1,N} + (u)_{i,N} & \text{if } i = M, j = 1, \\ (u)_{i+1,j} - (u)_{i,j} - (u)_{i+1,j-1} + (u)_{i,j-1} & \text{if } 1 \leq i < M, 1 < j \leq N, \\ (u)_{1,j} - (u)_{i,j} - (u)_{1,j-1} + (u)_{i,j-1} & \text{if } i = M, 1 < j \leq N. \end{cases} \tag{2.59}$$

Based on (2.54) and (2.55), the discrete Laplace operator is given by

$$(\Delta u)_{i,j} = \text{div}(\nabla u)_{i,j} = \partial_x^- \partial_x^+ (u)_{i,j} + \partial_y^- \partial_y^+ (u)_{i,j}. \tag{2.60}$$

For  $\mathbf{q} = \begin{pmatrix} q_1 & q_2 \\ q_3 & q_4 \end{pmatrix} \in \mathcal{V}^{2 \times 2}$  and  $u \in \mathcal{V}$ , we have

$$\sum_{\substack{1 \leq i \leq M \\ 1 \leq j \leq N}} \text{div}^2(\mathbf{q}) \cdot u = \sum_{\substack{1 \leq i \leq M \\ 1 \leq j \leq N}} \mathbf{q} \cdot (\nabla^2 u).$$

Therefore, the discrete version of the second-order divergence operator is given by

$$\text{div}^2(\mathbf{q})_{i,j} = \partial_x^+ \partial_x^- (q_1)_{i,j} + \partial_y^- \partial_x^- (q_2)_{i,j} + \partial_x^- \partial_y^- (q_3)_{i,j} + \partial_y^+ \partial_y^- (q_4)_{i,j}. \tag{2.61}$$

For the discrete fourth-order derivative operators of  $u$  at grid point  $(i, j)$ , we

have

$$\begin{aligned}\partial_x^- \partial_x^+ \partial_x^- \partial_x^+(u)_{i,j} &= \partial_x^+ \partial_x^- \partial_x^- \partial_x^+(u)_{i,j} \\ &= 6(u)_{i,j} + (u)_{i,j+2} + (u)_{i,j-2} - 4(u)_{i,j+1} - 4(u)_{i,j-1},\end{aligned}\quad (2.62)$$

$$\begin{aligned}\partial_y^- \partial_y^+ \partial_y^- \partial_y^+(u)_{i,j} &= \partial_y^+ \partial_y^- \partial_y^- \partial_y^+(u)_{i,j} \\ &= 6(u)_{i,j} + (u)_{i+2,j} + (u)_{i-2,j} - 4(u)_{i+1,j} - 4(u)_{i-1,j},\end{aligned}\quad (2.63)$$

$$\begin{aligned}\partial_x^- \partial_x^+ \partial_y^- \partial_y^+(u)_{i,j} &= \partial_y^- \partial_y^+ \partial_x^- \partial_x^+(u)_{i,j} = \partial_x^- \partial_x^+ \partial_y^- \partial_y^+(u)_{i,j} = \partial_y^- \partial_x^- \partial_y^+ \partial_x^+(u)_{i,j} \\ &= 4(u)_{i,j} + (u)_{i+1,j+1} + (u)_{i-1,j+1} + (u)_{i+1,j-1} + (u)_{i-1,j-1} \\ &\quad - 2((u)_{i,j+1} + (u)_{i,j-1} + (u)_{i+1,j} + (u)_{i-1,j}).\end{aligned}\quad (2.64)$$

Based on (2.62)-(2.64), we obtain the following two discrete fourth-order differential operators:

$$\begin{aligned}div^2 (\nabla^2 u)_{i,j} &= \partial_x^+ \partial_x^- \partial_x^- \partial_x^+(u)_{i,j} + \partial_y^- \partial_x^- \partial_y^+ \partial_x^+(u)_{i,j} \\ &\quad + \partial_x^- \partial_y^- \partial_x^+ \partial_y^+(u)_{i,j} + \partial_y^+ \partial_y^- \partial_y^- \partial_y^+(u)_{i,j},\end{aligned}\quad (2.65)$$

$$\begin{aligned}\Delta^2(u)_{i,j} &= \Delta(\Delta u)_{i,j}, \\ &= \partial_x^- \partial_x^+ \partial_x^- \partial_x^+(u)_{i,j} + \partial_x^- \partial_x^+ \partial_y^- \partial_y^+(u)_{i,j} \\ &\quad + \partial_y^- \partial_y^+ \partial_x^- \partial_x^+(u)_{i,j} + \partial_y^- \partial_y^+ \partial_y^- \partial_y^+(u)_{i,j}.\end{aligned}\quad (2.66)$$

We note first that  $div^2 (\nabla^2 u)_{i,j} = \Delta^2(u)_{i,j}$ . We also note that the periodic boundary conditions are applied with the above finite difference approximations.

## 2.6 Iterative Solutions to System of Nonlinear Equations

In this section, we introduce the iterative methods to solve the system of nonlinear equations. For more details, we refer to [24, 67] and references therein.

### 2.6.1 Fixed-Point Iteration Method

We now consider systems of nonlinear equations. Let  $\mathbf{F}$  be a given vector function from a domain in  $\mathbb{R}^n$  to a range also in  $\mathbb{R}^m$ , i.e.,  $\mathbf{F} : \mathbb{R}^n \rightarrow \mathbb{R}^m$ . We are now

looking for a solution vector  $\mathbf{x} = (x_1, x_2, \dots, x_n)^T$  that satisfies a set of  $n$  nonlinear equations

$$\mathbf{F}(\mathbf{x}) = \mathbf{0}, \quad (2.67)$$

where

$$\mathbf{F}(\mathbf{x}) = \begin{pmatrix} f_1(x_1, x_2, \dots, x_n) \\ f_2(x_1, x_2, \dots, x_n) \\ \dots \\ f_m(x_1, x_2, \dots, x_n) \end{pmatrix} \quad (2.68)$$

and  $\mathbf{0}$  here is understood to be the zero vector in  $\mathbb{R}^m$ . In order to apply a fixed-point iteration method, we first need to transform the system

$$\mathbf{F}(\mathbf{x}) = \mathbf{0}$$

into the system

$$\mathbf{x} = \mathbf{G}(\mathbf{x}).$$

For the function  $\mathbf{x} = \mathbf{G}(\mathbf{x})$ , the fixed-point iteration method is given by

$$\mathbf{x}^{(k+1)} = \mathbf{G}(\mathbf{x}^k),$$

where  $k \in \mathbb{N}_0$ .

## 2.6.2 Explicit Time Marching Method

To solve the variational models for noise reduction, the main aim is to solve the associated EL equation, which generally turns out to be a nonlinear PDE as given by

$$f(u, z) + \mathcal{N}(u) = 0 \quad (2.69)$$

subject to the appropriate boundary conditions.

In order to solve the nonlinear PDE in (2.69), the time marching method performs by introducing the artificial time variable  $t$  and then determining the steady state solution of the linear time-dependent PDE:

$$\partial_t u(t) = f(u(t), z) + \alpha \mathcal{N}(u(t)),$$

where  $u(t) = u(x, t)$ , typically  $u(0) = z$ .

In the case  $f$  and  $\mathcal{N}$  are nonlinear, the explicit time marching method for (2.6.2) can be given by

$$\frac{u(t^{(k+1)}) - u(t^{(k)})}{\tau} = f(u(t^{(k)}), z) + \alpha \mathcal{N}(u(t^{(k)}))$$

where  $k \in \mathbb{N}_0$  and  $\tau > 0$  denotes the time length used to discretize  $\partial_t u(t)$  see [3, 6, 49, 50, 54].

### 2.6.3 Alternating Direction Method of Multipliers

Here, we review the alternating direction method of multipliers (ADMM) which is a variant of the augmented Lagrangian method that partially updates the dual variables. Consider the following constrained problem:

$$\begin{aligned} \min f(x) + g(z) \\ \text{s.t. } Ax + Bz = c \end{aligned} \quad (2.70)$$

with  $x \in \mathbb{R}^{n \times 1}$ ,  $z \in \mathbb{R}^{m \times 1}$ ,  $A \in \mathbb{R}^{p \times n}$ ,  $B \in \mathbb{R}^{p \times m}$  and  $c \in \mathbb{R}^{p \times 1}$ . Its corresponding augmented Lagrangian function is defined by the following formulation:

$$\mathcal{L}_A(x, z, \lambda, \sigma) = f(x) + g(z) + \lambda^T (Ax + Bz - c) + \frac{1}{2\sigma} \|Ax + Bz - c\|^2, \quad (2.71)$$

where  $\lambda$  is the Lagrangian multiplier and  $\sigma > 0$  is the penalty parameter. Then ADMM consists of the following iterations

$$\begin{aligned} x^{k+1} &:= \operatorname{argmin} \mathcal{L}_A(x, z^k, \lambda^k, \sigma), \\ z^{k+1} &:= \operatorname{argmin} \mathcal{L}_A(x^{k+1}, z, \lambda^k, \sigma), \\ \lambda^{k+1} &:= \lambda^k + \frac{1}{\sigma} (Ax^{k+1} + Bz^{k+1} - c). \end{aligned} \quad (2.72)$$

ADMM can be viewed as a Gauss-Seidel pass over  $x$  and  $z$  instead of updating  $x$  and  $z$  simultaneously. By considering the structures of  $f$  and  $g$ , we can design effective solves for subproblem  $x$  and subproblem  $z$  respectively and reduce the computational time significantly. Besides, ADMM can have excellent properties of the convergence under suitable assumptions.

## 2.6.4 Bregman Iteration

Here, we introduce the Bregman iteration, which is one of the most popular methods in image processing and first used by Osher et al. in [26] to solve the ROF model for TV denoising. We consider the following constrained optimization problem:

$$\min_x f(x) \text{ subject to } Ax = b, \quad (2.73)$$

where  $A$  is a linear operator and  $b$  is a vector. We use the quadratic penalty method to convert (2.73) into the following unconstrained optimization problem:

$$\min_x f(x) + \frac{1}{2\sigma} \|Ax - b\|_2^2. \quad (2.74)$$

Then the basic iterative scheme of the Bregman iteration is as follows:

$$x^{k+1} = \operatorname{argmin}_x f(x) + \frac{1}{2\sigma} \|Ax - b^k\|_2^2, \quad (2.75)$$

$$b^{k+1} = b^k + b - Ax^{k+1}. \quad (2.76)$$

Yin et al. [64] point out that the Bregman iteration is equivalent to the augmented Lagrangian method when the constraints are linear.

As we can see, the main idea behind our SB method is to introduce several auxiliary variables for converting the complex operation into an alternating iterative process by simple operations, which are easy to implement and have high computational efficiency. In order to solve the proposed variational model, we apply the split Bregman method to propose a fast ultrasound speckle reduction algorithm.

## Chapter 3

# Review of Variational Models for Noise Reduction

Basically, the US images used in the medical diagnosis suffer from the speckle noise (SN) because of the imaging principle. The SN degrades the quality and visibility of US images, thereby decreasing overall reliability of the images and interfering with the clinical diagnosis. Therefore, SN reduction in US images becomes one of the necessary pre-processing steps in order to provide meaningful and useful information for the medical diagnosis.

In order to improve the image quality and increase the diagnostics potential for clinical US images, a number of SN removal methods have been proposed and studied recently. Roughly speaking, these SN removal methods fall into five categories:

1. spatial domain [30, 38, 42, 46];
2. a transform domain, e.g. wavelet domain [2, 19, 29, 39];
3. non-local filtering [13, 22, 55];
4. anisotropic diffusion methods [18, 66];
5. variational methods [4, 28, 32, 33, 34, 35, 36, 50, 54].

Among these SN removal methods, the variational methods are powerful tools to offer superior image restoration quality. Accordingly, this research focuses on the variational method to deal with the SN in the US images.

### 3.1 Images and Noise

Given a noisy image  $z : \Omega \subset \mathbb{R}^2 \rightarrow V \subset \mathbb{R}$ , where  $\Omega$  is a bounded open subset of  $\mathbb{R}^2$ , the purpose of the noise reduction is to restore the original image  $u : \Omega \subset \mathbb{R}^2 \rightarrow V \subset \mathbb{R}$  from the noisy image  $z$ .

In many image formulation models, the noisy image is the sum of the original image and the additive noise (AN):

$$z = u + \eta, \quad (3.1)$$

where  $\eta$  is assumed to be the zero-mean Gaussian white noise.

In contrast, the image formation model is different from (3.1) for SN. It is assumed that the original image  $u$  is corrupted by some multiplicative speckle noise (MSN)  $\zeta$  as follows:

$$z = u\zeta, \quad (3.2)$$

where  $z > 0$  and  $u > 0$ . As is well known, MSN is commonly found in many real world image processing applications, such as in laser images, microscope images, medical US images and synthetic aperture radar (SAR) images. Unlike traditionally AN model in (3.1), the noisy signals in the recorded images are much more difficult to be removed, mainly not only because of the multiplicative nature between the noise and the original image, which is signal correlated, but also because of the noise distribution, which is generally non-Gaussian with Rayleigh and Gamma being common noise distributions [57].

In clinical US imaging systems, Loupas et al. [42] pointed out that the noise in the displayed US image “on screen” can be modeled as corrupted with the SN of the form

$$z = u + \sqrt{u}\zeta, \quad (3.3)$$

where  $\zeta$  is the zero-mean Gaussian noise with the standard deviation  $\sigma_n^2$ . Due to the additive term in the image formulation model (3.3), we shall name this SN as the *additive speckle noise* (ASN).

## 3.2 Variational Formulation

In the literature, many approaches have been developed to eliminate noise from images. The variational approach is one of the most commonly used techniques for noise reduction.

Generally speaking, the variational method or variational model for noise reduction of the noisy image consists in solving the minimization problem

$$\min_{u \in \mathcal{U}} \{ \mathcal{J}(u) = \gamma \mathcal{D}(u, z) + \mathcal{R}(u) \}, \quad (3.4)$$

where  $\mathcal{D}(u, z)$  is the data fidelity term, which is derived from the assumption on the distribution of the noise in the noisy image in order to penalize the inconsistency between the restored image and the noisy image,  $\mathcal{R}(u)$  is the regularization term, which is used to filter out the noise from the observed noisy image as well as to preserve significant features such as edges and textures of the restored image, and  $\gamma > 0$  is the regularization parameter, which is used to compromise the fidelity term  $\mathcal{D}(u, z)$  and the regularization term  $\mathcal{R}(u)$ . Here the solution  $u$  is searched over a set of admissible functions  $\mathcal{U}$ , which minimizes the objective functional  $\mathcal{J}$ .

## 3.3 Variational Models for Additive Noise Reduction

In order to recover  $u$  from the noisy image  $z$  by using the AN model in (3.1), Rudin, Osher, and Fatemi [49] used the TV regularization

$$\mathcal{R}^{\text{TV}}(u) = \int_{\Omega} |\nabla u| \, d\Omega$$

with the quadratic fidelity term resulting from the AN model (3.1)

$$\mathcal{D}_{\text{AN}}(u, z) = \frac{1}{2} \int_{\Omega} (u - z)^2 \, d\Omega$$

and proposed the total variation (TV) model

$$\min_u \{ \mathcal{J}^{\text{TV}}(u) = \gamma \mathcal{D}_{\text{AN}}(u, z) + \mathcal{R}^{\text{TV}}(u) \}. \quad (3.5)$$

Although TV regularization has some undesired effects. In particular, it transforms smooth signals or signals that are not necessarily piecewise constant into



piecewise constants. This phenomenon is known as staircase effect. From a practical point of view, staircase solutions of TV based variational model fail to satisfy the evaluation of visual quality, and they can develop false edges that do not exist in the true image. The main challenge is thus to deal with the staircase effect while preserving image sharpness.

The weakness of TV regularization is known as staircase effect. To eliminate the staircase effect, several higher-order regularizations have been proposed so far in the literature for (3.4) to yield better restoration results. These higher-order regularizations usually involve second-order differential operators in dealing with the staircase effect because piecewise-vanishing second-order derivatives yield piecewise-linear solutions that better fit than those by the TV regularization for smooth intensity changes. To the best of our knowledge, there are three main classes of higher-order regularizations for image restoration problems. The first class combines a second-order regularization with the TV regularization. The second class employs a second-order regularization in a standalone way. The third class uses fractional-order derivative to model the regularization term. Next, we briefly review the higher-order variational models.

You and Kaveh [65] used the TL regularization

$$\mathcal{R}^{\text{TL}}(u) = \int_{\Omega} |\Delta u| d\Omega = \int_{\Omega} \sqrt{|u_{xx}|^2 + |u_{yy}|^2} d\Omega,$$

where  $\Delta u$  denotes the Laplacian operator and introduced the total Laplace (TL) model

$$\min_u \{ \mathcal{J}_{\text{AN}}^{\text{TL}}(u) = \gamma \mathcal{D}_{\text{AN}}(u, z) + \mathcal{R}^{\text{TL}}(u) \}. \quad (3.6)$$

Scherzer [51], Lysaker et al. [45], Hinterberger and Scherzer [31], Bergounioux and Piffet [5] and Lai et al. [41] used the BH regularization

$$\mathcal{R}^{\text{BH}}(u) = \int_{\Omega} |\nabla^2 u| d\Omega,$$

where

$$\nabla^2 u = \begin{pmatrix} u_{xx} & u_{yx} \\ u_{xy} & u_{yy} \end{pmatrix}$$

is the Hessian matrix of  $u$  and  $|\nabla^2 u| = \sqrt{u_{xx}^2 + u_{yx}^2 + u_{xy}^2 + u_{yy}^2}$  and considered the

bounded Hessian (BH) model

$$\min_u \{ \mathcal{J}_{\text{AN}}^{\text{BH}}(u) = \gamma \mathcal{D}_{\text{AN}}(u, z) + \mathcal{R}^{\text{BH}}(u) \}. \quad (3.7)$$

Chan et al. [16] decomposed the noisy image  $z$  into three parts, i.e.  $z = u_1 + u_2 + \eta$  and proposed the fidelity term  $\bar{\mathcal{D}}_{\text{AN}}(u_1, u_2, z) = \frac{1}{2} \int_{\Omega} (z - u_1 - u_2)^2 d\Omega$ . They used the CEP- $L^2$  regularization

$$\mathcal{R}^{\text{CEP-}L^2}(u_1, u_2) = \gamma_1 \mathcal{R}^{\text{TV}}(u_1) + \gamma_2 \mathcal{R}^{\text{TL}}(u_2)$$

where  $\gamma_1 > 0$  and  $\gamma_2 > 0$  are the weighting parameters and proposed the CEP- $L^2$  model

$$\min_{u_1, u_2} \{ \mathcal{J}^{\text{CEP-}L^2}(u_1, u_2) = \gamma \bar{\mathcal{D}}_{\text{AN}}(u_1, u_2, z) + \mathcal{R}^{\text{CEP-}L^2}(u_1, u_2) \}. \quad (3.8)$$

Zheng et al. [69], Wang et al. [61] and Chan et al. [15] used the TVL regularization

$$\mathcal{R}^{\text{TVL}}(u) = \gamma_1 \mathcal{R}^{\text{TV}}(u) + \gamma_2 \mathcal{R}^{\text{TL}}(u)$$

and proposed the TVL model

$$\min_u \{ \mathcal{J}_{\text{AN}}^{\text{TVL}}(u) = \gamma \mathcal{D}_{\text{AN}}(u, z) + \mathcal{R}^{\text{TVL}}(u) \}. \quad (3.9)$$

Papafitsoros and Schönlieb [48] used the TVBH regularization

$$\mathcal{R}^{\text{TVBH}}(u) = \gamma_1 \mathcal{R}^{\text{TV}}(u) + \gamma_2 \mathcal{R}^{\text{BH}}(u)$$

and proposed the TVBH model

$$\min_u \{ \mathcal{J}_{\text{AN}}^{\text{TVBH}}(u) = \gamma \mathcal{D}_{\text{AN}}(u, z) + \mathcal{R}^{\text{TVBH}}(u) \}. \quad (3.10)$$

Chambolle and Lions [14] used the INFCON regularization

$$\mathcal{R}^{\text{INFCON}}(u_1, u_2) = \gamma_1 \mathcal{R}^{\text{TV}}(u_1) + \gamma_2 \mathcal{R}^{\text{BH}}(u_2)$$

and introduced the INFCON model

$$\min_{u_1, u_2} \{ \mathcal{J}_{\text{AN}}^{\text{INFCON}}(u_1, u_2) = \gamma \bar{\mathcal{D}}_{\text{AN}}(u_1, u_2, z) + \mathcal{R}^{\text{INFCON}}(u_1, u_2) \}. \quad (3.11)$$

Bredies et al. [8] used the TGV regularization

$$\mathcal{R}^{\text{TGV}}(u, \tilde{\mathbf{p}}) = \gamma_1 \int_{\Omega} |\nabla u - \tilde{\mathbf{p}}| d\Omega + \gamma_2 \int_{\Omega} |\epsilon(\tilde{\mathbf{p}})| d\Omega,$$

where  $\epsilon(\tilde{\mathbf{p}})$  is the symmetrized derivatives defined as

$$\epsilon(\tilde{\mathbf{p}}) = \begin{pmatrix} \tilde{p}_{1x} & \frac{\tilde{p}_{1y} + \tilde{p}_{2x}}{2} \\ \frac{\tilde{p}_{1y} + \tilde{p}_{2x}}{2} & \tilde{p}_{2y} \end{pmatrix}$$

and introduced the total generalized variation (TGV) model

$$\min_{u, \tilde{\mathbf{p}}} \{ \mathcal{J}_{\text{AN}}^{\text{TGV}}(u, \tilde{\mathbf{p}}) = \gamma \mathcal{D}_{\text{AN}}(u, z) + \mathcal{R}^{\text{TGV}}(u, \tilde{\mathbf{p}}) \}. \quad (3.12)$$

Zhu and Chan [70] used the MC regularization

$$\mathcal{R}^{\text{MC}}(u) = \int_{\Omega} |\kappa_{\text{M}}(u)| \, d\Omega$$

where

$$\kappa_{\text{M}}(u) = \nabla \cdot \left( \frac{\nabla u}{\sqrt{1 + |\nabla u|^2}} \right)$$

is the mean curvature of image surface  $\phi(x, y, z) = u(x, y) - z = 0$  and proposed the mean curvature (MC) model

$$\min_u \{ \mathcal{J}_{\text{AN}}^{\text{MC}}(u) = \gamma \mathcal{D}_{\text{AN}}(u, z) + \mathcal{R}^{\text{MC}}(u) \}. \quad (3.13)$$

This model tries to fit the given noisy image surface  $(x, y, z(x, y))$  with a surface  $(x, y, u(x, y))$  that bears small magnitude of mean curvature. As demonstrated in [70], the MC model is able to sweep noise while keeping object edges, and it also ameliorates the staircase effect. More importantly, the MC model is also capable of preserving image contrasts as well as geometry of object shapes, especially object corners.

Brito-Loeza and Chen [11] used the GC regularization

$$\mathcal{R}^{\text{GC}}(u) = \int_{\Omega} |\kappa_{\text{G}}(u)| \, d\Omega$$

where

$$\kappa_{\text{G}}(u) = \frac{u_{xx}u_{yy} - u_{xy}u_{yx}}{(1 + |\nabla u|^2)^2}$$

is the Gaussian curvature of image surface  $\phi(x, y, z) = u(x, y) - z = 0$  and proposed the Gaussian curvature (GC) model

$$\min_u \{ \mathcal{J}_{\text{AN}}^{\text{GC}}(u) = \gamma \mathcal{D}_{\text{AN}}(u, z) + \mathcal{R}^{\text{GC}}(u) \}. \quad (3.14)$$

This model is able to preserve image contrast, edges, and corners such as the MC model does.

Zhang and Chen [68] used the  $\text{TV}^\alpha$  regularization

$$\mathcal{R}^{\text{TV}^\alpha}(u) = \sup_{\phi \in K} \int_{\Omega} (-u \operatorname{div}^\alpha \phi) d\Omega,$$

where  $\operatorname{div}^\alpha \phi = \sum_{i=1}^d \frac{\partial^\alpha \phi_i}{\partial x_i^\alpha}$ ,  $\frac{\partial^\alpha \phi_i}{\partial x_i^\alpha}$  is the  $\alpha$ -order derivative of  $\phi_i$  along the  $x_i$  direction,

$$K = \{\phi \in l_0^l(\Omega, \mathbb{R}^d) \mid |\phi(x)| \leq 1 \text{ for all } x \in \Omega\}$$

is the space of special test functions, and  $l_0^l(\Omega, \mathbb{R}^d)$  is the  $l$ -compactly supported continuous-integrable function space, and proposed the total  $\alpha$ -order variation model

$$\min_u \{ \mathcal{J}_{\text{AN}}^{\text{TV}^\alpha}(u) = \gamma \mathcal{D}_{\text{AN}}(u, z) + \mathcal{R}^{\text{TV}^\alpha}(u) \}. \quad (3.15)$$

Chankan et al. [17] proposed firstly a new high-order regularization based on the sum of squared principal curvatures of the image surface

$$\mathcal{R}^{\text{Cv}}(u) = \frac{1}{2} \int_{\Omega} (k_M^2(u) - 2k_G(u)) d\Omega$$

and proposed a new high-order variation model

$$\min_u \{ \mathcal{J}_{\text{AN}}^{\text{Cv}}(u) = \mathcal{D}_{\text{AN}}(u, z) + \gamma \mathcal{R}^{\text{Cv}}(u) \}. \quad (3.16)$$

From the variational models for additive noise reduction, we can see that the higher-order regularizations are superior than the TV regularization in order to reduce staircase effects and achieve good trade-off between noise removal and edge preservation. Some performance comparison can be seen in [11, 43, 68].

### 3.4 Variational Models for Speckle Noise Reduction

In the literature, the total variation (TV) regularization  $\mathcal{R}^{\text{TV}}(u) = \int_{\Omega} |\nabla u| d\Omega$  is commonly used as regularization term in several variational models for MSN reduction. The term difference among different variational models only comes from

their data fidelity terms. As far as we know, Rudin, Lions, and Osher [50] proposed firstly the MSN removal model (called RLO model) as follows:

$$\min_{u \in S(\Omega)} \left\{ \mathcal{J}_{\text{MSN}}^{\text{RLO}}(u) = \gamma_1 \int_{\Omega} \frac{z}{u} d\Omega + \gamma_2 \int_{\Omega} \left( \frac{z}{u} - 1 \right)^2 d\Omega + \int_{\Omega} |\nabla u| d\Omega \right\}, \quad (3.17)$$

where the first two terms are the data fidelity terms.  $\gamma_1$  and  $\gamma_2$  are the weighting parameters. Here  $S(\Omega) = \{u \in BV(\Omega), u > 0\}$  and  $BV(\Omega)$  represent the space of functions in  $L^1(\Omega)$  such that the bounded variations

$$\int_{\Omega} |Du| = \sup \left\{ \int_{\Omega} u \operatorname{div}(\phi) d\Omega \mid \phi \in C_0^{\infty}(\Omega, \mathbb{R}^2), \|\phi\|_{L^{\infty}(\Omega, \mathbb{R}^N)} \leq 1 \right\}$$

is finite, i.e.  $BV(\Omega) = \{u \in L^1(\Omega), \int_{\Omega} |Du| < \infty\}$ . This model is non-convex and particularly effective for Gaussian multiplicative noise removal.

Under the assumption that the multiplicative noise  $\zeta$  follows the Gamma distribution with mean equal to 1. Aubert and Aujol used the maximum a posteriori (MAP) estimation to derive the variational model in [3] (called the AA model) as follows:

$$\min_{u \in BV(\Omega)} \left\{ \mathcal{J}_{\text{MSN}}^{\text{AA}}(u) = \gamma \int_{\Omega} \left( \log u + \frac{z}{u} \right) d\Omega + \int_{\Omega} |\nabla u| d\Omega \right\}. \quad (3.18)$$

Unfortunately, the AA model is also non-convex due to the data fidelity term. It is therefore difficult to find a global solution and the computed solutions rely on the initial estimation. Moreover, some fast algorithms for convex optimization cannot be used. However, they still proved the existence of the minimizer, gave a sufficient condition ensuring uniqueness and showed that a comparison principle holds. They further gave some numerical tests illustrating the capability of their model. Their results indicate that the AA model outperforms the RLO model for Gamma distribution and are comparable to the results of RLO for Gaussian distribution.

In order to resolve the non-convexity of AA model, Shi and Osher [53] used logarithmic transformation  $\bar{u} = \log(u)$  and proposed the transformed variational model (referred to as SO model):

$$\min_{\bar{u} \in BV(\Omega)} \left\{ \mathcal{J}_{\text{MSN}}^{\text{SO}}(\bar{u}) = \gamma \int_{\Omega} \left( aze^{-\bar{u}} + \frac{b}{2} z^2 e^{-2\bar{u}} + (a+b)\bar{u} \right) d\Omega + \int_{\Omega} |\nabla \bar{u}| d\Omega \right\}, \quad (3.19)$$

where  $a, b$  are nonnegative constants and  $u = e^{\bar{u}}$ . It is remarkable that the SO model is convex in the logarithm domain, but are not convex in the original image

domain. Using the relaxed inverse scale space (ISS) flow method, the restored images can be obtained although it is expensive to compute the solutions.

To improve the speed of computation, Huang et al. [32] used a different idea by converting the term  $\log u + \frac{z}{u}$  in the data fidelity term of AA model into  $u + ze^{-u}$  under the exponential transformation  $u \rightarrow e^u$  to derive the convex model (called HNw model) as follows:

$$\min_{u, w \in BV(\Omega)} \left\{ \mathcal{J}_{\text{MSN}}^{\text{HNW}}(u) = \int_{\Omega} (u + ze^{-u}) d\Omega + \gamma_1 \int_{\Omega} |u - w|^2 d\Omega + \gamma_2 \int_{\Omega} |\nabla w| d\Omega \right\}, \quad (3.20)$$

where  $\gamma_1, \gamma_2$  are two weighting parameters. Jin and Yang [35] used the AA and HNw models to propose the convex model (called JY model) as follows:

$$\min_{u \in BV(\Omega)} \left\{ \mathcal{J}_{\text{MSN}}^{\text{JY}}(u) = \gamma \int_{\Omega} (u + ze^{-u}) d\Omega + \int_{\Omega} |\nabla u| d\Omega \right\}. \quad (3.21)$$

Their experiments on the test images corrupted by some MSN with Gaussian and Gamma noise show that the JY model delivers better restoration results than the AA model. Chunchob et al. [20] introduced the convex model (called CCB model) to restore the noisy images corrupted by the combination of the AN and MSN as follows:

$$\min_{u \in BV(\Omega)} \left\{ \mathcal{J}_{\text{AN-MSN}}^{\text{CCB}}(u) = \frac{\gamma_1}{2} \int_{\Omega} (u - z)^2 d\Omega + \gamma_2 \int_{\Omega} (u + ze^{-u}) d\Omega + \int_{\Omega} |\nabla u| d\Omega \right\}, \quad (3.22)$$

where  $\gamma_1, \gamma_2$  are two weighting parameters. Their results show that the CCB model performs a clear improvement over some existing MSN reduction methods.

Several variational models for ASN reduction in US images by minimization of TV regularization have been proposed in [21, 34, 36, 40]. As far as we know, Krissian et al. [40] introduced firstly the ASN removal model (KKWV model):

$$\min_{u \in S(\Omega)} \left\{ \mathcal{J}_{\text{ASN}}^{\text{KKWV}}(u) = \gamma \int_{\Omega} \frac{(u - z)^2}{u} d\Omega + \int_{\Omega} |\nabla u| d\Omega \right\}. \quad (3.23)$$

As can be seen, the KKWV is convex. The authors in [36] proved the existence and uniqueness of the minimizer for the variational problem (3.23). Huang and Yang [34] used the generalized Kullback–Leibler (KL) distance with (3.3) and proposed the convex model (HY model):

$$\min_{\bar{u} \in BV(\Omega)} \left\{ \mathcal{J}_{\text{ASN}}^{\text{HY}}(\bar{u}) = \gamma \int_{\Omega} (ze^{-\bar{u}/2} \log \frac{z}{e^{\bar{u}}} - ze^{-\bar{u}/2} + e^{\bar{u}/2}) d\Omega + \int_{\Omega} |\nabla \bar{u}| d\Omega \right\}. \quad (3.24)$$

To fast solve the HY model, the authors proposed to incorporate splitting method and Bregman iterative method. Their experimental results indicate that their proposed algorithm is fast and effective to remove ASN in the real US images. Recently,

Chumchob and Prakit [21] used the Weberized total variation (WTV) regularization

$$\mathcal{R}^{\text{WTV}}(u) = \int_{\Omega} \frac{|\nabla u|}{u} d\Omega \quad (3.25)$$

and proposed the convex variational model (improved KKWV model):

$$\min_{\bar{u} \in \bar{S}(\Omega)} \left\{ \mathcal{J}_{\text{ASN}}^{\text{HY}}(u) = \int_{\Omega} \frac{(u - z)^2}{u} d\Omega + \gamma_1 \int_{\Omega} |\nabla u| d\Omega + \gamma_2 \int_{\Omega} \frac{|\nabla u|}{u} d\Omega \right\},$$

for removing ASN on US images, where

$$\bar{S}(\Omega) = \left\{ u \in BV(\Omega), u > 0, \int_{\Omega} \frac{|Du|}{u} < \infty \right\}. \quad (3.26)$$

Their numerical tests show that the improved KKWV model can provide significant improvement over the KKWV and HY models.

From a practical point of view, a fundamental assumption concerning only pure MSN or ASN as modeled and given respectively by (3.2) or (3.3) is inadequate for SN reduction in US images. The reason is that the complex image formation process is considered.

## 3.5 Numerical Solution Schemes

To study the efficient numerical solutions of the existing variational models for SN reduction such as the JY, KKWV and improved KKWV models, we review three numerical algorithms based on the SB framework.

### 3.5.1 Split Bregman Algorithm for the JY model

First, we start with introducing an auxiliary vector variable  $\mathbf{w} = (w_1 \ w_2)$ , a Bregman iterative parameter  $\mathbf{b} = (b_1 \ b_2)$  and a positive penalty parameter  $\theta$ , to transform the variational problem

$$\min_{u \in BV(\Omega)} \left\{ \mathcal{J}_{\text{MSN}}^{\text{JY}}(u) = \gamma \int_{\Omega} (u + ze^{-u}) d\Omega + \int_{\Omega} |\nabla u| d\Omega \right\}$$

into the following form

$$\min_{u, \mathbf{w}} \left\{ \bar{\mathcal{J}}_{\text{MSN}}^{\text{JY}}(u, \mathbf{w}; \mathbf{b}) = \gamma \int_{\Omega} (u + ze^{-u}) d\Omega + \int_{\Omega} |\mathbf{w}| d\Omega + \frac{\theta}{2} \int_{\Omega} (\mathbf{w} - \nabla u - \mathbf{b})^2 d\Omega \right\}. \quad (3.27)$$

Clearly, both variables  $u$  and  $\mathbf{w}$  are very difficult to solve simultaneously. We then separate the minimization problem in (3.27) into two subproblems:

$$u^{(m+1)} = \arg \min_{u>0} \left\{ \gamma \int_{\Omega} (u + ze^{-u}) d\Omega + \frac{\theta}{2} \int_{\Omega} (\mathbf{w}^{(m)} - \nabla u - \mathbf{b}^{(m)})^2 d\Omega \right\}, \quad (3.28)$$

$$\mathbf{w}^{(m+1)} = \arg \min_{\mathbf{w}} \left\{ \int_{\Omega} |\mathbf{w}| d\Omega + \frac{\theta}{2} \int_{\Omega} (\mathbf{w} - \nabla u^{(m+1)} - \mathbf{b}^{(m)})^2 d\Omega \right\}, \quad (3.29)$$

and use an alternating minimization procedure as proposed in Algorithm 1 to approximate the solution. Here the Bregman iterative parameter is update by

$$\mathbf{b}^{(m+1)} = \mathbf{b}^{(m)} + \nabla u^{(m+1)} - \mathbf{w}^{(m+1)}. \quad (3.30)$$

This process is repeated until one of the following stopping rules is satisfied:

$$\frac{\|u^{(m+1)} - u^{(m)}\|^2}{\|u^{(m)}\|^2} < \epsilon_1^{\text{SB}}, \quad (3.31)$$

$$m \geq \epsilon_2^{\text{SB}}, \quad (3.32)$$

where  $\epsilon_1^{\text{SB}}$  denotes the predefined small positive number and  $\epsilon_2^{\text{SB}}$  denotes the maximum iteration of the SB method. Here  $m$  represents the index of the current iteration. The two subproblems can be solved as follows:

**$u$ -subproblem.** Fixing variables  $(\mathbf{w}; \mathbf{b})$  in (3.28) yields the EL equation associated with  $u$  as follows:

$$\Delta u = \bar{G}(u) \quad (3.33)$$

where  $\bar{G}(u) = \nabla \cdot (\mathbf{w} - \mathbf{b}) + \frac{\gamma}{\theta} (1 - ze^{-u})$ . To solve the nonlinear partial differential equation in (3.33), we firstly apply the simple linearized iterations by the following

$$\gamma_1 u^{[\nu+1]} - \Delta u^{[\nu+1]} = G(u^{[\nu]}) \quad (3.34)$$

where  $G(u^{[\nu]}) = \bar{G}(u^{[\nu]}) + \gamma_1 u^{[\nu]}$  and  $\gamma_1 > 0$  is the FP parameter used to stabilize numerical computation. Secondly, we assume that  $\Omega = [1, M] \times [1, N]$  and  $\bar{\Omega} \subset \Omega$  is the discretized image domain where

$$\bar{\Omega} = \{(x, y) = (x_i, y_j) \in \Omega, x_i = i, y_j = j, 1 \leq i \leq M \text{ and } 1 \leq j \leq N\}.$$



Next, we discretize the linearized PDE (3.34) using the standard finite difference method subject to periodic boundary conditions. Therefore, the discrete Fourier transform (DFT) method can be directly applied as follows:

$$\mathcal{F}\{\gamma_1(u^{[\nu+1]})_{i,j} - (\Delta u^{[\nu+1]})_{i,j}\} = \mathcal{F}\{G(u^{[\nu]})_{i,j}\} \quad (3.35)$$

where  $\mathcal{F}$  denoted the DFT operator. For the discrete frequencies  $r \in [0, M)$  and  $s \in [0, N)$ , we have

$$\zeta \mathcal{F}\{(u^{[\nu+1]})_{i,j}\} = \mathcal{F}\{(G(u^{[\nu]})_{i,j}\} \quad (3.36)$$

where  $\zeta = \gamma_1 - 2(\cos(\frac{2\pi s}{N}) + \cos(\frac{2\pi r}{M}) - 2)$ ,  $i \in [1, M]$  and  $j \in [1, N]$  are the indexes in the discrete time domain. For each outer step  $\nu$ , we finally have a closed-form solution of  $u^{[\nu+1]}$  at grid point  $(i, j)$

$$(u^{[\nu+1]})_{i,j} = \text{Re}(\mathcal{F}^{-1}(\frac{\mathcal{F}((G(u^{[\nu]})_{i,j}))}{\zeta})), \quad (3.37)$$

where  $\mathcal{F}^{-1}$  denotes the inverse DFT operator.  $\text{Re}$  is the real part of a complex number. ‘—’ represents for point-wise division of matrices.

**w-subproblem.** Fixing variables  $(u; \mathbf{b})$  in (3.29) yields the EL equation associated with  $\mathbf{w}$  as follows:

$$\frac{\mathbf{w}}{|\mathbf{w}|} + \theta(\mathbf{w} - \nabla u - \mathbf{b}) = 0.$$

The solution can be determined using the closed-form formula [44]

$$(\mathbf{w})_{i,j} = \max(|\nabla(u)_{i,j} + (\mathbf{b})_{i,j}| - \frac{1}{\theta}, 0) \frac{\nabla(u)_{i,j} + (\mathbf{b})_{i,j}}{|\nabla(u)_{i,j} + (\mathbf{b})_{i,j}|}, \quad (3.38)$$

with the convention  $0/0 = 0$ .

### Algorithm 1 : Split Bregman Algorithm for the JY Model

Denote by

- $u$  the restored image
- $z$  the noisy image
- $\mathbf{w}$  the auxiliary spitting vector variable
- $\mathbf{b}$  the Bregman iterative parameter
- $\gamma$  the weighting parameter
- $\gamma_1$  the FP parameter
- $\theta$  the penalty parameter

$$[u] \leftarrow \text{SB}(u, z, \mathbf{w}, \mathbf{b}, \gamma, \gamma_1, \theta)$$

---

Step 1. Initialization, set  $u = z, m = 0$  and  $\mathbf{w}^{(m)} = \mathbf{b}^{(m)} = \mathbf{0}$

and choose  $\gamma, \gamma_1, \theta > 0$ ;

Step 2. Compute  $u^{(m+1)}$  according to (3.37) for fixed  $(\mathbf{w}^{(m)}; \mathbf{b}^{(m)})$ ;

Step 3. Compute  $\mathbf{w}^{(m+1)}$  according to (3.38) for fixed  $(u^{(m+1)}; \mathbf{b}^{(m)})$ ;

Step 4. Update  $\mathbf{b}^{(m+1)}$  according to (3.30);

Step 5. If a stopping criterion is satisfied, stop; else  $m \leftarrow m + 1$ , repeat 2.

---

### 3.5.2 Split Bregman Algorithm for the KKWV model

In order to solve the KKWV model, we introduce an auxiliary vector variable  $\mathbf{w} = (w_1 \ w_2)$ , a Bregman iterative parameter  $\mathbf{b} = (b_1 \ b_2)$  and a positive penalty parameter  $\theta$ , to transform the variational problem

$$\min_{u \in S(\Omega)} \left\{ \mathcal{J}_{\text{ASN}}^{\text{KKWV}}(u) = \gamma \int_{\Omega} \frac{(u-z)^2}{u} d\Omega + \int_{\Omega} |\nabla u| d\Omega \right\}.$$

into the following form

$$\min_{u, \mathbf{w}} \left\{ \bar{\mathcal{J}}_{\text{ASN}}^{\text{KKWV}}(u, \mathbf{w}; \mathbf{b}) = \gamma \int_{\Omega} \frac{(u-z)^2}{u} d\Omega + \int_{\Omega} |\mathbf{w}| d\Omega + \frac{\theta}{2} \int_{\Omega} (\mathbf{w} - \nabla u - \mathbf{b})^2 d\Omega \right\}. \quad (3.39)$$

Applying the alternating optimization technique with (3.39), we then solve two subproblems for  $u$  and  $w$  and update  $b$  as follows :

$$u^{(m+1)} = \arg \min_{u > 0} \left\{ \gamma \int_{\Omega} \frac{(u-z)^2}{u} d\Omega + \frac{\theta}{2} \int_{\Omega} (\mathbf{w}^{(m)} - \nabla u - \mathbf{b}^{(m)})^2 d\Omega \right\}, \quad (3.40)$$

$$\mathbf{w}^{(m+1)} = \arg \min_{\mathbf{w}} \left\{ \int_{\Omega} |\mathbf{w}| d\Omega + \frac{\theta}{2} \int_{\Omega} (\mathbf{w} - \nabla u^{(m+1)} - \mathbf{b}^{(m)})^2 d\Omega \right\}, \quad (3.41)$$

$$\mathbf{b}^{(m+1)} = \mathbf{b}^{(m)} + \nabla u^{(m+1)} - \mathbf{w}^{(m+1)}. \quad (3.42)$$

This process is repeated until one of the stopping rules given in (3.31) and (3.32) is satisfied. The two subproblems can be solved as follows:

**$u$ -subproblem.** Fixing variables  $(\mathbf{w}; \mathbf{b})$  in (3.40) yields the EL equation associated with  $u$  as follows:

$$\Delta u = \bar{G}(u) \quad (3.43)$$

where  $\bar{G}(u) = \nabla \cdot (\mathbf{w} - \mathbf{b}) + \frac{\gamma}{\theta} \left(1 - \frac{z^2}{u^2}\right)$ . By using the similar procedure in section 3.5.1, the nonlinear PDE (3.43) can be solve as follows. We apply the simple linearized iterations by the following

$$\gamma_1 u^{[\nu+1]} - \Delta u^{[\nu+1]} = G(u^{[\nu]}) \quad (3.44)$$

where  $G(u^{[\nu]}) = \bar{G}(u^{[\nu]}) + \gamma_1 u^{[\nu]}$  and  $\gamma_1 > 0$  is the FP parameter used to stabilize numerical computation. Secondly, we apply the discrete differential operators as given in section 3.5.1 and then apply the DFT to the both side leads to

$$\mathcal{F}\{\gamma_1 (u^{[\nu+1]})_{i,j} - (\Delta u^{[\nu+1]})_{i,j}\} = \mathcal{F}\{G(u^{[\nu]})_{i,j}\} \quad (3.45)$$

where  $\mathcal{F}$  denoted the DFT operator. For the discrete frequencies  $r \in [0, M)$  and  $s \in [0, N)$ , we have

$$\zeta \mathcal{F}\{(u^{[\nu+1]})_{i,j}\} = \mathcal{F}\{(G(u^{[\nu]}))_{i,j}\} \quad (3.46)$$

where  $\zeta = \gamma_1 - 2(\cos(\frac{2\pi s}{N}) + \cos(\frac{2\pi r}{M}) - 2)$ ,  $i \in [1, M]$  and  $j \in [1, N]$  are the indexes in the discrete time domain. For each outer step  $\nu$ , we finally have a closed-form solution of  $u^{[\nu+1]}$  at grid point  $(i, j)$

$$(u^{[\nu+1]})_{i,j} = \text{Re}(\mathcal{F}^{-1}(\frac{\mathcal{F}((G(u^{[\nu]}))_{i,j})}{\zeta})), \quad (3.47)$$

where  $\mathcal{F}^{-1}$  denotes the inverse DFT operator.  $\text{Re}$  is the real part of a complex number. ‘—’ represents for point-wise division of matrices.

**w-subproblem.** Fixing variables  $(u; \mathbf{b})$  in (3.41) yields the EL equation associated with  $\mathbf{w}$  as follows:

$$\frac{\mathbf{w}}{|\mathbf{w}|} + \theta(\mathbf{w} - \nabla u - \mathbf{b}) = 0.$$

The solution can be determined using the closed-form formula [44]

$$(\mathbf{w})_{i,j} = \max(|\nabla(u)_{i,j} + (\mathbf{b})_{i,j}| - \frac{1}{\theta}, 0) \frac{\nabla(u)_{i,j} + (\mathbf{b})_{i,j}}{|\nabla(u)_{i,j} + (\mathbf{b})_{i,j}|}, \quad (3.48)$$

with the convention  $0/0 = 0$ .

The SB method for the KKWV model (3.39) can be summarized as shown in Algorithm 2.

## Algorithm 2 : Split Bregman Algorithm for the KKWV Model

Denote by

- $u$  the restored image
- $z$  the noisy image
- $\mathbf{w}$  the auxiliary spitting vector variable
- $\mathbf{b}$  the Bregman iterative parameter
- $\gamma$  the weighting parameter
- $\gamma_1$  the FP parameter
- $\theta$  the penalty parameter

$$[u] \leftarrow \text{SB}(u, z, \mathbf{w}, \mathbf{b}, \gamma, \gamma_1, \theta)$$

---

Step 1. Initialization, set  $u = z, m = 0$  and  $\mathbf{w}^{(m)} = \mathbf{b}^{(m)} = \mathbf{0}$

and choose  $\gamma, \gamma_1, \theta > 0$ ;

Step 2. Compute  $u^{(m+1)}$  according to (3.47) for fixed  $(\mathbf{w}^{(m)}; \mathbf{b}^{(m)})$ ;

Step 3. Compute  $\mathbf{w}^{(m+1)}$  according to (3.48) for fixed  $(u^{(m+1)}; \mathbf{b}^{(m)})$ ;

Step 4. Update  $\mathbf{b}^{(m+1)}$  according to (3.42);

Step 5. If a stopping criterion is satisfied, stop; else  $m \leftarrow m + 1$ , repeat 2.

---

### 3.5.3 Split Bregman Algorithm for the improved KKWV model

For the improved KKWV model, we convert the original problem

$$\min_{u \in \mathcal{S}(\Omega)} \left\{ \mathcal{J}_{\text{ASN}}^{\text{improved KKWV}}(u) = \int_{\Omega} \frac{(u - z)^2}{u} d\Omega + \alpha_1 \int_{\Omega} |\nabla u| + \alpha_2 \int_{\Omega} \frac{|\nabla u|}{u} \right\}$$

into the following form

$$\min_{u, \mathbf{w}} \left\{ \bar{\mathcal{J}}_{\text{ASN}}^{\text{improved KKWV}}(u, \mathbf{w}; \mathbf{b}) = \int_{\Omega} |\mathbf{w}| d\Omega + \frac{\theta}{2} \int_{\Omega} (\mathbf{w} - \nabla u - \mathbf{b})^2 + F(u; \alpha_1, \alpha_2) d\Omega \right\}. \quad (3.49)$$

Next, we solve two subproblems for  $u, \mathbf{w}$  and update  $\mathbf{b}$  as follows:

$$u^{(m+1)} = \arg \min_{u > 0} \left\{ \frac{\theta}{2} \int_{\Omega} (\mathbf{w}^{(m)} - \nabla u - \mathbf{b}^{(m)})^2 + F(u; \alpha_1, \alpha_2) d\Omega \right\}, \quad (3.50)$$

$$\mathbf{w}^{(m+1)} = \arg \min_{\mathbf{w}} \left\{ \int_{\Omega} |\mathbf{w}| d\Omega + \frac{\theta}{2} \int_{\Omega} (\mathbf{w} - \nabla u^{(m+1)} - \mathbf{b}^{(m)})^2 d\Omega \right\}, \quad (3.51)$$

$$\mathbf{b}^{(m+1)} = \mathbf{b}^{(m)} + \nabla u^{(m+1)} - \mathbf{w}^{(m+1)}. \quad (3.52)$$

This process is repeated until one of the stopping rules given in (3.31) and (3.32) is satisfied.

**$u$ -subproblem.** Fixing variables  $(\mathbf{w}; \mathbf{b})$  in (3.50) yields the EL equation associated with  $u$  as follows:

$$\Delta u = \bar{G}(u) \quad (3.53)$$

where  $\bar{G}(u) = \nabla \cdot (\mathbf{w} - \mathbf{b}) + \frac{1}{\theta} \cdot \frac{u^2 - z^2}{\alpha_1 u^2 + \alpha_2 u}$ . In order to solve the nonlinear PDE in (3.53), we apply the simple linearized iterations by the following

$$\gamma_1 u^{[\nu+1]} - \Delta u^{[\nu+1]} = G(u^{[\nu]}) \quad (3.54)$$

where  $G(u^{[\nu]}) = \bar{G}(u^{[\nu]}) + \gamma_1 u^{[\nu]}$  and  $\gamma_1 > 0$  is the FP parameter used to stabilize numerical computation.

We use the similar procedure in section 3.5.1 and 3.5.3 to solve the nonlinear PDE (3.54). Hence, we have

$$\mathcal{F}\{\gamma_1 (u^{[\nu+1]})_{i,j} - (\Delta u^{[\nu+1]})_{i,j}\} = \mathcal{F}\{G(u^{[\nu]})_{i,j}\} \quad (3.55)$$

where  $\mathcal{F}$  denoted the DFT operator. For the discrete frequencies  $r \in [0, M)$  and  $s \in [0, N)$ , we have

$$\zeta \mathcal{F}\{(u^{[\nu+1]})_{i,j}\} = \mathcal{F}\{(G(u^{[\nu]}))_{i,j}\} \quad (3.56)$$

where  $\zeta = \gamma_1 - 2(\cos(\frac{2\pi s}{N}) + \cos(\frac{2\pi r}{M}) - 2)$ ,  $i \in [1, M]$  and  $j \in [1, N]$  are the indexes in the discrete time domain. For each outer step  $\nu$ , we finally have a closed-form solution of  $u^{[\nu+1]}$  at grid point  $(i, j)$

$$(u^{[\nu+1]})_{i,j} = \text{Re}(\mathcal{F}^{-1}(\frac{\mathcal{F}((G(u^{[\nu]}))_{i,j})}{\zeta})), \quad (3.57)$$

where  $\mathcal{F}^{-1}$  denotes the inverse DFT operator.  $\text{Re}$  is the real part of a complex number. ‘—’ represents for point-wise division of matrices.

**$\mathbf{w}$ -subproblem.** Fixing variables  $(u; \mathbf{b})$  in (3.51) yields the EL equation associated with  $\mathbf{w}$  as follows:

$$\frac{\mathbf{w}}{|\mathbf{w}|} + \theta(\mathbf{w} - \nabla u - \mathbf{b}) = 0.$$

The solution can be determined using the closed-form formula [44]

$$(\mathbf{w})_{i,j} = \max(|\nabla(u)_{i,j} + (\mathbf{b})_{i,j}| - \frac{1}{\theta}, 0) \frac{\nabla(u)_{i,j} + (\mathbf{b})_{i,j}}{|\nabla(u)_{i,j} + (\mathbf{b})_{i,j}|}, \quad (3.58)$$

with the convention  $0/0 = 0$ .

Algorithm 3 summarizes the SB method for the improved KKWV model.

### Algorithm 3 : Split Bregman Algorithm for the improved KKWV Model

Denote by

- $u$  the restored image
- $z$  the noisy image
- $\mathbf{w}$  the auxiliary spitting vector variable
- $\mathbf{b}$  the Bregman iterative parameter
- $\alpha_1$  the weighting parameter
- $\alpha_2$  the weighting parameter
- $\gamma_1$  the FP parameter
- $\theta$  the penalty parameter

$$[u] \leftarrow \text{SB}(u, z, \mathbf{w}, \mathbf{b}, \alpha_1, \alpha_2, \gamma_1, \theta)$$

---

Step 1. Initialization, set  $u = z, m = 0$  and  $\mathbf{w}^{(m)} = \mathbf{b}^{(m)} = \mathbf{0}$   
and choose  $\alpha_1, \alpha_2, \gamma_1, \theta > 0$ ;

Step 2. Compute  $u^{(m+1)}$  according to (3.57) for fixed  $(\mathbf{w}^{(m)}; \mathbf{b}^{(m)})$ ;

Step 3. Compute  $\mathbf{w}^{(m+1)}$  according to (3.58) for fixed  $(u^{(m+1)}; \mathbf{b}^{(m)})$ ;

Step 4. Update  $\mathbf{b}^{(m+1)}$  according to (3.52);

Step 5. If a stopping criterion is satisfied, stop; else  $m \leftarrow m + 1$ , repeat 2.

---

# Chapter 4

## A First-Order Variational Model and Its Numerical Algorithm

From a practical point of view, a fundamental assumption concerning only pure MSN or ASN as modeled and given respectively by (3.2) or (3.3) is inadequate for SN reduction in US images. The reason is that the complex image formation process is considered. The first main contribution of this thesis is then to propose a new first-order variational model for removal of combined ASN and MSN in US images and an efficient algorithm for its numerical approximation. The proposed model is designed to utilize the two data fidelity terms in (3.21) and (3.23) for dealing with the ASN and MSN corrupted in the noisy images and TV regularization for preserving sharp edges while removing unwanted oscillations and noise.

### 4.1 Introduction

Due to the similarity between the processes of producing the SAR and US images [46], we now assume that the noise in US images can be modeled as corrupted with the combination of ASN and MSN components of the form

$$z = u + k_0\sqrt{u}\eta + k_1u\zeta, \quad (4.1)$$

where  $k_0$  and  $k_1$  are positive constants, respectively. Here we also assume that both noise distributions, Gaussian noise  $\eta$  and Gamma noise  $\zeta$ , are independently

contaminated in  $z$ . In order to remove this type of mixed noise on the US images, we first proposed a new first-order variational model as follows.

## 4.2 A New First-Order Variational Model

In order to remove mixed noise on the US images, our proposed model is formulated via the following minimization:

$$\min_{u \in S(\Omega)} \{ \mathcal{J}_{\text{ASN-MSN}}^{\text{TV}}(u) = \mathcal{D}_{\text{ASN-MSN}}^{\text{New}}(u, z) + \mathcal{R}^{\text{TV}}(u) \}, \quad (4.2)$$

where

$$\begin{aligned} \mathcal{D}_{\text{ASN-MSN}}^{\text{New}}(u, z) &= \gamma_1 \int_{\Omega} \frac{(u-z)^2}{u} d\Omega + \gamma_2 \int_{\Omega} (u + ze^{-u}) d\Omega, \\ \mathcal{R}^{\text{TV}}(u) &= \int_{\Omega} |\nabla u| d\Omega, \end{aligned}$$

$\gamma_1$  and  $\gamma_2$  are the weighting parameters used to balance between the two fidelity terms, respectively.

### 4.2.1 Existence and Uniqueness of the Solution

It is necessary to discuss about the existence and uniqueness of the solution to the minimization problem (4.2).

**Theorem 4.1.** *Assume that  $\gamma_1 > 0$ ,  $\gamma_2 > 0$  and  $z > 0$  is in  $L^\infty(\Omega)$ . Then the minimization problem in (4.2) has a unique solution in  $S(\Omega) = \{u \in BV(\Omega), u > 0\}$ .*

*Proof.* We first show that  $\mathcal{J}_{\text{ASN-MSN}}^{\text{TV}}(u)$  is BV-coercivity. For each  $u \in S(\Omega)$ , the BV-coercivity of  $\mathcal{J}_{\text{ASN-MSN}}^{\text{TV}}(u)$  follows provided  $\mathcal{J}_{\text{ASN-MSN}}^{\text{TV}}(u) \rightarrow +\infty$  as  $\|u\|_{BV} \rightarrow +\infty$ , where  $\|\cdot\|_{BV}$  is the total variation norm, and is analogous to  $\int_{\Omega} |\nabla u| d\Omega$  for  $u \in C_0^1(\Omega)$ ; see [1]. For (4.2), we have

$$\int_{\Omega} \frac{(u-z)^2}{u} d\Omega \geq 0 \quad (4.3)$$

and

$$\int_{\Omega} (u + ze^{-u}) d\Omega \geq 0. \quad (4.4)$$



It follows that  $\|u\|_{BV} \leq \mathcal{J}_{ASN-MSN}^{TV}(u)$  up to a constant. Thus, the coercivity condition holds.

Next, we obtain the weakly lower semi-continuity of (4.3) and (4.4) as proven in [35] and [36] and for  $\|u\|_{BV}$  as proven in [1]. Due to  $\mathcal{J}_{ASN-MSN}^{TV}(u)$  being lower semi-continuous and BV-coercive, the existence of the solution is guaranteed as shown in Acar and Vogel [1, Thm 3.1].

Finally, the solution is unique due to each term in  $\mathcal{J}_{ASN-MSN}^{TV}(u)$  being strictly convex, as also shown in [1, 35, 36].  $\square$

The following lemma leads to the EL equation of the proposed model (4.2).

**Lemma 4.2.** *Let  $\Phi(u) : (0, \infty) \rightarrow (0, \infty)$  be a  $C^1$  function and*

$$\mathcal{J}_{ASN-MSN}^{TV}(u) = \mathcal{D}_{ASN-MSN}^{New}(u, z) + \mathcal{R}^{TV}(u)$$

*then the formal equilibrium EL equation of  $\mathcal{J}_{ASN-MSN}^{TV}(u)$  is given by*

$$\begin{aligned} \gamma_1 \left(1 - \frac{z^2}{u^2}\right) + \gamma_2 (1 - ze^{-u}) + \left(-\nabla \cdot \left(\frac{\nabla u}{|\nabla u|}\right)\right) &= 0 \text{ on } \Omega \\ \frac{\partial u}{\partial \mathbf{n}} &= 0 \text{ on } \partial\Omega, \end{aligned}$$

*where  $\mathbf{n}$  is the unit outward normal vector on the image boundary  $\partial\Omega$ .*

*Proof.* We consider  $\delta \mathcal{J}_{ASN-MSN}^{TV}(u) = 0$ . That is  $\delta \mathcal{D}_{ASN-MSN}^{New}(u, z) + \delta \mathcal{R}^{TV}(u) = 0$ .

Since  $\mathcal{D}_{ASN-MSN}^{New}(u, z) = \gamma_1 \int_{\Omega} \frac{(u-z)^2}{u} d\Omega + \gamma_2 \int_{\Omega} (u + ze^{-u}) d\Omega$ , we have

$$\begin{aligned} \delta \mathcal{D}_{ASN-MSN}^{New}(u, z; v) &= \frac{d}{d\epsilon} \mathcal{D}_{ASN-MSN}^{New}(u + \epsilon v, z; v) \Big|_{\epsilon=0} \\ &= \gamma_1 \int_{\Omega} \frac{d}{d\epsilon} \frac{(u + \epsilon v - z)^2}{u + \epsilon v} \Big|_{\epsilon=0} d\Omega \\ &\quad + \gamma_2 \int_{\Omega} \frac{d}{d\epsilon} (u + \epsilon v + ze^{-(u+\epsilon v)}) \Big|_{\epsilon=0} d\Omega \\ &= \gamma_1 \int_{\Omega} \frac{2v(u + \epsilon v)(u + \epsilon v - z) - v(u + \epsilon v - z)^2}{(u + \epsilon v)^2} \Big|_{\epsilon=0} d\Omega \\ &\quad + \gamma_2 \int_{\Omega} (v - zve^{-(u+\epsilon v)}) \Big|_{\epsilon=0} d\Omega \\ &= \gamma_1 \int_{\Omega} \left(1 - \frac{z^2}{u^2}\right) v d\Omega + \gamma_2 \int_{\Omega} (1 - ze^{-u}) v d\Omega \\ &= \gamma_1 \int_{\Omega} \left\langle 1 - \frac{z^2}{u^2}, v \right\rangle d\Omega + \gamma_2 \int_{\Omega} \langle 1 - ze^{-u}, v \rangle d\Omega. \end{aligned}$$

Let  $\Phi(S) = S$ . Then  $\Phi(|\nabla u|) = |\nabla u|$ . We have that  $\mathcal{R}^{\text{TV}}(u) = \int_{\Omega} \Phi(|\nabla u|) d\Omega$ .

Then

$$\begin{aligned}
\delta\mathcal{R}^{\text{TV}}(u; v) &= \frac{d}{d\epsilon} \mathcal{R}^{\text{TV}}(u + \epsilon v; v) \Big|_{\epsilon=0} \\
&= \frac{d}{d\epsilon} \int_{\Omega} \Phi(|\nabla u + \epsilon \nabla v|) d\Omega \Big|_{\epsilon=0} \\
&= \int_{\Omega} \sum_{m=1}^2 \frac{\Phi'(|\nabla u + \epsilon \nabla v|)}{|\nabla u + \epsilon \nabla v|} (u_{x_m} + \epsilon v_{x_m}) \Big|_{\epsilon=0} d\Omega \\
&= \int_{\Omega} \frac{\Phi'(|\nabla u|)}{|\nabla u|} \nabla u \nabla v d\Omega \\
&= - \int_{\Omega} \nabla \cdot \left( \frac{\Phi'(|\nabla u|)}{|\nabla u|} \nabla u \right) \nabla v d\Omega + \int_{\partial\Omega} \frac{\Phi'(|\nabla u|)}{|\nabla u|} \nabla u \cdot \mathbf{n} dS.
\end{aligned}$$

Since  $\Phi(S) = S$ ,  $\Phi'(S) = 1$ . Then

$$\begin{aligned}
\delta\mathcal{D}_{\text{ASN-MSN}}^{\text{New}}(u, z; v) &= - \int_{\Omega} \nabla \cdot \left( \frac{\nabla u}{|\nabla u|} \right) v d\Omega + \int_{\partial\Omega} \frac{\nabla u}{|\nabla u|} \cdot \mathbf{n} dS \\
&= \int_{\Omega} \left\langle -\nabla \cdot \left( \frac{\nabla u}{|\nabla u|} \right), v \right\rangle d\Omega + \int_{\partial\Omega} \left\langle \frac{\nabla u}{|\nabla u|}, \mathbf{n} \right\rangle dS.
\end{aligned}$$

Since  $\delta\mathcal{D}_{\text{ASN-MSN}}^{\text{New}}(u, z) + \delta\mathcal{R}^{\text{TV}}(u) = 0$ , we have

$$\begin{aligned}
\gamma_1 \left( 1 - \frac{z^2}{u^2} \right) + \gamma_2 (1 - ze^{-u}) + \left( -\nabla \cdot \left( \frac{\nabla u}{|\nabla u|} \right) \right) &= 0 \text{ on } \Omega \\
\frac{\partial u}{\partial \mathbf{n}} &= 0 \text{ on } \partial\Omega.
\end{aligned}$$

Therefore the Euler-Lagrange equation is

$$\begin{aligned}
\gamma_1 \left( 1 - \frac{z^2}{u^2} \right) + \gamma_2 (1 - ze^{-u}) + \left( -\nabla \cdot \left( \frac{\nabla u}{|\nabla u|} \right) \right) &= 0 \text{ on } \Omega \\
\frac{\partial u}{\partial \mathbf{n}} &= 0 \text{ on } \partial\Omega.
\end{aligned}$$

□

## 4.2.2 Euler-Lagrange Equation

According to Lemma 4.2, the minimizer of  $\mathcal{J}_{\text{ASN-MSN}}^{\text{TV}}(u)$  in (4.2) satisfies the Euler-Lagrange (EL) equation:

$$\underbrace{-\mathcal{K}(u) + \gamma_1 \left( 1 - \frac{z^2}{u^2} \right) + \gamma_2 (1 - ze^{-u})}_{\mathcal{N}(u)} = 0, \quad (4.5)$$

subject to the Neumann boundary condition  $\frac{\partial u}{\partial \mathbf{n}} = 0$ , where  $\mathbf{n}$  is the unit outward normal vector on the image boundary  $\partial\Omega$  and  $\mathcal{K}(u) = \nabla \cdot \left( \frac{\nabla u}{|\nabla u|_\beta} \right)$ ,  $|\nabla u|_\beta = \sqrt{|\nabla u|^2 + \beta}$ , and  $0 < \beta \ll 1$  is small constant to avoid division by zero in numerical computations.

## 4.3 Numerical Solutions

### 4.3.1 Numerical Discretization

Let  $(u^h)_{i,j} = u^h(x_i, y_j)$  be the grid function with the uniform grid spacing  $h = \frac{1}{n}$ . Here the integer  $n = \frac{1}{h}$  is the number of uniform intervals in the  $x$  and  $y$  coordinate directions. Each grid point  $\mathbf{x}$  in the discretized domain  $\Omega^h \subset \Omega$  is vertex-centered and given by  $\mathbf{x} = (x_i, y_j)^\top = (ih, jh)^\top$  for  $1 \leq i, j \leq n$ . The partial derivatives in (4.5) are approximated by the standard second-order finite difference schemes. Therefore, the discrete nonlinear system is given by

$$\mathcal{N}^h(u^h)_{i,j} = 0, \quad (4.6)$$

where

$$\begin{aligned} \mathcal{N}^h(u^h)_{i,j} &= -\mathcal{K}^h(u^h)_{i,j} + \gamma_1 \left( 1 - \frac{(z^h)_{i,j}^2}{(u^h)_{i,j}^2} \right) + \gamma_2 \left( 1 - (z^h)_{i,j} e^{-(u^h)_{i,j}} \right), \\ \mathcal{K}^h(u^h)_{i,j} &= -\frac{1}{h^2} \left( (\sum^h)_{i,j}(u^h)_{i,j} - (\bar{\sum}^h)_{i,j}(u^h)_{i,j} \right), \\ (\sum^h)_{i,j}(u^h)_{i,j} &= (D_1(u^h)_{i,j} + D_2(u^h)_{i,j} + 2D_3(u^h)_{i,j})(u^h)_{i,j}, \\ (\bar{\sum}^h)_{i,j}(u^h)_{i,j} &= D_1(u^h)_{i,j}(u^h)_{i-1,j} + D_2(u^h)_{i,j}(u^h)_{i,j-1} \\ &\quad + D_3(u^h)_{i,j}(u^h)_{i+1,j} + D_3(u^h)_{i,j}(u^h)_{i,j+1}, \\ D_1(u^h)_{i,j} &= D(u^h)_{i-1,j}, \\ D_2(u^h)_{i,j} &= D(u^h)_{i,j-1}, \\ D_3(u^h)_{i,j} &= D(u^h)_{i,j}, \\ D(u^h)_{i,j} &= \frac{1}{\sqrt{(\delta_x^+(u^h)_{i,j}/h)^2 + (\delta_y^+(u^h)_{i,j}/h)^2 + \beta}}, \\ \delta_x^\pm(u^h)_{i,j} &= \pm((u^h)_{i\pm 1,j} - (u^h)_{i,j}), \\ \delta_y^\pm(u^h)_{i,j} &= \pm((u^h)_{i,j\pm 1} - (u^h)_{i,j}). \end{aligned}$$

We note that the approximations in (4.6) need to be adjusted at the image boundary  $\partial\Omega_h$  using the discrete boundary conditions  $(u^h)_{i,0} = (u^h)_{i,1}$ ,  $(u^h)_{i,n+1} = (u^h)_{i,n}$ ,  $(u^h)_{0,j} = (u^h)_{1,j}$ ,  $(u^h)_{n+1,j} = (u^h)_{n,j}$ . In the following sections the symbol ‘ $h$ ’ and  $(\cdot, \cdot)_{i,j}^h$  will sometimes drop for simplicity.

### 4.3.2 Method 1-Explicit Time Marching Method

We can see that the EL equation (4.6) is highly nonlinear discrete problem that is not easy to solve. In order to overcome the nonlinearity of  $\mathcal{N}$ , the gradient descent method, also known as explicit time marching (ETM) method, can be conveniently applied, and the iteration is then given by

$$(u^{(k+1)})_{i,j} = (u^{(k)})_{i,j} - \tau(-\mathcal{K}(u^{(k)})_{i,j} + \gamma_1(1 - \frac{(z)_{i,j}^2}{(u^{(k)})_{i,j}^2}) + \gamma_2(1 - (z)_{i,j}e^{-(u^{(k)})_{i,j}})), \quad (4.7)$$

where  $(u^{(k)})_{i,j} = u(x_i, y_j, t_k)$ ,  $t_k = t_0 + k\tau$ ,  $\tau > 0$  is the time-step and  $k = 0, 1, \dots$ . Although the above ETM method is simple for numerical implementation, this method is not efficient because the time step  $\tau$  is required to be very small for stability reasons.

### 4.3.3 Method 2-Fixed-Point Iteration Method

As is well known, the fixed-point (FP) method is also a possible option in solving the EL equations related to the TV minimization. For our proposed FP method, the nonlinear terms  $\frac{1}{|\nabla u|_\beta}$ ,  $\frac{1}{u}$  and  $e^{-u}$  represented in (4.5) or  $D(u)_{i,j}$ ,  $\frac{1}{(u)_{i,j}}$  and  $e^{-(u)_{i,j}}$  in (4.6) can be linearized or frozen globally at a previous FP step  $\nu$ . The simple linearized iterations is given by the following

$$\mathcal{N}[u^{[\nu]}]u^{[\nu+1]} = \mathcal{G}[u^{[\nu]}], \quad \nu = 0, 1, \dots \quad (4.8)$$

where

$$\begin{aligned} \mathcal{N}[u^{[\nu]}]u^{[\nu+1]} &= -\nabla \cdot \left( \frac{\nabla u^{[\nu+1]}}{|\nabla u^{[\nu]}|_\beta} \right) + \gamma_3 u^{[\nu+1]}, \\ \mathcal{G}[u^{[\nu]}] &= \gamma_1 \left( \frac{z^2}{(u^{[\nu]})^2} - 1 \right) + \gamma_2 \left( z e^{-u^{[\nu]}} - 1 \right) + \gamma_3 u^{[\nu]}, \end{aligned}$$

and  $\gamma_3 > 0$  represents the FP parameter for stabilizing the numerical computation. To solve the linearized discrete system (4.8), the successive over-relaxation (SOR)

method is applied with the relaxation parameter  $\omega \in (0, 2)$ . For each FP step  $\nu$ , the new iteration at each grid point  $(i, j)$  is given by

$$(u^{[\nu+1, k+1]})_{i,j} = (1 - \omega) (u^{[\nu+1, k]})_{i,j} + \omega (\mathcal{N}[u^{[\nu]}])_{i,j}^{-1} (\mathcal{G}[u^{[\nu, k+1/2]}])_{i,j} \quad (4.9)$$

where

$$\begin{aligned} (\mathcal{N}[u^{[\nu]}])_{i,j}^{-1} &= ((1/h^2)(\Sigma^{[\nu]})_{i,j} + \gamma_3)^{-1}, \\ (\mathcal{G}[u^{[\nu, k+1/2]}])_{i,j} &= \gamma_1 \left( \frac{(z)_{i,j}^2}{(u^{[\nu]})_{i,j}^2} - 1 \right) + \gamma_2 ((z)_{i,j} e^{-(u^{[\nu]})_{i,j}} - 1) \\ &\quad + \gamma_3 (u^{[\nu]})_{i,j} + (1/h^2)(\bar{\Sigma}^{[\nu]})_{i,j} (u^{[\nu+1, k+1/2]})_{i,j}. \end{aligned}$$

Here the superscripts  $k$ ,  $k+1/2$  and  $k+1$  denote the current, intermediate and new approximations computed by the SOR method, respectively.

#### 4.3.4 Method 3-Split Bregman Method

Alternating direction method of multipliers (ADMM) has been successfully applied to minimize the energy functional involving TV regularization and quadratic or non-quadratic data fitting term. For example, the authors in [26] used the split Bregman (SB) iteration to solve the TV model, while the augmented Lagrangian method (ALM) has been developed for the ROF model in [56, 62]. Note that both SB and ALM employ ADMM to minimize their energy functionals and the convergence of ADMM is always guaranteed. In [56, 62], the authors have proven that the two methods are in fact equivalent. For applying ADMM to minimize the energy functionals, we refer to [4, 28, 32, 34, 63].

As can be seen, both Method 1 and Method 2 share two drawbacks. At first, they provide only the approximate solutions of the original problem (4.2), since the TV regularization

$$\mathcal{R}^{\text{TV}}(u) = \int_{\Omega} |\nabla u| d\Omega = \int_{\Omega} \sqrt{u_x^2 + u_y^2} d\Omega$$

is replaced with

$$\mathcal{R}^{\beta\text{TV}}(u) = \int_{\Omega} \sqrt{u_x^2 + u_y^2 + \beta} d\Omega$$

to avoid non-differentiability of  $\mathcal{R}^{\text{TV}}(u)$ . On the second, the choice of  $\beta$  will effect on the computational efficiency of the numerical methods and the smoothness of

the restored images. Larger the  $\beta$ , more efficient the methods are, whereas more smooth the constructed images will be. Therefore the performance of the proposed model in removing SN and preserving edges by these two methods is very sensitive to the parameter  $\beta$ .

In order to deal with TV regularization, in this work, we propose to solve our noise removal model (4.2) by split Bregman (SB) method. Instead of solving (4.2) directly, we first introduce an auxiliary scalar variable  $\mathbf{w}$ , a Bregman iterative parameter  $\mathbf{b}$ , and a positive penalty parameter  $\theta$ , and then consider the following equivalent unconstrained minimization problem (4.2):

$$\min_{u>0, \mathbf{w}} \{ \mathcal{J}_{\text{ASN-MSN}}^{\text{TV}}(u, \mathbf{w}; \mathbf{b}) = \mathcal{D}_{\text{ASN-MSN}}^{\text{New}}(u, z) + \int_{\Omega} |\mathbf{w}| d\Omega + \frac{\theta}{2} \int_{\Omega} (\mathbf{w} - \nabla u - \mathbf{b})^2 d\Omega \} \quad (4.10)$$

where

$$\mathcal{D}_{\text{ASN-MSN}}^{\text{New}}(u, z) = \gamma_1 \int_{\Omega} \frac{(u - z)^2}{u} d\Omega + \gamma_2 \int_{\Omega} (u + ze^{-u}) d\Omega$$

represent the non-quadratic data fidelity term.

Clearly, both variables  $u$  and  $\mathbf{w}$  are very difficult to solve simultaneously. We then separate the minimization problem in (4.10) into two subproblems:

$$u^{(m+1)} = \arg \min_{u>0} \{ \mathcal{D}_{\text{ASN-MSN}}^{\text{New}}(u, z) + \frac{\theta}{2} \int_{\Omega} (\mathbf{w}^{(m)} - \nabla u - \mathbf{b}^{(m)})^2 d\Omega \}, \quad (4.11)$$

$$\mathbf{w}^{(m+1)} = \arg \min_{\mathbf{w}} \{ \int_{\Omega} |\mathbf{w}| d\Omega + \frac{\theta}{2} \int_{\Omega} (\mathbf{w} - \nabla u^{(m+1)} - \mathbf{b}^{(m)})^2 d\Omega \}, \quad (4.12)$$

and use an alternating minimization procedure as proposed in Algorithm 4 to approximate the solution. Here the Bregman iterative parameter is update by

$$\mathbf{b}^{(m+1)} = \mathbf{b}^{(m)} + \nabla u^{(m+1)} - \mathbf{w}^{(m+1)}. \quad (4.13)$$

This process is repeated until one of the following stopping rules is satisfied:

$$\frac{\|u^{(m+1)} - u^{(m)}\|^2}{\|u^{(m)}\|^2} < \epsilon_1^{\text{SB}}, \quad (4.14)$$

$$m \geq \epsilon_2^{\text{SB}}, \quad (4.15)$$

where  $\epsilon_1^{\text{SB}}$  denotes the predefined small positive number and  $\epsilon_2^{\text{SB}}$  denotes the maximum iteration of the SB method. Here  $m$  represents the index of the current iteration.

The two subproblems can be solved as follows:

**$u$ -subproblem.** Fixing variables  $(\mathbf{w}; \mathbf{b})$  in (4.11) yields the EL equation associated with  $u$  as follows:

$$\Delta u = \bar{G}(u) \quad (4.16)$$

where  $\bar{G}(u) = \nabla \cdot (\mathbf{w} - \mathbf{b}) + \frac{\gamma_1}{\theta} \left(1 - \frac{z^2}{u^2}\right) + \frac{\gamma_2}{\theta} (1 - ze^{-u})$ . To solve the nonlinear partial differential equation in (4.16), we firstly apply the simple linearized iterations by the following

$$\gamma_3 u^{[\nu+1]} - \Delta u^{[\nu+1]} = G(u^{[\nu]}) \quad (4.17)$$

where  $G(u^{[\nu]}) = \bar{G}(u^{[\nu]}) + \gamma_3 u^{[\nu]}$  and  $\gamma_3 > 0$  is the FP parameter used to stabilize numerical computation. Secondly, we assume that  $\Omega = [1, M] \times [1, N]$  and  $\bar{\Omega} \subset \Omega$  is the discretized image domain where

$$\bar{\Omega} = \{(x, y) = (x_i, y_j) \in \Omega, x_i = i, y_j = j, 1 \leq i \leq M \text{ and } 1 \leq j \leq N\}.$$

Next, we discretize the linearized partial differential equation (4.17) using the standard finite difference method subject to periodic boundary conditions. Therefore, the discrete Fourier transform (DFT) method can be directly applied as follows:

$$\mathcal{F}\{\gamma_3 (u^{[\nu+1]})_{i,j} - (\Delta u^{[\nu+1]})_{i,j}\} = \mathcal{F}\{G(u^{[\nu]})_{i,j}\} \quad (4.18)$$

where  $\mathcal{F}$  denoted the DFT operator. For the discrete frequencies  $r \in [0, M)$  and  $s \in [0, N)$ , we have

$$\zeta \mathcal{F}\{(u^{[\nu+1]})_{i,j}\} = \mathcal{F}\{(G(u^{[\nu]}))_{i,j}\} \quad (4.19)$$

where  $\zeta = \gamma_3 - 2(\cos(\frac{2\pi r}{N}) + \cos(\frac{2\pi r}{M}) - 2)$ ,  $i \in [1, M]$  and  $j \in [1, N]$  are the indexes in the discrete time domain. For each outer step  $\nu$ , we finally have a closed-form solution of  $u^{[\nu+1]}$  at grid point  $(i, j)$

$$(u^{[\nu+1]})_{i,j} = \text{Re}(\mathcal{F}^{-1}(\frac{\mathcal{F}((G(u^{[\nu]}))_{i,j})}{\zeta})), \quad (4.20)$$

where  $\mathcal{F}^{-1}$  denotes the inverse DFT operator.  $\text{Re}$  is the real part of a complex number. ‘—’ represents for point-wise division of matrices.

**$w$ -subproblem.** Fixing variables  $(u; \mathbf{b})$  in (4.12) yields the EL equation associated with  $w$  as follows:

$$\frac{w}{|w|} + \theta(\mathbf{w} - \nabla u - \mathbf{b}) = 0.$$

The solution can be determined using the closed-form formula [44]

$$(\mathbf{w})_{i,j} = \max(|\nabla(u)_{i,j} + (\mathbf{b})_{i,j}| - \frac{1}{\theta}, 0) \frac{\nabla(u)_{i,j} + (\mathbf{b})_{i,j}}{|\nabla(u)_{i,j} + (\mathbf{b})_{i,j}|}, \quad (4.21)$$

with the convention  $0/0 = 0$ .

#### Algorithm 4 : Split Bregman Algorithm for the Proposed First-Order Variational Model

Denote by

- $u$  the restored image
- $z$  the noisy image
- $\mathbf{w}$  the auxiliary spitting vector variable
- $\mathbf{b}$  the Bregman iterative parameter
- $\gamma_1$  the weighting parameter
- $\gamma_2$  the weighting parameter
- $\gamma_3$  the FP parameter
- $\theta$  the penalty parameter

$$[u] \leftarrow \text{SB}(u, z, \mathbf{w}, \mathbf{b}, \gamma_1, \gamma_2, \gamma_3, \theta)$$

---

Step 1. Initialization, set  $u = z, m = 0$  and  $\mathbf{w}^{(m)} = \mathbf{b}^{(m)} = \mathbf{0}$   
and choose  $\gamma_1, \gamma_2, \gamma_3, \theta > 0$ ;

Step 2. Compute  $u^{(m+1)}$  according to (4.20) for fixed  $(\mathbf{w}^{(m)}; \mathbf{b}^{(m)})$ ;

Step 3. Compute  $\mathbf{w}^{(m+1)}$  according to (4.21) for fixed  $(u^{(m+1)}; \mathbf{b}^{(m)})$ ;

Step 4. Update  $\mathbf{b}^{(m+1)}$  according to (4.13);

Step 5. If a stopping criterion is satisfied, stop; else  $m \leftarrow m + 1$ , repeat 2.

---

The alternating minimization procedure mentioned above can be summarized as shown in Algorithm 4. This proposed algorithm is efficient. At each iteration, the computation requires to solve two subproblems. On one hand for the  $u$ -subproblem, the objective functional in (4.11) is strictly convex, which implies a unique solution, and the solution can be determined by using the proposed FP method as given by (4.20) (usually takes 10 – 15 iteration in our experiments). On the other hand for the  $\mathbf{w}$ -subproblem, it has a closed-form solution as given in (4.21). According to [6, 23, 52] the convergence of the algorithm is guaranteed as long as the sequences of



optimization errors with respect to  $u$  (in Step 2) and  $\mathbf{w}$  (in Step 3) are absolutely summable. That is to say Steps 2 do not have to be solved exactly (In all our experiments, we take only ten iterations in Step 2.).

## 4.4 Numerical Results and Discussion

In this section, we carry out numerical experiments from several test cases for both synthetic and real US images to

1. compare the noise reduction results of the proposed TV model in (4.2) with existing three existing noise removal models, the JY model [35], KKWV model [40] and improved KKWV model [21].
2. illustrate the overall performances of the three numerical solutions, ETM, FP and proposed SB methods.

We note first that all experiments were performed using MATLAB R2019a on a machine with an Intel Core i5 at 2.3GHz with 8 GB of RAM. Second, the peak signal to noise ratio (PSNR) between the original and restored images is used to measure the quality of image restoration results; a higher PSNR value indicates the higher quality of the restored image (better). The PSNR is defined as follows:

$$\text{PSNR} = 10 \log \left( \frac{255^2}{\text{MSE}} \right),$$

where  $\text{MSE} = \frac{1}{NM} \sum_{i=1}^M \sum_{j=1}^N ((u^*)_{i,j} - (u)_{i,j})^2$ . Here  $u$  and  $u^*$  are the original image and the restored image, respectively. Note that all numerical methods for each model will be repeated until the following stopping criteria based on the relative error of the solution is satisfied

$$\frac{\| u^{[\text{new}]} - u^{[\text{old}]} \|_{l_2}^2}{\| u^{[\text{old}]} \|_{l_2}^2} < 10^{-5}. \quad (4.22)$$

### Results on synthetic images

In our first test, the standard test images in Figure 4.1: “Ring” “Boat” and “Barbara” are used to compare the performance between three competing noise removal models in the literature and the one proposed in this work. Note that the size

of test images are all the same, which is  $256 \times 256$  pixels. We also note that, we implement the ETM methods for all models to make a fair comparison. Here, the images are corrupted by different levels of noise strength. According to the noise formation model as given by (4.1), there are two cases to be considered. First, we test on different levels of noise strength by using the fixed value of  $k_0 = 0.5$  and different values of  $k_1 = \frac{1}{100}, \frac{1}{75}, \frac{1}{50}, \frac{1}{25}, \frac{1}{10}$  to see the effects of Gamma noise  $\zeta$  on quality improvement of the restored images. Second, we use the fixed value of  $k_1 = \frac{1}{100}$  and different values of  $k_0 = 0.5, 0.75, 1, 1.25$  to see the effects of Gaussian noise  $\eta$  on quality improvement of the restored images. We note that the parameters  $\beta = 10^{-4}$ ,  $\tau \in [10^{-5}, 10^{-4}]$  and  $\gamma_3 \in [10, 10^3]$  are used in this test, where  $\tau$  and  $\gamma_3$  are manually selected for each noise removal problem. Tables 4.1 and 4.2 show the restoration results for the first and second cases, respectively. Table 4.3 summarizes the restoration results for the case, where the test images are corrupted with four different levels of Gaussian noise and five different levels of Gamma noise. As can be seen, the average PSNR of the restored images by the proposed model is more accurate and robust than the other three noise removal models for different levels of noise strength.



Figure 4.1: The original test images.

Model	Ring	Boat	Barbara
Proposed Model	<b>37.7740</b>	<b>29.0951</b>	<b>29.8553</b>
JY Model	36.7811	28.9229	29.7121
KKWV Model	33.1726	26.1507	26.9316
Improved KKWV Model	33.2747	26.2220	26.9978

Table 4.1: Performance comparison using the average PSNR of the restored images by four noise removal models with several levels of noise strength, where the test images are corrupted with a fixed level of Gaussian noise and five different levels of Gamma noise.

Model	Ring	Boat	Barbara
Proposed Model	<b>41.1206</b>	<b>30.5264</b>	<b>31.0669</b>
JY Model	41.1036	<b>30.5264</b>	31.0490
KKWV Model	40.2642	29.6509	30.2900
Improved KKWV Model	40.3775	30.3871	30.8069

Table 4.2: Performance comparison using the average PSNR of the restored images by four noise removal models with several levels of noise strength, where the test images are corrupted with a fixed level of Gamma noise and four different levels of Gaussian noise.

Model	Ring	Boat	Barbara
Proposed Model	<b>38.6602</b>	<b>29.1531</b>	<b>29.8564</b>
JY Model	38.0312	29.0455	29.7579
KKWV Model	35.7750	27.0906	27.8380
Improved KKWV Model	35.8480	27.5033	28.1348

Table 4.3: Performance comparison using the average PSNR of the restored images by four noise removal models with several levels of noise strength, where the test images are corrupted with four different levels of Gaussian noise and five different levels of Gamma noise.

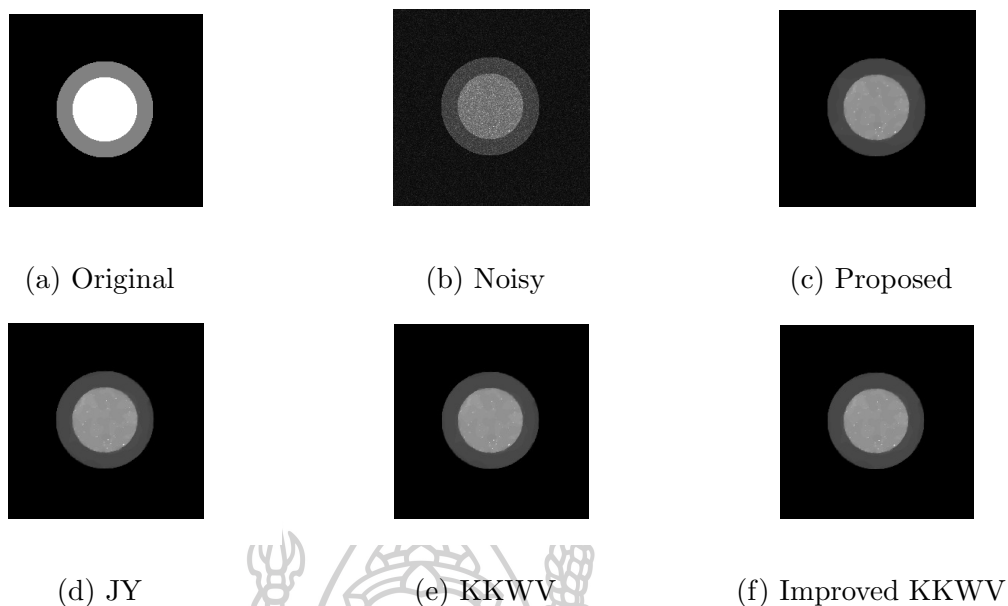


Figure 4.2: Performance comparison of the restored images by four noise removal models with  $k_0 = 0.5$  and  $k_1 = \frac{1}{10}$ ; (a) original image; (b) noisy image; (c)-(f) restoration results by proposed, JY, KKWV and improved KKWV models respectively.

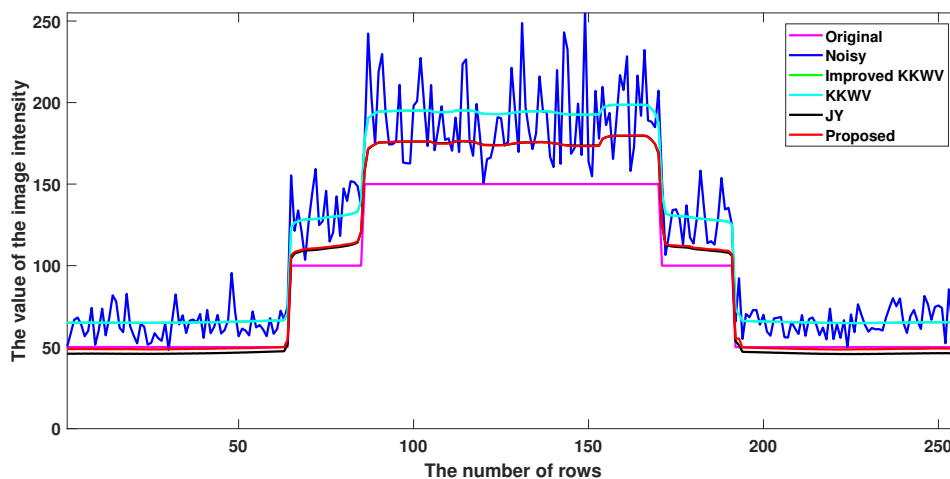


Figure 4.3: Corresponding signals of one column 128 of the Ring image in figure 4.2.

Method	Ring	Boat	Barbara
ETM Method	41.1206	30.5264	31.0669
FP Method	42.0911	29.5537	30.0121
Proposed SB Method	<b>44.7128</b>	<b>32.0729</b>	<b>31.6899</b>

Table 4.5: Performance comparison using the average PSNR of the restored images by three numerical solutions with several levels of SN strength, where the test images are corrupted with a fixed level of Gamma noise and four different levels of Gaussian noise.

Method	Ring	Boat	Barbara
ETM Method	38.6602	29.1531	29.8564
FP Method	38.4731	28.0264	28.7448
Proposed SB Method	<b>41.6659</b>	<b>31.6570</b>	<b>31.5015</b>

Table 4.6: Performance comparison using the average PSNR of the restored images by three numerical solutions with several levels of noise strength, where the test images are corrupted with four different levels of Gaussian noise and five different levels of Gamma noise.

Method	Ring	Boat	Barbara
ETM Method	37.7740	29.0951	29.8553
FP Method	36.2722	29.1733	28.0407
Proposed SB Method	<b>39.3677</b>	<b>31.8719</b>	<b>31.6242</b>

Table 4.4: Performance comparison using the average PSNR of the restored images by three numerical solutions with several levels of noise strength, where the test images are corrupted with a fixed level of Gaussian noise and five different levels of Gamma noise.

## Results on real US images

Next, we test the performance of the proposed model and compared with the other three noise removal models in removing mixed noise from the two real US images, which are “baby” and “kidney”. We note that the test images are contaminated by the unknown noise strength and have the same size of  $256 \times 256$ . As shown in Figures 4.4 and 4.5, the first and second columns show the real US images and the restores images by the proposed model, respectively. The third, fourth and fifth columns show respectively the restored images by the JY, KKWV and improved KKWV models. Figures 4.6 and 4.11 show the corresponding signal of one column at different columns (named by the highlight line) extracted from the original image and the restored images by the JY, KKWV, improved KKWV, proposed models. The horizontal axis is the pixel along the highlight line and the vertical axis is the intensity value. Digits 1-3 are marked along the highlight line. Here the areas in Digit 1 (the local change of intensity) and Digit 2 (the significant local change of intensity) should be well preserved and the area in Digit 3 (the homogeneous regions) should be smoothed in SN reduction. In the aspect of protection Digit 1, we can see from Figure 4.6 and 4.11. that the JY, KKWV and improved KKWV models are not successful as the proposed model. Moreover, it is clear from Figure 4.11 that our proposed model outperforms to protect the significant local change in Digit 2 over the other three SN removal models. However, all models are able to smooth the homogeneous in Digit 3 as shown in Figures 4.6 and 4.11. These evidence from Figures 4.4-4.15 clearly support us that our proposed model is the most effective noise removal model among the four for the real US images.

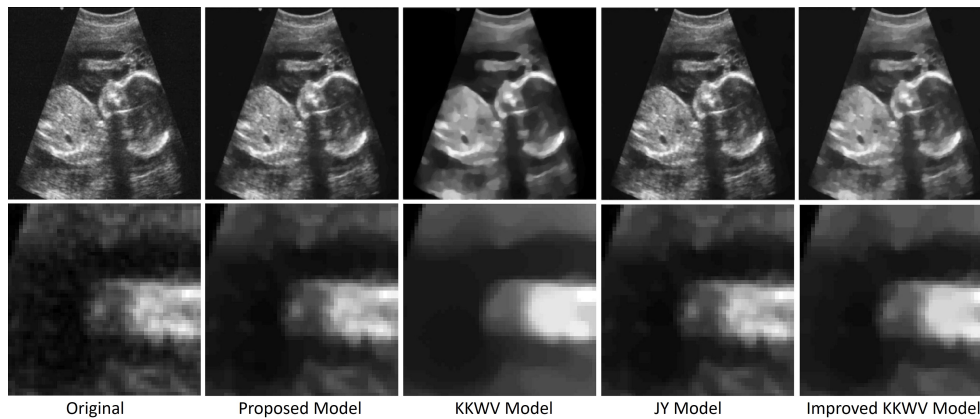


Figure 4.4: Performance comparison of different noise removal models on the baby image. Top: The original and restored images. Bottom: the magnification of the original and restored images.

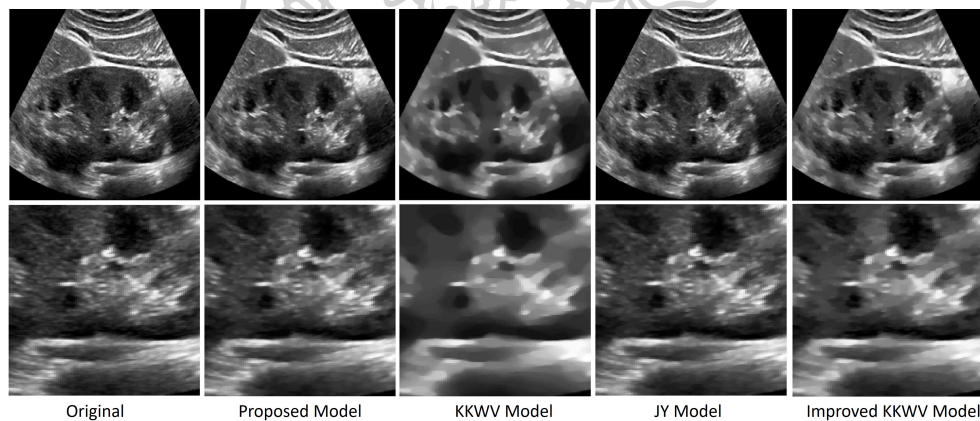


Figure 4.5: Performance comparison of different noise removal models on the kidney image. Top: The original and restored images. Bottom: the magnification of the original and restored images.

In our second test, the aim is to illustrate the performance among three numerical solutions discussed in the previous section. The test images with the  $256 \times 256$  pixels as shown in Figure 4.1 are also used here and distorted by different levels of noise strength divided into two cases as performed in our first test. By experiments we note that the parameters  $\beta = 10^{-4}$ ,  $\tau \in [10^{-5}, 10^{-4}]$ ,  $\gamma_3 \in [10, 10^3]$ ,  $\epsilon_1^{\text{SB}} = 10^{-5}$  and  $\epsilon_2^{\text{SB}} = 10^3$  are used in this test, where  $\tau$  and  $\gamma_3$  are well-selected for each noise

reduction problem. Tables 4.4 and 4.5 show the restoration results for the first and second cases, respectively. Table 4.6 summarizes the restoration results for the case, where the test images are corrupted with four different levels of Gaussian noise and five different levels of Gamma noise. As expected from the previous section, Tables 4.5-4.6 confirm us that the SB method is more accurate and robust than the ETM and FP methods in delivering high-quality image restoration results, while the ETM is less efficient.

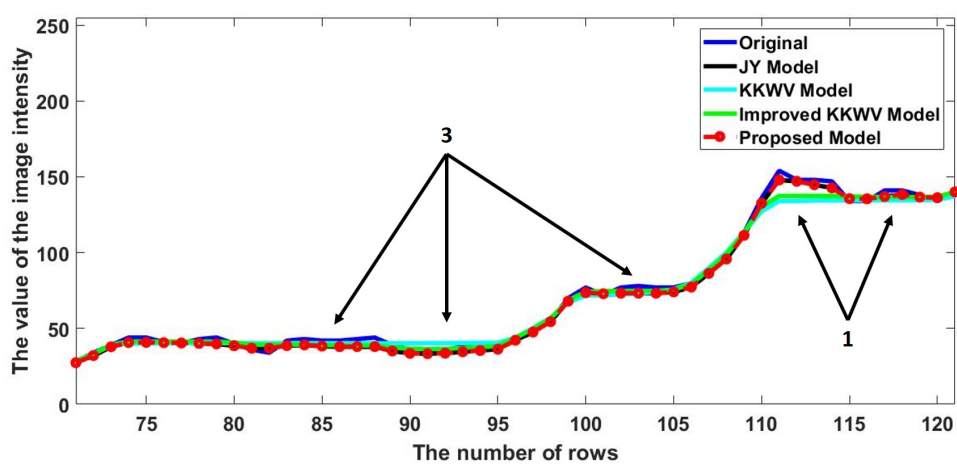


Figure 4.6: Corresponding signals of the 75th column with different rows ranging from 70 to 120, extracted from the baby image and the restored images by four noise removal models.



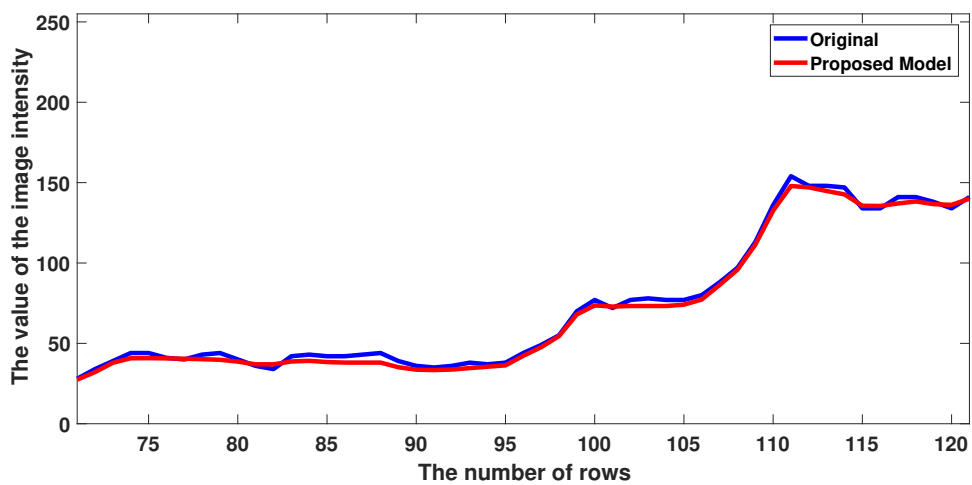


Figure 4.7: Corresponding signals of the 75th column with different rows ranging from 70 to 120, extracted from the kidney image and the restored images by the proposed model.

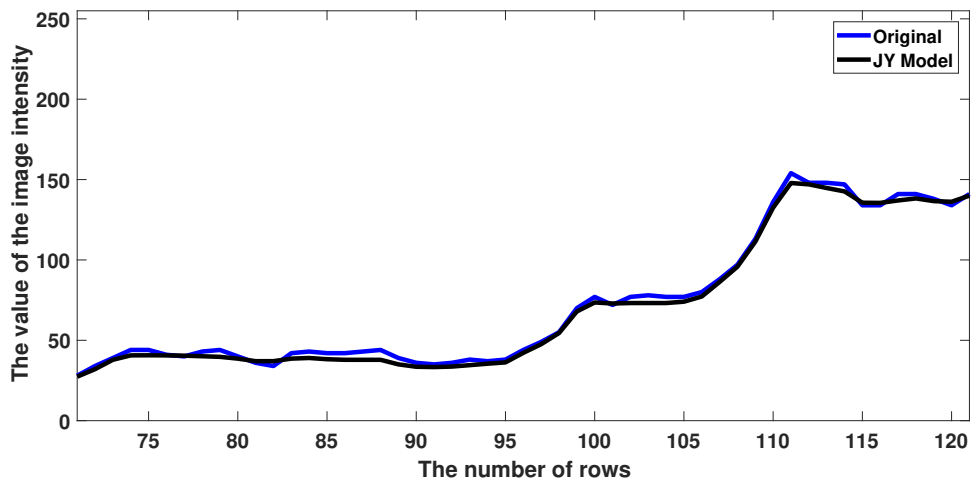


Figure 4.8: Corresponding signals of the 75th column with different rows ranging from 70 to 120, extracted from the baby image and the restored images by the JY model.

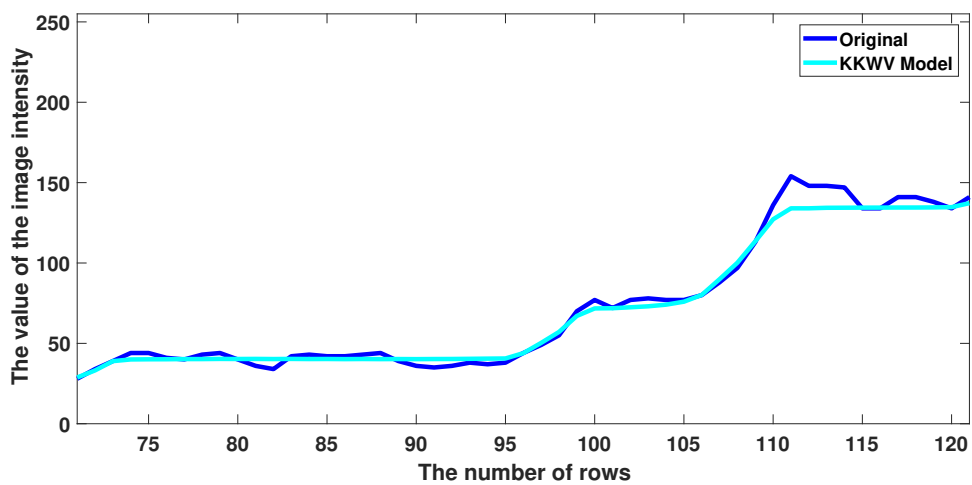


Figure 4.9: Corresponding signals of the 75th column with different rows ranging from 70 to 120, extracted from the baby image and the restored images by the KKWV model.

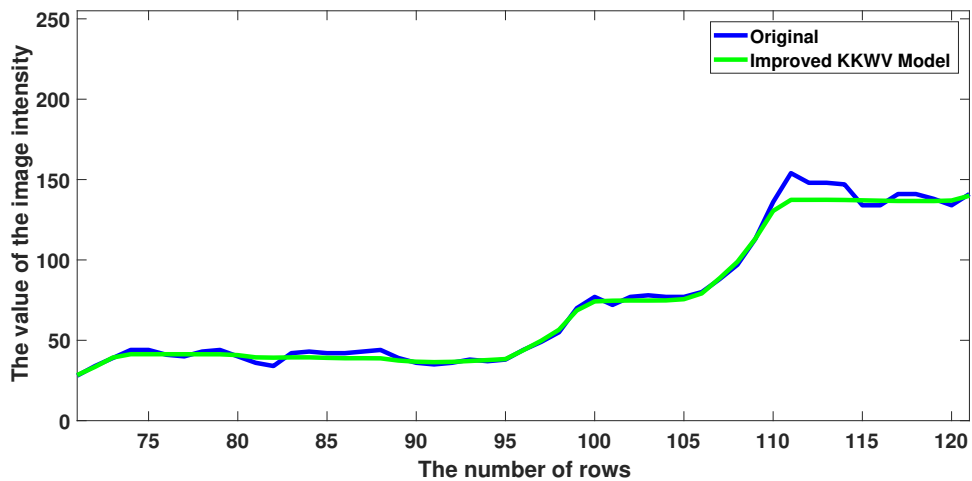


Figure 4.10: Corresponding signals of the 75th column with different rows ranging from 70 to 120, extracted from the baby image and the restored images by the improved KKWV model.

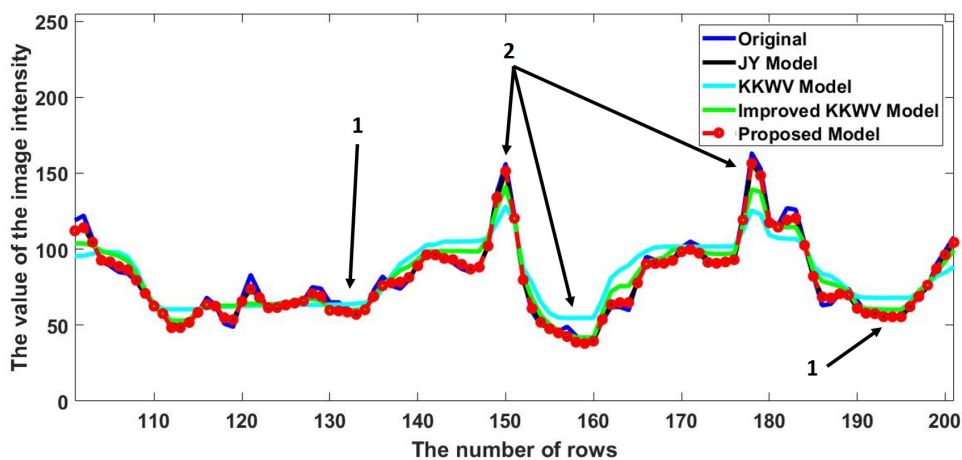


Figure 4.11: Corresponding signals of the 150th column with different rows ranging from 100 to 200, extracted from the baby image and the restored images by four noise removal models.

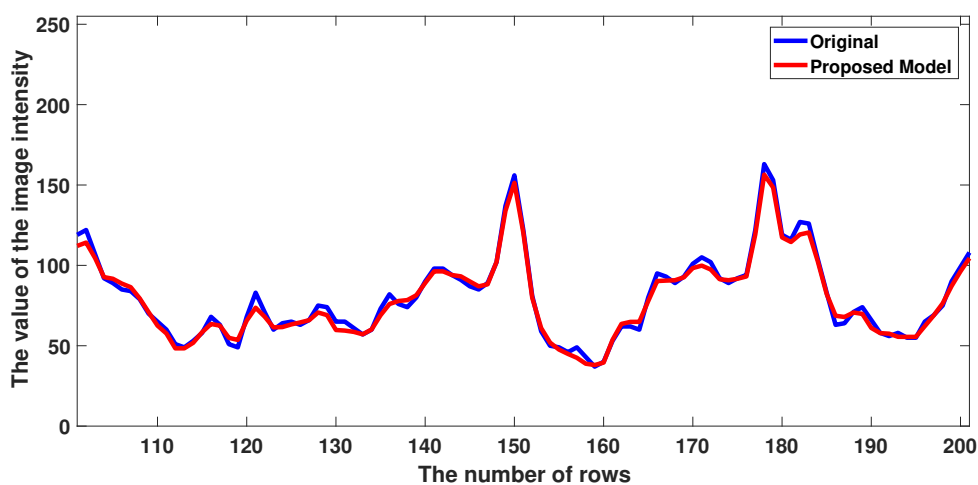


Figure 4.12: Corresponding signals of the 150th column with different rows ranging from 100 to 200, extracted from the baby image and the restored images by the proposed model.

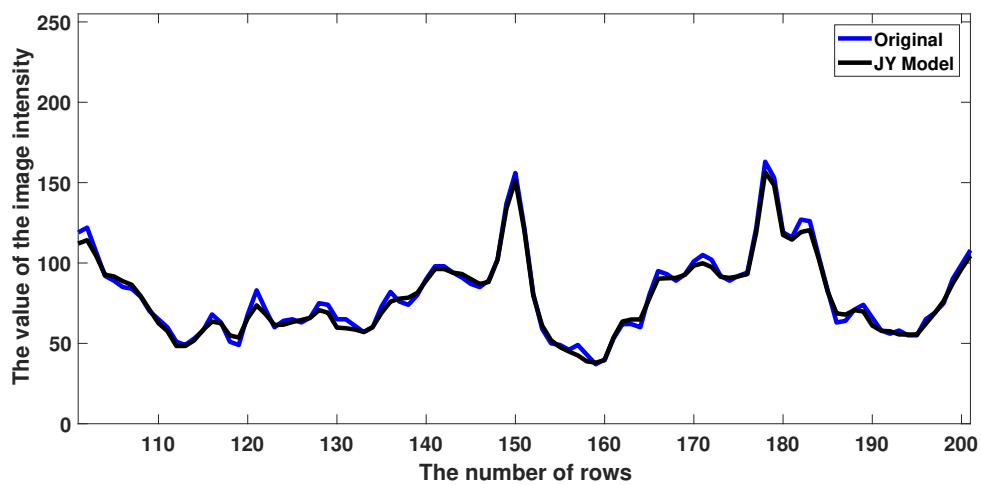


Figure 4.13: Corresponding signals of the 150th column with different rows ranging from 100 to 200, extracted from the kidney image and the restored images by the JY model.

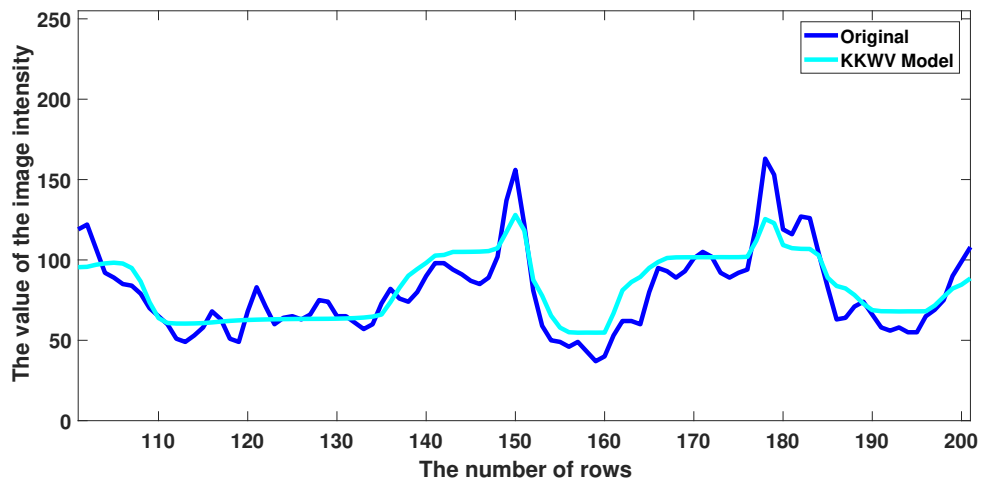


Figure 4.14: Corresponding signals of the 150th column with different rows ranging from 100 to 200, extracted from the kidney image and the restored images by the KKWV model.

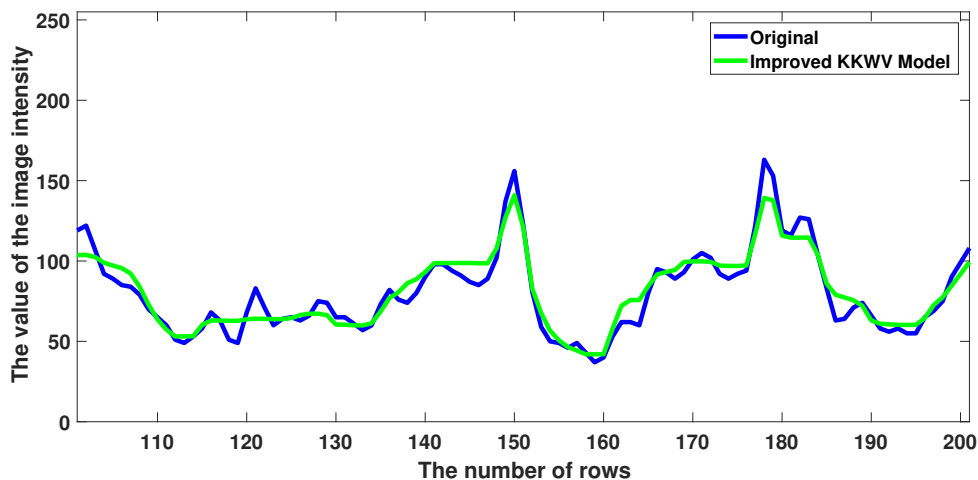


Figure 4.15: Corresponding signals of the 150th column with different rows ranging from 100 to 200, extracted from the kidney image and the restored images by the improved KKWV model.

## 4.5 Conclusions

In this chapter, we have firstly proposed a first-order variational model for the mixed noise reduction of real US images. In order to solve the proposed model, we have developed an efficient numerical algorithm based on the SB method. Our numerical results not only confirm that the proposed model is more accurate and robust in removing mixed noise from synthetic and real US images than existing noise removal models, but also that the proposed numerical algorithm is more effective than those by the other two standard methods.

# Chapter 5

## A Second-Order Model and Its Numerical Algorithm

As can be seen, the main difference among the variational models mentioned in the previous section for SN removal only comes from their data terms, while a common feature is to use  $\mathcal{R}^{\text{TV}}$  as the regularization term. As previously reviewed in Chapter 3,  $\mathcal{R}^{\text{TV}}$  used in these models for recovering sharp edges is confliction with SN removing because the noise is very large and signal dependent. That is to say the edges are blurred when noise is removed or edges are sharp but the noise is not well removed. In other words,  $\mathcal{R}^{\text{TV}}$  is not inadequate. In order to improve the restoration results of  $\mathcal{R}^{\text{TV}}$ , it motivates us to propose a second-order regularization based variational model in dealing with these effects from SN reduction process. To our knowledge, higher-order regularization approach has not been applied for SN reduction in real US images modeled by (4.1).

### 5.1 A New Second-Order Variational Model

Since TV based models always have the staircase effect due to the solutions consisting of piecewise constant function in BV space, in this thesis, we propose a new higher-order model based on the second-order TGV regularization to eliminate the combined ASN and MSN in real US images as follows:

$$\min_{u>0, u \in L^p(\Omega)} \{ \mathcal{J}_{\text{ASN-MSN}}^{\text{TGV}}(u) = \mathcal{D}_{\text{ASN-MSN}}^{\text{New}}(u) + \text{TGV}_{\alpha}^2(u) \}. \quad (5.1)$$

We note that  $p \leq 2$ ,

$$\mathcal{D}_{\text{ASN-MSN}}^{\text{New}}(u) = \gamma_1 \int_{\Omega} \frac{(u-z)^2}{u} d\Omega + \gamma_2 \int_{\Omega} (u + ze^{-u}) d\Omega,$$

and the second-order TGV regularization is defined as

$$\text{TGV}_{\alpha}^2(u) = \sup \left\{ \int_{\Omega} u \operatorname{div}^2 \mathbf{v} dx \mid \mathbf{v} \in \mathcal{C}^2(\Omega, \mathcal{S}^{2 \times 2}), \|\mathbf{v}\|_{\infty} \leq \alpha_2, \|\operatorname{div} \mathbf{v}\|_{\infty} \leq \alpha_1 \right\},$$

where  $\alpha_1, \alpha_2 > 0$ ,  $\mathcal{S}^{2 \times 2}$  is the set of all  $2 \times 2$  symmetric matrices, and  $\mathcal{C}^2(\Omega, \mathcal{S}^{2 \times 2})$  is the space of continuously differentiable symmetric matrix field with the compact support in  $\Omega$ . Here the infinity norm of  $\mathbf{v}$  and  $\operatorname{div} \mathbf{v}$  are defined as

$$\|\mathbf{v}\|_{\infty} = \sup_{x \in \Omega} \left( \sum_{i,j=1}^2 |\mathbf{v}_{i,j}|^2 \right)^{1/2},$$

$$\|\operatorname{div} \mathbf{v}\|_{\infty} = \sup_{x \in \Omega} \left( \sum_{i=1}^2 |(\operatorname{div} \mathbf{v})_i|^2 \right)^{1/2},$$

and the divergences are given by

$$(\operatorname{div} \mathbf{v})_i = \sum_{j=1}^2 \frac{\partial \mathbf{v}_{i,j}}{\partial x_j},$$

$$\operatorname{div}^2 \mathbf{v} = \sum_{i,j=1}^2 \frac{\partial^2 \mathbf{v}_{i,j}}{\partial x_i \partial x_j},$$

where  $1 \leq i \leq 2$ . We note that the kernel of  $\text{TGV}_{\alpha}^2(u)$  is defined as

$$\ker(\text{TGV}_{\alpha}^2(u)) = \{u : \Omega \rightarrow \mathbb{R} \mid u(x) = Ax + b \text{ a.e. in } \Omega \text{ for some } A \in \mathbb{R}^{1 \times 2}, b \in \mathbb{R}\}.$$

Then a linear mapping  $P$  is defined as a projection operator onto the kernel of  $\text{TGV}_{\alpha}^2(u)$ :

$$P : L^p(\Omega) \rightarrow \ker(\text{TGV}_{\alpha}^2(u)).$$

To prove the existence of solutions for (5.1), the following coercivity assumption on  $\mathcal{D}_{\text{ASN-MSN}}^{\text{New}}$  should be made: For any sequence  $\{u^n\}$  in  $L^p(\Omega)$ , it follows that

$$\|Pu^n\|_p \rightarrow \infty \text{ and } \left\{ \|(I - P)u^n\|_p \right\} \text{ bounded} \Rightarrow \mathcal{D}_{\text{ASN-MSN}}^{\text{New}} \rightarrow \infty. \quad (5.2)$$

If (5.2) is satisfied, there exists at least one solution for (5.1) [7].

### 5.1.1 Existence and Uniqueness of the Solution

**Theorem 5.1.** *For  $z \geq 0$  and  $z \in L^\infty(\Omega)$ , there exists a linear projection  $P$  such that  $\mathcal{D}_{ASN-MSN}^{\text{New}}$  satisfies the condition (5.2). Thus the proposed model (5.1) exists at least one minimizer.*

*Proof.* Let  $P : L^1(\Omega) \rightarrow \ker(\text{TGV}_\alpha^2(u))$  be an arbitrary linear continuous projection. If, for a sequence  $\{u^n\} \subset L^p(\Omega)$  it holds that  $\|Pu^n\|_p \rightarrow \infty$ , then also  $\|Pu^n\|_1 \rightarrow \infty$  since all norms are equivalent on the finite-dimensional space  $\ker(\text{TGV}_\alpha^2(u))$ . Then the following inequality holds as  $P$  is continuous on  $L^1(\Omega)$ ,

$$\begin{aligned} \mathcal{D}_{ASN-MSN}^{\text{New}}(u^n) &= \gamma_1 \int_{\Omega} \left( u^n + \frac{z^2}{u^n} - 2z \right) d\Omega + \gamma_2 \int_{\Omega} (u^n + ze^{-u^n}) d\Omega \\ &\geq \gamma_1 \int_{\Omega} (u^n - 2z) d\Omega + \gamma_2 \int_{\Omega} u^n d\Omega \\ &= (\gamma_1 + \gamma_2) \|u^n\|_1 - 2\gamma_1 \int_{\Omega} z d\Omega \\ &\geq c(\gamma_1 + \gamma_2) \|Pu^n\|_1 - 2\gamma_1 \int_{\Omega} z d\Omega \end{aligned}$$

for some constant  $c > 0$ . Accordingly,  $\mathcal{D}_{ASN-MSN}^{\text{New}}(u^n) \rightarrow \infty$  as  $n \rightarrow \infty$ , and therefore (5.2) is satisfied. Together with the fact that  $\mathcal{D}_{ASN-MSN}^{\text{New}}$  is proper, convex, and lower semi-continuous, this implies that the proposed model (5.1) admits at least one solution.  $\square$

**Theorem 5.2.** *Let  $z \in L^\infty(\Omega)$  with  $\inf_{\Omega} z > 0$ , then the proposed model (5.1) admits a unique solution.*

*Proof.* From now on, we write  $\mathcal{D}_{ASN-MSN}^{\text{New}}(u)$  as

$$\mathcal{D}_{ASN-MSN}^{\text{New}}(u) = \gamma_1 \int_{\Omega} h(u) d\Omega + \gamma_2 \int_{\Omega} g(u) d\Omega, \quad (5.3)$$

where

$$h(s) = \frac{(z-s)^2}{s} \text{ and } g(s) = s + ze^{-s}.$$

It is easy to find that  $h''(s) = \frac{2z^2}{s^3}$  and  $g''(s) = ze^{-s}$ . Thus  $h$  and  $g$  are strictly convex with respect to  $s$  as  $\inf_{\Omega} z > 0$ . Therefore,  $\mathcal{D}_{ASN-MSN}^{\text{New}}(u)$  is strictly convex for all  $\gamma_1, \gamma_2 > 0$ . With the convexity of the TGV regularization  $\text{TGV}_\alpha^2(u)$  [7] and strictly convexity of  $\mathcal{D}_{ASN-MSN}^{\text{New}}(u)$ , we obtain the conclusion that objective functional  $\mathcal{J}_{ASN-MSN}^{\text{TGV}}(u)$  in the proposed model (5.1) is strictly convex. Hence the uniqueness follows from the strict convexity of  $\mathcal{J}_{ASN-MSN}^{\text{TGV}}(u)$ .  $\square$



### 5.1.2 Split Bregman Method for the New Variational Model

By the Fenchel–Rockafellar duality, we have the dual form of  $\text{TGV}_\alpha^2(u)$  which can be rewritten as (see, for instance, [9, 10, 59])

$$\text{TGV}_\alpha^2(u) = \min_{\mathbf{p} \in \mathcal{C}^2(\Omega, \mathcal{S}^{2 \times 2})} \left\{ \alpha_1 \int_{\Omega} |\nabla u - \mathbf{p}| \, d\Omega + \alpha_2 \int_{\Omega} |\epsilon(\mathbf{p})| \right\} \quad (5.4)$$

where

$$\epsilon(\mathbf{p}) = \begin{pmatrix} p_{1x} & \frac{p_{1y} + p_{2x}}{2} \\ \frac{p_{1y} + p_{2x}}{2} & p_{2y} \end{pmatrix}.$$

The SB method can be easily applied to solve the proposed second-order variational model (5.1). Here, we use the auxiliary variables  $(\mathbf{w}, \mathbf{v}; \mathbf{b}, \mathbf{d})$  and positive penalty parameter  $(\theta_1, \theta_2)$ . We reformulate the original model (5.1) as the equivalent unconstrained minimization problem as given by

$$\begin{aligned} \min_{u, \mathbf{p}, \mathbf{w}, \mathbf{v}} \left\{ \bar{\mathcal{J}}_{\text{ASN-MSN}}^{\text{TGV}}(u, \mathbf{p}, \mathbf{w}, \mathbf{v}; \mathbf{b}, \mathbf{d}) = \mathcal{D}_{\text{ASN-MSN}}^{\text{New}}(u, z) \right. \\ \left. + \alpha_1 \int_{\Omega} |\mathbf{w}| \, d\Omega + \frac{\theta_1}{2} \int_{\Omega} (\mathbf{w} - \nabla u + \mathbf{p} - \mathbf{b})^2 \, d\Omega \right. \\ \left. + \alpha_2 \int_{\Omega} |\mathbf{v}| \, d\Omega + \frac{\theta_2}{2} \int_{\Omega} (\mathbf{v} - \epsilon(\mathbf{p}) - \mathbf{d})^2 \, d\Omega \right\}. \end{aligned} \quad (5.5)$$

Recall that the meaning of the primal and dual variables in (5.5) are listed as the following

- $u$  denotes the denoised image to be recovered;
- $\mathbf{p} = (p_1 \ p_2)$  is the symmetrized gradient;
- $\mathbf{w} = (w_1 \ w_2)$  is a vector valued function related to vector field  $\nabla u - \mathbf{p}$ ;
- $\mathbf{v} = \begin{pmatrix} v_{11} & v_3 \\ v_3 & v_{22} \end{pmatrix}$  is a matrix valued function related to symmetrized gradient  $\epsilon(\mathbf{p})$ ;
- $\mathbf{b} = (b_1 \ b_2)$  denotes a vector Bregman iterative parameter for enforcing  $\mathbf{w} = \nabla u - \mathbf{p}$ ;

- $\mathbf{d} = \begin{pmatrix} d_{11} & d_3 \\ d_3 & d_{22} \end{pmatrix}$  denotes a matrix Bregman iterative parameter for enforcing  $\mathbf{v} = \epsilon(\mathbf{p})$ .

The primal-dual algorithm for solving the minimization problem (5.5) is expressed as the following iterations:

$$u^{[\text{new}]} = \arg \min_u \left\{ \mathcal{D}_{\text{ASN-MSN}}^{\text{New}}(u, z) + \frac{\theta_1}{2} \int_{\Omega} (\mathbf{w}^{[\text{old}]} - \nabla u + \mathbf{p}^{[\text{old}]} - \mathbf{b}^{[\text{old}]})^2 d\Omega \right\}, \quad (5.6)$$

$$\begin{aligned} \mathbf{p}^{[\text{new}]} = \arg \min_{\mathbf{p}} \left\{ \frac{\theta_1}{2} \int_{\Omega} (\mathbf{w}^{[\text{old}]} - \nabla u^{[\text{new}]} + \mathbf{p} - \mathbf{b}^{[\text{old}]})^2 d\Omega \right. \\ \left. + \frac{\theta_2}{2} \int_{\Omega} (\mathbf{v}^{[\text{old}]} - \epsilon(\mathbf{p}) - \mathbf{d}^{[\text{old}]})^2 d\Omega \right\}, \end{aligned} \quad (5.7)$$

$$\mathbf{w}^{[\text{new}]} = \arg \min_{\mathbf{w}} \left\{ \alpha_1 \int_{\Omega} |\mathbf{w}| d\Omega + \frac{\theta_1}{2} \int_{\Omega} (\mathbf{w} - \nabla u^{[\text{new}]} + \mathbf{p}^{[\text{new}]} - \mathbf{b}^{[\text{old}]})^2 d\Omega \right\}, \quad (5.8)$$

$$\mathbf{v}^{[\text{new}]} = \arg \min_{\mathbf{v}} \left\{ \alpha_2 \int_{\Omega} |\mathbf{v}| d\Omega + \frac{\theta_2}{2} \int_{\Omega} (\mathbf{v} - \epsilon(\mathbf{p}^{[\text{new}]})) - \mathbf{d}^{[\text{old}]} \right\}^2 d\Omega \right\}, \quad (5.9)$$

$$\mathbf{b}^{[\text{new}]} = \mathbf{b}^{[\text{old}]} + \nabla u^{[\text{new}]} - \mathbf{p}^{[\text{new}]} - \mathbf{w}^{[\text{new}]}, \quad (5.10)$$

$$\mathbf{d}^{[\text{new}]} = \mathbf{d}^{[\text{old}]} + \epsilon(\mathbf{p}^{[\text{new}]}) - \mathbf{v}^{[\text{new}]}. \quad (5.11)$$

The solutions for  $u$ -,  $\mathbf{p}$ -,  $\mathbf{w}$ - and  $\mathbf{v}$ -subproblems can be derived as the following.

**$u$ -subproblem.** Fixing variables  $(\mathbf{p}, \mathbf{w}; \mathbf{b})$  in (5.6) leads to the Euler-Lagrange equation associated with  $u$  as given by

$$-\theta_1 \Delta u = \bar{G}(u) \quad (5.12)$$

where  $\bar{G}(u) = \gamma_1(\frac{z^2}{u^2} - 1) + \gamma_2(ze^{-u} - 1) - \theta_1 \text{div}(\mathbf{w} + \mathbf{p} - \mathbf{b})$ . To solve the nonlinear PDE (5.12), we firstly apply the fixed point method as follows:

$$\gamma_3 u^{[\nu+1]} - \theta_1 \Delta u^{[\nu+1]} = G(u^{[\nu]}) \quad (5.13)$$

where  $G(u^{[\nu]}) = \bar{G}(u^{[\nu]}) + \gamma_3 u^{[\nu]}$  and  $\gamma_3 > 0$ . Secondly, we assume that  $\Omega = [1, M] \times [1, N]$  and  $\bar{\Omega} \subset \Omega$  is the discretized image domain where

$$\bar{\Omega} = \{(x, y) = (x_i, y_j) \in \Omega, x_i = i, y_j = j\}$$

with  $1 \leq i \leq M$  and  $1 \leq j \leq N$ . Next, we discretize the linearized PDE (5.13) using the standard finite difference method subject to periodic boundary conditions.

Thus, the DFT method can be directly applied as follows:

$$\mathcal{F}\{\gamma_3(u^{[\nu+1]})_{i,j} - \theta_1(\Delta u^{[\nu+1]})_{i,j}\} = \mathcal{F}\{G(u^{[\nu]})_{i,j}\}. \quad (5.14)$$

where  $\mathcal{F}$  denoted the DFT operator. For the discrete frequencies  $r \in [0, M)$  and  $s \in [0, N)$ , we have

$$\zeta_1 \mathcal{F}\{(u^{[\nu+1]})_{i,j}\} = \mathcal{F}\{(G(u^{[\nu]}))_{i,j}\}. \quad (5.15)$$

where  $\zeta_1 = \gamma_3 - 2\theta_1 \left( \cos\left(\frac{2\pi s}{N}\right) + \cos\left(\frac{2\pi r}{M}\right) - 2 \right)$ ,  $i \in [1, M]$  and  $j \in [1, N]$  are the indexes in the discrete time domain. For each outer step  $\nu$ , we finally have a closed-form solution of  $u^{[\nu+1]}$  at grid point  $(i, j)$

$$(u^{[\nu+1]})_{i,j} = \text{Re} \left( \mathcal{F}^{-1} \left( \frac{\mathcal{F}((G(u^{[\nu]}))_{i,j})}{\zeta_1} \right) \right), \quad (5.16)$$

where  $\mathcal{F}^{-1}$  denotes the inverse DFT operator.  $\text{Re}$  is the real part of a complex number. ‘—’ represents for point-wise division of matrices.

**p-subproblem.** By fixing variables  $(u, \mathbf{w}, \mathbf{v}; \mathbf{b}, \mathbf{d})$  in (5.7), the Euler-Lagrange equation associated with  $\mathbf{p} = (p_1 \ p_2)$  as given by

$$(\theta_1 - \theta_2 \partial_x^+ \partial_x^- - \frac{\theta_2}{2} \partial_y^+ \partial_y^-)(p_1)_{i,j} - \frac{\theta_2}{2} \partial_y^+ \partial_x^- (p_2)_{i,j} = (h_1)_{i,j}, \quad (5.17)$$

$$(\theta_1 - \frac{\theta_2}{2} \partial_x^+ \partial_x^- - \theta_2 \partial_y^+ \partial_y^-)(p_2)_{i,j} - \frac{\theta_2}{2} \partial_x^+ \partial_y^- (p_1)_{i,j} = (h_2)_{i,j}, \quad (5.18)$$

where

$$(h_1)_{i,j} = \theta_1(\partial_x^+ u + b_1 - w_1)_{i,j} - \theta_2 \partial_x^+(v_{11} - d_{11})_{i,j} - \theta_2 \partial_y^+(v_3 - d_3)_{i,j}, \quad (5.19)$$

$$(h_2)_{i,j} = \theta_1(\partial_y^+ u + b_2 - w_2)_{i,j} - \theta_2 \partial_y^+(v_{22} - d_{22})_{i,j} - \theta_2 \partial_x^+(v_3 - d_3)_{i,j}. \quad (5.20)$$

Taking the DFT with (5.17) and (5.18) leads to the following system of linear equations

$$\begin{pmatrix} a_{11} & a_{12} \\ a_{21} & a_{22} \end{pmatrix} \begin{pmatrix} \mathcal{F}\{(p_1)_{i,j}\} \\ \mathcal{F}\{(p_2)_{i,j}\} \end{pmatrix} = \begin{pmatrix} \mathcal{F}\{(h_1)_{i,j}\} \\ \mathcal{F}\{(h_2)_{i,j}\} \end{pmatrix},$$

where

$$\begin{aligned} a_{11} &= \theta_1 - \theta_2 \left( 2 \cos \frac{2\pi s}{N} - 2 \right) - \frac{\theta_2}{2} \left( 2 \cos \frac{2\pi r}{M} - 2 \right), \\ a_{12} &= -\frac{\theta_2}{2} \left( -1 + \cos \frac{2\pi r}{M} + \sqrt{-1} \sin \frac{2\pi r}{M} \right) \cdot \left( 1 - \cos \frac{2\pi s}{N} + \sqrt{-1} \sin \frac{2\pi s}{N} \right), \\ a_{21} &= -\frac{\theta_2}{2} \left( -1 + \cos \frac{2\pi s}{N} + \sqrt{-1} \sin \frac{2\pi s}{N} \right) \cdot \left( 1 - \cos \frac{2\pi r}{M} + \sqrt{-1} \sin \frac{2\pi r}{M} \right), \\ a_{22} &= \theta_1 - \frac{\theta_2}{2} \left( 2 \cos \frac{2\pi s}{N} - 2 \right) - \theta_2 \left( 2 \cos \frac{2\pi r}{M} - 2 \right). \end{aligned}$$

The coefficient matrix  $\begin{pmatrix} a_{11} & a_{12} \\ a_{21} & a_{22} \end{pmatrix}$  is a  $M \times N$  numbers of  $2 \times 2$ , whose determinant is

$$D = \left( \theta_1 - 2\theta_2 \left( \cos \frac{2\pi s}{N} + \cos \frac{2\pi r}{M} - 2 \right) \right) \cdot \left( \theta_1 - \theta_2 \left( \cos \frac{2\pi s}{N} + \cos \frac{2\pi r}{M} - 2 \right) \right), \quad (5.21)$$

which always positive for all discrete frequencies if  $(\theta_1, \theta_2) > 0$ . Thus, the closed-form solution of  $p_1$  and  $p_2$  at a grid point  $(i, j)$  are given by

$$(p_1)_{i,j} = \operatorname{Re} \left( \mathcal{F}^{-1} \left\{ \frac{a_{22} \mathcal{F} \{ (h_1)_{i,j} \} - a_{12} \mathcal{F} \{ (h_2)_{i,j} \}}{D} \right\} \right), \quad (5.22)$$

$$(p_2)_{i,j} = \operatorname{Re} \left( \mathcal{F}^{-1} \left\{ \frac{a_{11} \mathcal{F} \{ (h_2)_{i,j} \} - a_{21} \mathcal{F} \{ (h_1)_{i,j} \}}{D} \right\} \right). \quad (5.23)$$

**w-subproblem.** By fixing variables  $(u, \mathbf{p}, \mathbf{v}; \mathbf{b}, \mathbf{d})$  in (5.8), the closed-form solution of  $\mathbf{w}$  at a grid point  $(i, j)$  is given by

$$(\mathbf{w})_{i,j} = \max \left( |\nabla(u)_{i,j} - (\mathbf{p})_{i,j} + (\mathbf{b})_{i,j}| - \frac{\alpha_1}{\theta_1}, 0 \right) \cdot \frac{\nabla(u)_{i,j} - (\mathbf{p})_{i,j} + (\mathbf{b})_{i,j}}{|\nabla(u)_{i,j} - (\mathbf{p})_{i,j} + (\mathbf{b})_{i,j}|}. \quad (5.24)$$

**v-subproblem.** By fixing variables  $(\mathbf{p}; \mathbf{d})$  in (5.9), the closed-form solution of  $\mathbf{v}$  at a grid point  $(i, j)$  is given by

$$(\mathbf{v})_{i,j} = \max \left( |\epsilon((\mathbf{p})_{i,j}) + (\mathbf{d})_{i,j}| - \frac{\alpha_2}{\theta_2}, 0 \right) \frac{\epsilon((\mathbf{p})_{i,j}) + (\mathbf{d})_{i,j}}{|\epsilon((\mathbf{p})_{i,j}) + (\mathbf{d})_{i,j}|}. \quad (5.25)$$

Finally, the proposed method for the second-order model (5.5) can be presented in Algorithm 5.

### Algorithm 5 : Split Bregman Algorithm for the Proposed Second-Order Variational Model

Denote by

- $u$  the denoised image
- $z$  the noisy image
- $\gamma_1, \gamma_2$  the regularization parameters
- $\alpha_1, \alpha_2$  the regularization parameters
- $\mathbf{p}$  the symmetrized gradient
- $\mathbf{w}$  the auxiliary spitting vector variable
- $\mathbf{v}$  the auxiliary spitting matrix variable
- $\mathbf{b}, \mathbf{d}$  the Bregman iterative parameters
- $\theta_1, \theta_2$  the penalty parameters

$$[u] \leftarrow \text{SBTGV}(u, z, \gamma_1, \gamma_2, \alpha_1, \alpha_2, \mathbf{p}, \mathbf{w}, \mathbf{v}, \mathbf{b}, \mathbf{d}, \theta_1, \theta_2)$$

- 
- Step 1. Initialization : Set  $u = z, m = 0$  and  $(\mathbf{p}^{(m)}, \mathbf{w}^{(m)}, \mathbf{v}^{(m)}; \mathbf{b}^{(m)}, \mathbf{d}^{(m)}) = \mathbf{0}$ , and choose  $\gamma_1, \gamma_2, \alpha_1, \alpha_2 > 0, \theta_1, \theta_2 > 0$ ;
  - Step 2. Compute  $u^{(m+1)}$  according to (5.16) for fixed  $(\mathbf{p}^{(m)}, \mathbf{w}^{(m)}; \mathbf{b}^{(m)})$ ;
  - Step 3. Compute  $\mathbf{p}^{(m+1)}$  according to (5.22) and (5.23) for fixed  $(u^{(m+1)}, \mathbf{w}^{(m)}, \mathbf{v}^{(m)}; \mathbf{b}^{(m)}; \mathbf{d}^{(m)})$ ;
  - Step 4. Compute  $\mathbf{w}^{(m+1)}$  according to (5.24) for fixed  $(u^{(m+1)}, \mathbf{p}^{(m+1)}, \mathbf{v}^{(m)}; \mathbf{b}^{(m)}; \mathbf{d}^{(m)})$ ;
  - Step 5. Compute  $\mathbf{v}^{(m+1)}$  according to (5.25) for fixed  $(\mathbf{p}^{(m+1)}; \mathbf{d}^{(m)})$ ;
  - Step 6. Update  $\mathbf{b}^{(m+1)}$  according to (5.10);
  - Step 7. Update  $\mathbf{d}^{(m+1)}$  according to (5.11);
  - Step 8. If a stopping criterion is satisfied, stop; else  $m \leftarrow m + 1$ , repeat 2.
- 

## 5.2 Numerical Results and Discussion

Our aim in this section is to show that the proposed second-order variational model is more accurate and reliable than existing variational models for removing noise from both synthetic and real US images. To compare the performance of existing

higher-order variational models with the proposed second-order model, we apply the SB methods for all models.

There are 5 variational models in experiment. For simplicity, we name these variational models as follows:

- $\min_{u>0} \{ \mathcal{J}_{\text{ASN-MSN}}^{\text{TV}}(u) = \mathcal{D}_{\text{ASN-MSN}}^{\text{New}}(u) + \mathcal{R}^{\text{TV}}(u) \}$  called SN-TV model,
- $\min_{u>0} \{ \mathcal{J}_{\text{ASN-MSN}}^{\text{TL}}(u) = \mathcal{D}_{\text{ASN-MSN}}^{\text{New}}(u) + \mathcal{R}^{\text{TL}}(u) \}$  called SN-TL model,
- $\min_{u>0} \{ \mathcal{J}_{\text{ASN-MSN}}^{\text{BH}}(u) = \mathcal{D}_{\text{ASN-MSN}}^{\text{New}}(u) + \mathcal{R}^{\text{BH}}(u) \}$  called SN-BH model,
- $\min_{u>0} \{ \mathcal{J}_{\text{ASN-MSN}}^{\text{TC}}(u) = \mathcal{D}_{\text{ASN-MSN}}^{\text{New}}(u) + \mathcal{R}^{\text{Cv}}(u) \}$  called SN-TC model,
- $\min_{u>0} \{ \mathcal{J}_{\text{ASN-MSN}}^{\text{TGV}}(u) = \mathcal{D}_{\text{ASN-MSN}}^{\text{New}}(u) + \text{TGV}_{\alpha}^2(u) \}$  called SN-TGV model.

We note first that all experiments were performed using MATLAB R2019a on a machine with Intel Core i5 at 2.3GHz with 8 GB of RAM. Second, the peak signal to noise ratio (PSNR) between the original and restored images is used to measure the quality of image restoration results; a higher PSNR value indicates the higher quality of the restored image (better). The PSNR is defined as follows:

$$\text{PSNR} = 10 \log \left( \frac{255^2}{\text{MSE}} \right),$$

where  $\text{MSE} = \frac{1}{NM} \sum_{i=1}^M \sum_{j=1}^N ((u^*)_{i,j} - (u)_{i,j})^2$ . Here  $u$  and  $u^*$  are the original image and the restored image, respectively. Note that all numerical methods for each model will be repeated until the following stopping criteria based on the relative error of the solution is satisfied

$$\frac{\| u^{[\text{new}]} - u^{[\text{old}]} \|_{l^2}^2}{\| u^{[\text{old}]} \|_{l^2}^2} < 10^{-5}. \quad (5.26)$$

## Results on synthetic images

Figure 5.1 shows the original test images to be used here for the performance test of different models. The size of the three images are all the same which is  $256 \times 256$  pixels.

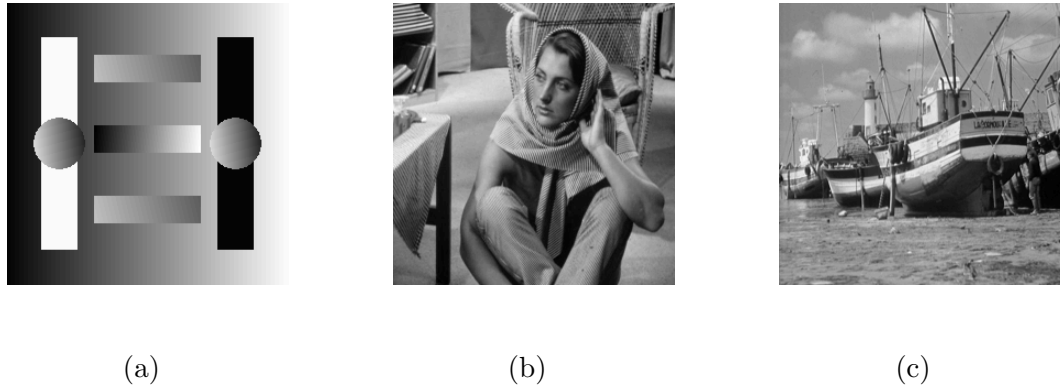


Figure 5.1: The original test images.

In order to test the performance of the variational models in dealing with staircase effect, we consider the linear-preservation abilities of different variational models on a piecewise linear image.

Figures 5.2 - 5.4 show the linear-preservation abilities of different variational models on a piecewise linear image as shown in Figure 5.1 (a).

In terms of visual inspection from Figure 5.3, the image (b)-(c) shows the results of the first-order SN-TV model are composed of jagged appearance, which is staircase effect. In addition, the restoration results shown from the images (d)-(f) illustrate the SN-BH, the SN-TC and the proposed SN-TGV models can remove the staircase effect.

As shown in Table 5.1 we see that the proposed SN-TGV model is the best model for the linear-preservation ability.

Model	PSNR
SN-TV Model	32.8007
SN-TL Model	30.4729
SN-BH Model	30.8700
SN-TC Model	34.6507
SN-TGV Model	<b>35.4040</b>

Table 5.1: Comparison of PSNR by different variational models on synthetic image.

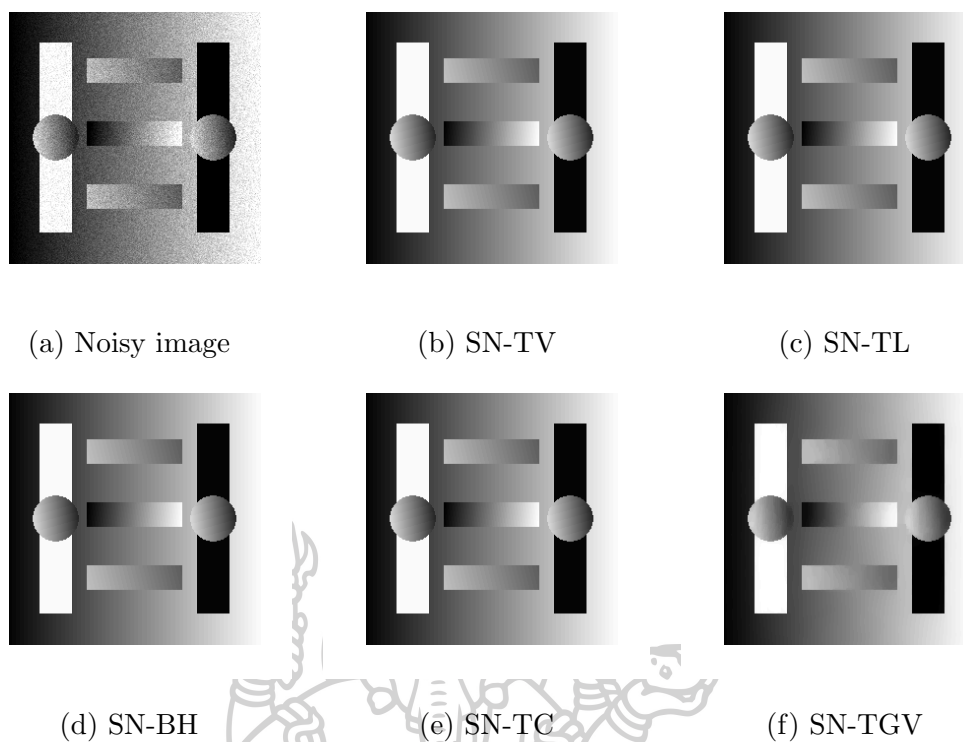


Figure 5.2: Linear-preservation ability test; (a) noisy image; (b)-(f) restoration results by SN-TV, SN-TL, SN-BH, SN-TC and SN-TGV models respectively.



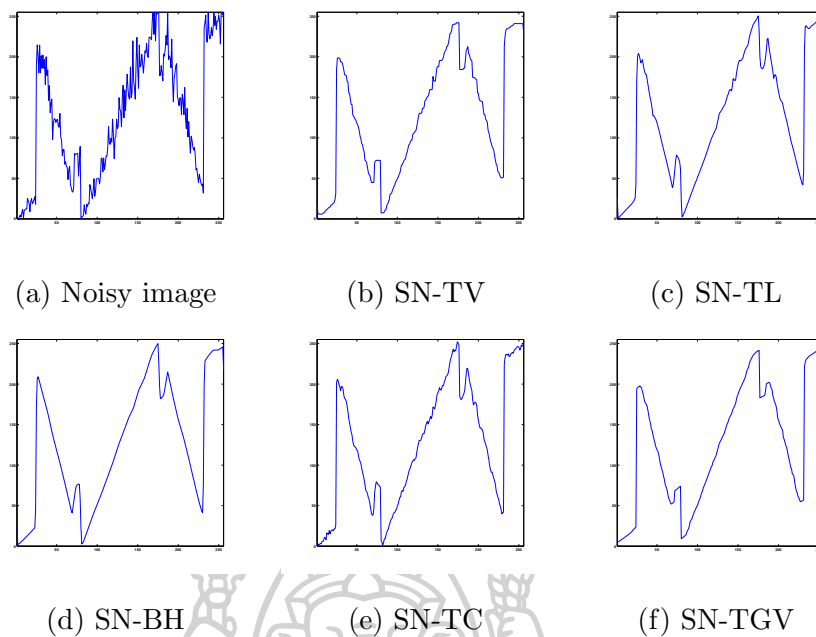


Figure 5.3: Plots of 1D of the noisy and denoised images in Figure 5.2, where the x-axis presents the number of columns and the y-axis shows the value of the image intensity.

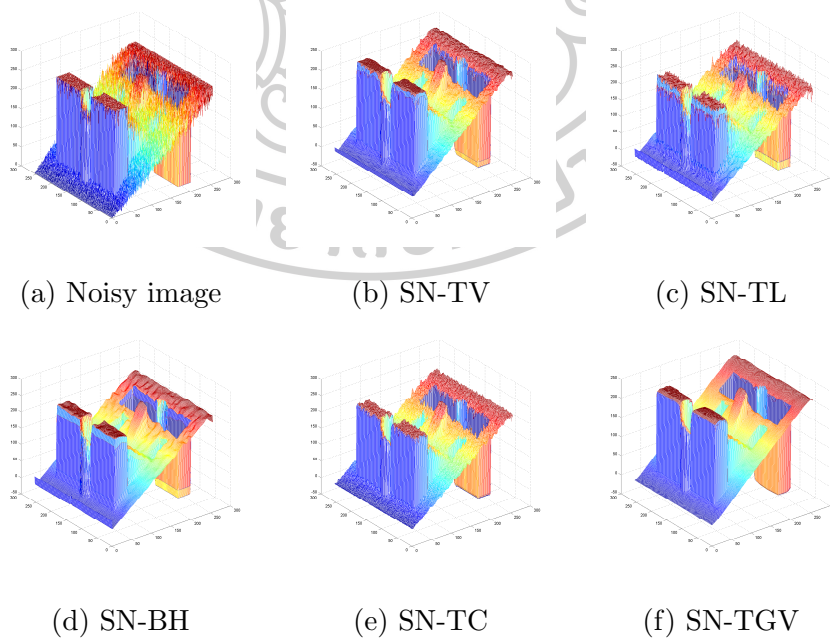


Figure 5.4: Surfaces of the noisy and denoised images in Figure 5.2.

Next, we test the performance of existing second-order variational models with the proposed second-order variational model on two noisy images, which are the “Boat” image and “Barbara” image. In Figure 5.1 (b)-(c), the noise formation model in (4.1) was used for creating the noisy versions of the original images Figure 5.1. In experiments, there are two case to considered. First, we test on different levels for Gamma noise  $(\frac{1}{10}, \frac{1}{50}, \frac{1}{100})$  by fixing  $k_0 = 0.5$ . Second, we test on different levels for Gaussian noise  $(0.5, 0.75, 1.25)$  by fixing  $k_1 = \frac{1}{100}$ . Tables 5.2 and 5.3 show the restoration results for the first and second cases, respectively.

Image	Model	$(k_0, k_1)$		
		$(0.5, \frac{1}{10})$	$(0.5, \frac{1}{50})$	$(0.5, \frac{1}{100})$
Barbara	SN-TV	27.3137	33.1470	34.3224
	SN-TL	27.2104	33.7238	34.4954
	SN-BH	27.7852	34.3320	35.2134
	SN-TC	28.0437	34.4047	35.1072
	SN-TGV	<b>28.3770</b>	<b>34.7061</b>	<b>35.6537</b>
Boat	SN-TV	26.9434	33.1043	34.0371
	SN-TL	26.7045	33.7157	34.6086
	SN-BH	27.4703	34.2175	35.2666
	SN-TC	27.8417	33.5479	35.3654
	SN-TGV	<b>28.4870</b>	<b>34.6713</b>	<b>35.8587</b>

Table 5.2: Comparison of PSNR testing on different levels of Gamma noise by different variational models on two images.

Image	Model	$(k_0, k_1)$		
		$(0.5, \frac{1}{100})$	$(0.75, \frac{1}{100})$	$(1.25, \frac{1}{100})$
Barbara	SN-TV	34.3224	32.6780	30.1405
	SN-TL	34.4954	32.3755	29.7882
	SN-BH	35.2134	32.6813	29.9819
	SN-TC	35.1072	<b>32.9776</b>	30.0458
	SN-TGV	<b>35.6537</b>	32.7008	<b>30.7949</b>
Boat	SN-TV	34.0371	32.8264	30.0651
	SN-TL	34.6086	32.4048	29.8085
	SN-BH	35.2666	32.8117	29.1545
	SN-TC	35.3654	33.1903	30.0377
	SN-TGV	<b>35.8587</b>	<b>33.4747</b>	<b>30.7719</b>

Table 5.3: Comparison of PSNR testing on different levels of Gaussian noise by different variational models on real images.

As can be seen from Table 5.2-5.3, the average PSNR of the restored images by the proposed second-order variational model is more accurate and robust than other four noise removal models for different level of noise strength.

### Results on real US images

In this section, we test the performance of the proposed second-order variational model and compared with other four models using two real US images, “baby” and “kidney”. These real US images from different medical applications are the same size which is  $256 \times 256$  pixels and corrupted with unknown SN strength.

Figure 5.5 and Figure 5.7 show the real US images of the baby and the kidney with SN and the restored image by the SN-TV, SN-TL, SN-BH, SN-TC and SN-TGV models. Figure 5.6 show the enlarged portions of the baby image and the restored image of the baby image by the SN-TV, SN-TL, SN-BH, SN-TC and SN-TGV models. Figure 5.8 show the enlarged portions of the kidney and the restored image of the baby image by the SN-TV, SN-TL, SN-BH, SN-TC and SN-TGV

models. Figure 5.9 show corresponding signals of the 75th column with different rows ranging from 70 to 120, extracted from the baby image and the restored images by five noise removal models. Figure 5.10 show corresponding signals of the 150th column with different rows ranging from 100 to 200, extracted from the kidney image and the restored images by five noise removal models.

It can be observed from Figure 5.5-5.8 that all models can be used to remove SN from real US images. Figure 5.9 and Figure 5.10 show that our model is more effective than other four models.

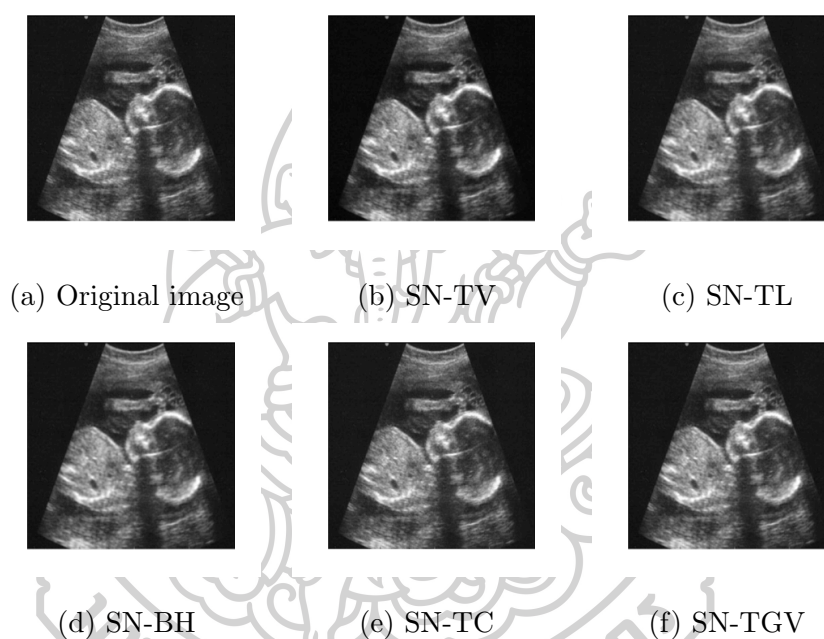


Figure 5.5: Performance comparison of different noise removal models on the baby image; (a) original image; (b)-(f) restored images.

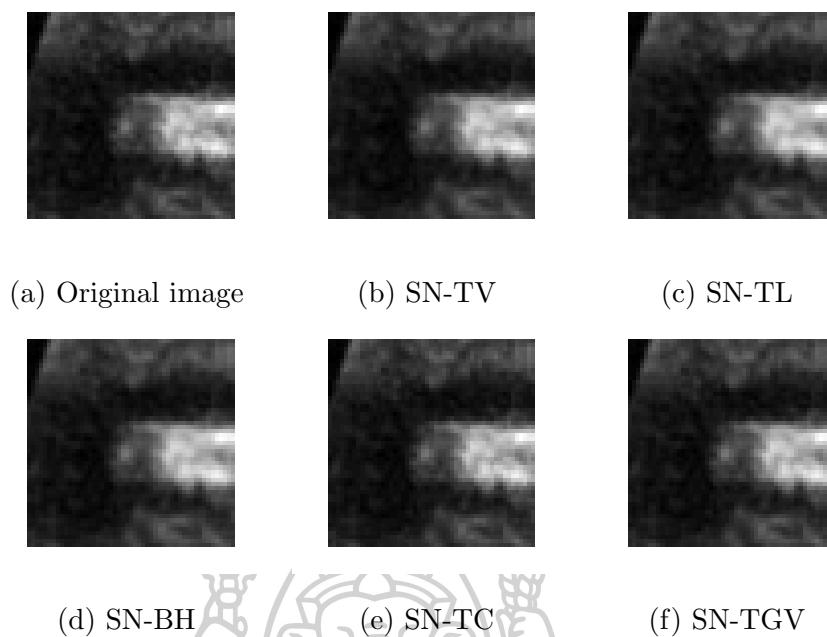


Figure 5.6: Performance comparison of different noise removal models on the baby image; (a) magnification of original image; (b)-(f) magnification of restored images.

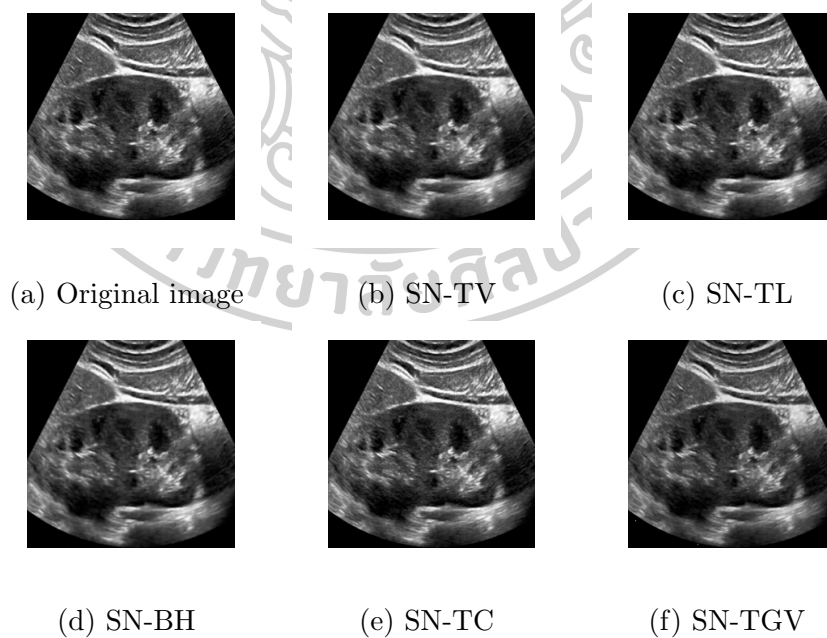


Figure 5.7: Performance comparison of different noise removal models on the kidney image; (a) original image; (b)-(f) restored images.

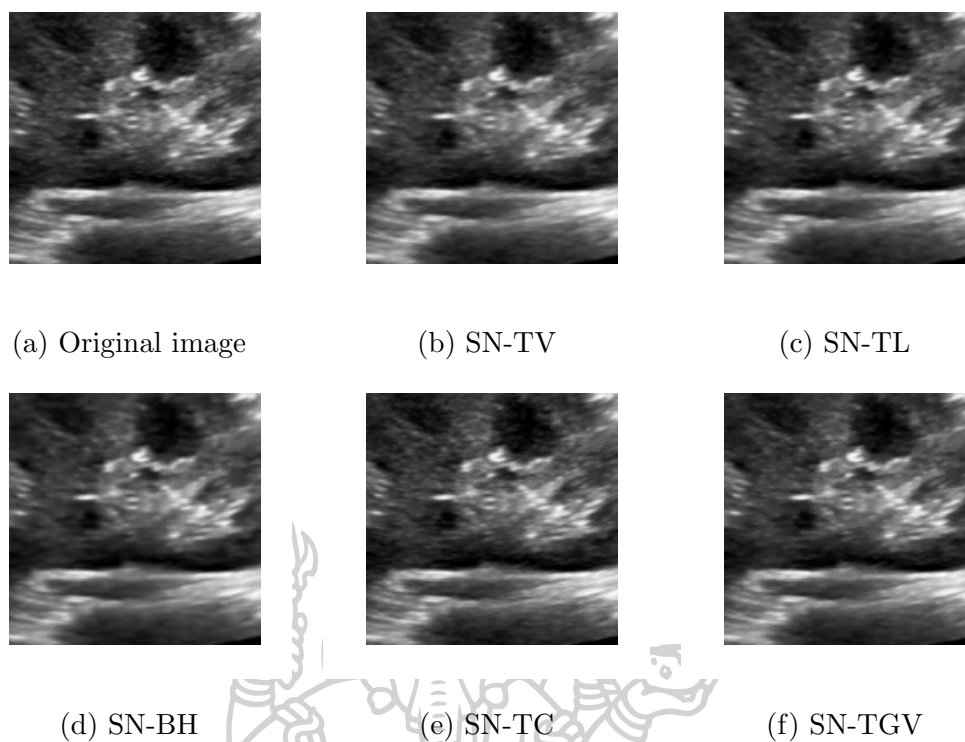


Figure 5.8: Performance comparison of different noise removal models on the kidney image; (a) magnification of original image; (b)-(f) magnification of restored images.

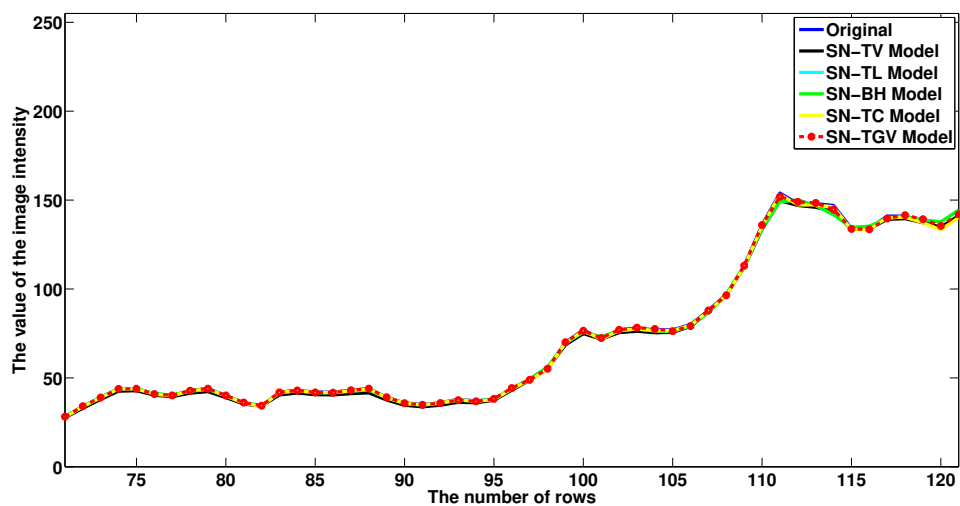


Figure 5.9: Corresponding signals of the 75th column with different rows ranging from 70 to 120, extracted from the baby image and the restored images by five noise removal models.

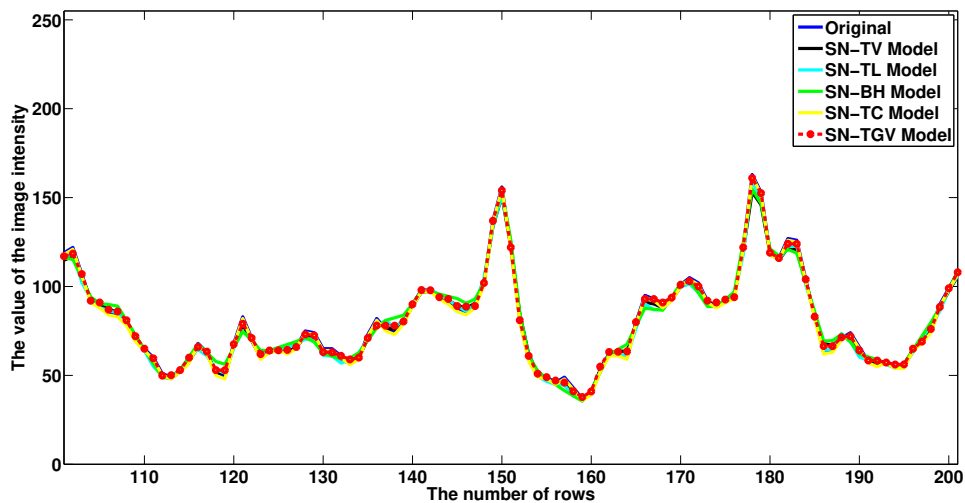


Figure 5.10: Corresponding signals of the 150th column with different rows ranging from 100 to 200, extracted from the kidney image and the restored images by five noise removal models.

### 5.3 Conclusions

In this Chapter, we presented a new second-order variational models for removing mixed noise from real US images to deal with the staircase effect. In order to solve the associated variational problem, we proposed the efficient numerical algorithm based on the SB framework. Our numerical tests confirm that the proposed second-order variational models deliver more accurate and reliable restoration results than the competing models.

## Chapter 6

# Summary and Future Directions

In this work, we have firstly proposed a first-order variational model for both ASN and MSN noise reduction of real US images. We have also discussed the existence and uniqueness of the solution for the proposed first-order variational model. In order to solve the proposed first-order variational model, we have developed three efficient numerical algorithm:

1. Method 1-explicit time marching method;
2. Method 2-fixed-point iteration method;
3. Method 3-split Bregman method.

Numerical tests confirmed that the proposed first-order model delivers better restoration results than those in [21, 35, 40] and the proposed algorithm based on SB method is more accurate than the standard numerical algorithms in delivering visually pleasing restoration results.

In order to improve the restoration results, we also proposed a second-order variational model and discussed the existence and uniqueness of the solution for the proposed second-order variational model. In order to solve the second-order variational model, we develop the numerical algorithm base on SB method. Numerical tests show that the proposed second-order variational model has several advantages. Firstly, it is more efficient than the competing models to remove mixed noise and preserve edge. Secondly, our SB method for proposed second-order variational model is fast and accurate in providing visually preasing SN reduction. Finally, we



found what we expected in numerical experiments that it provides better restoration results than those obtained from several regularizations.

The idea presented in this thesis can be expended in different directions. First, variational models used in this work can be developed both fidelity term and regularization term in order to improve restoration result. Next, the algorithm must be modified due to the nonlinearity of EL equation resulting in the slowness.



# REFERENCES

- [1] R. Acar and C. Vogel. Analysis of bounded variation penalty method. *Inverse Problems*, 10:1217–1229, 1994.
- [2] F. Adamo, G. Andria, F. Attivissimo, A.M.L. Lanzolla, and M. Spadavecchia. A comparative study on mother wavelet selection in ultrasound image denoising. *Measurement*, 46:2447–2456, 2013.
- [3] G. Aubert and J.-F. Aujol. A variational approach to removing multiplicative noise. *SIAM J. Appl. Math.*, 68(4):925–946, 2008.
- [4] Z.-F. Pang, B. Shi, L. Huang. Fast algorithm for multiplicative noise removal. *J. Vis. Commun. Image R.*, 23:126–133, 2012.
- [5] M. Bergounioux and L. Piffet. A second-order model for image denoising. *Set-Valued and Variational Analysis*, 18(3-4):277–306, 2010.
- [6] J. M. Bioucas-Dias and M. A. T. Figueiredo. Multiplicative noise removal using variable splitting and constrained optimization. *IEEE Transactions on Image Processing*, 19:1720–1730, 2010.
- [7] K. Bredies. *Recovering piecewise smooth multichannel images by minimization of convex functionals with total generalized variation penalty*. Inst. Math. Sci. Comput., Graz Univ. Technol., Graz, Austria, Tech. Rep. 12-006, 2012.
- [8] K. Bredies, K. Kunisch, and T. Pock. Color TV: Total variation methods for restoration of vector-valued images. *SIAM J. Imaging Sci.*, 3(3):492–526, 2010.

- [9] K. Bredies and H. P. Sun. Preconditioned douglas–rachford algorithms for tv- and tgv-regularized variational imaging problems. *J. Math. Imaging Vision*, 52(3):317–344, 2015.
- [10] K. Bredies and T. Valkonen. *Inverse problems with second-order total generalized variation constraints*. in: Ninth International Conference on Sampling Theory and Applications (Singapore 2011), Nanyang Technological University, Singapore(2011),<https://imsc.uni-graz.at/bredies/papers/SampTA2011.pdf>, 2011.
- [11] C. Brito-Loeza, K. Chen, and V. Uc-Cetina. Image denoising using the gaussian curvature of the image surface. *Numer. Meth. Part. Differ. Equ.*, 32(3):1066–1089, 2016.
- [12] B. V. Brunt. *The calculus of variations*. Springer, 2004.
- [13] A. Buades, B. Coll, and J. M. Morel. A review of image denoising algorithms, with a new one. *Multiscale Model. Simul.*, 4(2):490–530, 2005.
- [14] A. Chambolle and P.L. Lions. Image recovery via total variation minimization and related problems. *Numerische Mathematik*, 76(2):167–188, 1997.
- [15] R.H. Chan, H.X. Liang, S.H. Wei, M. Nikolova, and X.-C. Tai. High-order total variation regularization approach for axially symmetric object tomography from a single radiograph. *Inverse Problems and Imaging*, 9(1):55–77, 2015.
- [16] T.F. Chan, S. Esedoglu, and F. Park. A fourth order dual method for staircase reduction in texture extraction and image restoration problems. *2010 17th IEEE International Conference on Image Processing (ICIP), Hongkong, China*, pages 4137–4140, 2010.
- [17] S. Chankan, N. Chumchob, and P. Sroisangwan. A novel image denoising approach based on a curvature-based regularization. *Signal, Image and Video Processing*, 1:1711–1863, 2023.
- [18] Q. Chen, P. Montesinos, Q.S. Sun, and D.S. Xia. Ramp preserving Perona-Malik model. *Signal Processing*, 90:1963–1975, 2010.

- [19] H. Choi and J. Jeong. Despeckling algorithm for removing speckle noise from ultrasound images. *Symmetry*, 12(6):983, 2020.
- [20] N. Chumchob, K. Chen, and C. Brito. A new variational model for removal of combined additive and multiplicative noise and a fast algorithm for its numerical approximation. *International Journal of Computer Mathematics*, 90(1):140–161, 2013.
- [21] N. Chumchob and I. Prakit. An improved variational model and its numerical solutions for speckle noise removal from real ultrasound images. *International Journal of Computer Mathematics*, 37:1–39, 2019.
- [22] P. Coupé, P. Hellier, C. Kervrann, and C. Barillot. Nonlocal means-based speckle filtering for ultrasound images. *IEEE Trans. Image Process.*, 18(10):2221–2229, 2009.
- [23] J. Eckstein and D. Bertsekas. On the douglas–rachford splitting method and the proximal point algorithm for maximal monotone operators. *Mathematical Programming*, 5(1):293–318, 1992.
- [24] J. F. Epperson. *An introduction to numerical methods and analysis*. WILEY, 2013.
- [25] E. Giusti. *Minimal Surfaces and Functions of Bounded Variation. Monographs in Mathematics, Vol. 80*. Birkhauser, Boston, 1984.
- [26] T. Goldstein and S. Osher. The split bregman method for l1-regularized problems. *SIAM Journal on Imaging Sciences*, 2(2):323–343, 2009.
- [27] J. Hadamard. *Sur les problèmes aux dérivées partielles et leur signification physique*. Princeton university bulletin, 1902.
- [28] Y. Han, X.-C. Feng, G. Baciú, and W.-W. Wang. Nonconvex sparse regularizer based speckle noise removal. *Pattern recognition*, 46:989–1001, 2013.
- [29] X.H. Hao, S.K. Gao, and X.R. Gao. A novel multiscale nonlinear thresholding method for ultrasonic speckle suppressing. *IEEE Trans. Med. Imaging.*, 18(9):787–794, 1999.

- [30] P. Hellier, C. Kervrann, and C. Barillot. Nonlocal means-based speckle filtering for ultrasound images. *IEEE Trans. Image Process.*, 18(10):2221–2229, 2009.
- [31] W. Hinterberger and O. Scherzer. Variational methods on the space of functions of bounded hessian for convexification and denoising. *Computing*, 76(1):109–133, 2006.
- [32] Y. Huang, M. Ng, and Y. Wen. A new total variation method for multiplicative noise removal. *SIAM J. Imaging Sci.*, 2(1):20–40, 2009.
- [33] J.B.-Dias and M.A.T. Figueiredo. Multiplicative noise removal using variable splitting and constrained optimization. *IEEE Trans. Image Process.*, 19(7):1720–1730, 2010.
- [34] J.Huang and X.Yang. Fast reduction of speckle noise in real ultrasound images. *Signal Processing*, 93:684–694, 2013.
- [35] Z. Jin and X. Yang. Analysis of a new variational model for multiplicative noise removal. *J. Math. Anal. Appl.*, 362:415–426, 2010.
- [36] Z. Jin and X. Yang. A variational model to remove the multiplicative noise in ultrasound images. *J. Math Imaging Vis*, 39:62–74, 2011.
- [37] J. Jost, J. Jost, and X. Li-Jost. *Calculus of variations*. Cambridge University Press, 1998.
- [38] J. Koo and S.B. Oark. Speckle reduction with edge preservation in medical ultrasonic images using a homogenous region growing mean filter (HRGMF). *Ultrasonic Imaging*, 13:629–639, 1990.
- [39] J. Koo and S.B. Oark. Despeckling of medical ultrasound images using daubechies complex wavelet transform. *Signal Processing*, 90:428–439, 2010.
- [40] K. Krissian, R. Kikinis, C.F. Westin, and K. K. Vosburgh. Speckle constrained filtering of ultrasound images. *IEEE Comput. Vis. Pattern Recogn.*, 15:547–552, 2005.

- [41] R.J. Lai, X.-C. Tai, and T.F. Chan. A ridge and corner preserving model for surface restoration. *SIAM Journal on Scientific Computing*, 35(2):A675–A695, 2013.
- [42] T. Loupas, W. McDicken, and P. Allan. An adaptive weighted median filter for speckle suppression in medical ultrasound images. *IEEE Transactions on Circuits and Systems*, 36(1):129–135, 1989.
- [43] W. Lu, J. Duan, Z. Qiu, Z. Pan, R.W. Lid, and L. Bai. Implementation of high-order variational models made easy for image processing. *Mathematical Methods in the Applied Sciences*, 39:4208–4233, 2016.
- [44] L.Wenqi, D. Jinming, Q. Zhaowen, P. Zhenkuan, L.R. Wen, and B. Li. Implementation of high-order variational models made easy for image processing. *Mathematical Methods in the Applied Sciences*, 39(14):4208–4233, 2016.
- [45] M. Lysaker, A. Lundervold, and X.-C. Tai. Noise removal using fourth-order partial differential equation with applications to medical magnetic resonance images in space and time. *IEEE Transactions on Image Processing*, 12(12):1579–1590, 2003.
- [46] O.V. Michailovich and A. Tannenbaum. An accurate and efficient bayesian model for automatic segmetation of brain MRI. *IEEE Trans. Ultrason., Ferroelect., Freq. Contr.*, 53(1):64–78, 2006.
- [47] K. Papafitsoros. *Novel higher order regularisation methods for image reconstruction*. University of Cambridge, 2014.
- [48] K. Papafitsoros and C.B. Schönlieb. A combined first and second order variational approach for image reconstruction. *Journal of Mathematical Imaging and Vision*, 48(2):308–338, 2014.
- [49] L. Rudin, S. Osher, and E. Fatemi. Nonlinear total variation based noise removal algorithms. *Physica D*, 60:259–268, 1992.
- [50] L. I. Rudin, P. L. Lions, and S. Osher. *Multiplicative denoising and deblurring: theory and algorithms, in Geometric Level Set Methods in Imaging, Vision,*

- and Graphics, S. Osher and N.Paragios, Eds., pp. 103-120. Springer, Berlin, Germany, 2003.
- [51] O. Scherzer. Denoising with higher order derivatives of bounded variation and an application to parameter estimation. *Computing*, 60(1):1–27, 1998.
- [52] S. Setzer. Split bregman algorithm, douglas–rachford splitting and frame shrinkage, scale space and variational methods in computer vision. *Lecture Notes in Computer Science*, 5567:464–476, 2009.
- [53] J. Shi and S. Osher. A nonlinear inverse scale space method for a convex multiplicative noise model. *SIAM J. Imaging Sci.*, 1(3):294–321, 2008.
- [54] J.N. Shi and S. Osher. A nonlinear inverse scale space method for a convex multiplicative noise model. *SIAM J. Imaging Sci.*, 1(3):294–321, 2008.
- [55] P.V. Sudeep, P. Palanisamy, J. Rajan, H. Baradaran, L. Saba, A. Gupta, and J.S. Suri. Speckle reduction in medical ultrasound images using an unbiased non-local means method. *Biomedical Signal Processing and Control*, 28:1–8, 2016.
- [56] X.-C. Tai. and C. Wu. Augmented lagrangian method, dual methods and split bregman iteration for rof model. *Scale Space and Variational Methods in Computer Vision, LNCS*, 5567(556):502–513, 2009.
- [57] Z. Tao, H.D. Tagare, and J.D. Beaty. Evaluation of four probability distribution models for speckle in clinical cardiac ultrasound images. *IEEE Trans. Med. Imaging*, 25:1483–1492, 2006.
- [58] A. N. Tikhonov. On the solution of ill-posed problems and the method of regularization. *Doklady Akademii Nauk*, 151:501–504, 1963.
- [59] T.Valkonen, K.Bredies, and F. Knoll. Total generalized variation in diffusion tensor imaging. *SIAM J. Imaging Sci.*, 6(1):487–525, 2013.
- [60] C.R. Vogel. *Computational Methods for Inverse Problems*. SIAM Publications, Philadelphia, USA, 2002.

- [61] G.D. Wang, J. Xu, Q. Dong, and Z.L. Pan. Active contour model coupling with higher order diffusion for medical image segmentation. *International Journal of Biomedical Imaging*, 2014:1–8, 2014.
- [62] C. Wu. and X.-C. Tai. Augmented lagrangian method, dual methods, and split bregman iteration for rof, vectorial tv, and high order models. *SIAM J. Imaging Sci.*, 3(3):300–339, 2010.
- [63] L. Xiao, L.-L. Huang, and Z.-H. Wei. A weberized total variation regularization-based image multiplicative noise removal algorithm. *EURASIP Journal on Advances in Signal Processing*, 490384::DOI:0.1155/2010/490384, 2010.
- [64] W. Yin, S. Osher, D. Goldfarb, and J. Darbon. Bregman iterative algorithms for l1-minimization with applications to compressed sensing. *SIAM Journal on Imaging sciences*, 1:143–168, 2008.
- [65] Y.L. You and M. Kaveh. Fourth-order partial differential equations for noise removal. *IEEE Transactions on Image Processing*, 9(10):1723–1730, 2000.
- [66] H. Yua, J.L.Tana, and Y.Y.Wang. Ultrasound speckle reduction by a SUSAN-controlled anisotropic diffusion method. *Pattern Recognition*, 43:3083–3092, 2010.
- [67] D. Zhang. *Diffeomorphic Variational Models and Their Fast Algorithms for Image Registration Problems*. University of Liverpool, 2019.
- [68] J. Zhang and K. Chen. A total fractional-order variation model for image restoration with nonhomogeneous boundary conditions and its numerical solution. *SIAM J. Imaging Sci.*, 8(4):2487–2518, 2015.
- [69] S.X. Zheng, Z.K. Pan, C.X. Jiang, and G.D. Wang. A new fast algorithm for image denoising. *3rd International Conference on Multimedia Technology*, pages 682–689, 2013.
- [70] W. Zhu and T.F. Chan. Image denoising using mean curvature of image surface. *SIAM J. Imaging Sci.*, 5(1):1–32, 2012.



## PRESENTATION AND PUBLICATIONS

- S. Chankan, N. Chumchob and P. Sroisangwan, *A novel image denoising approach based on a curvature-based regularization*, Signal, Image and Video Processing, Published online: 12 January 2023, <https://doi.org/10.1007/s11760-022-02427-5>.



## VITA

**NAME** Miss Siriwan Chankan  
**DATE OF BIRTH** September 5, 1989  
**PLACE OF BIRTH** Kanchanaburi Province  
**INSTITUTIONS ATTENDED** 2008 – 2012 Bachelor of Science (B.Sc.)  
 Major Applied Mathematics  
 Silpakorn University.  
 2012 – 2014 Master of Science (M.Sc.)  
 Major Applied Mathematics and  
 Computational Science  
 Chulalongkorn University.  
**HOME ADDRESS** 102 Village No.7, Wangkrajae Sub-district,  
 Saiyok District, Kanchanaburi, 71150.



